State Estimation of Li-ion Batteries Using Machine Learning Algorithms

Iman Babaeiyazdi

A DISSERTAION SUBMITTED TO
THE FACULTY OF GRADUATE STUDIES
IN PARTIAL FULFILLMENT OF THE REQUIREMENTS
FOR THE DEGREE OF
DOCTOR OF PHILOSOPHY

GRADUATE PROGRAM IN
ELECTRICAL ENGINEERING AND COMPUTER SCIENCE

YORK UNIVERSITY

TORONTO, ONTARIO

January 2023

Abstract

Lithium-ion batteries are mainly utilized in electric vehicles, electric ships, etc. due to their virtue of high energy density, low self-discharge, and low costs. Electric vehicles are prone to accelerated battery degradation due to the high charging/discharging cycles and high peak power demand. Hence, efficient management of the batteries is a dire need in this regard. Battery management systems (BMS) have been developing to control, monitor, and measure the variables of the battery such as voltage, current, and temperature, to estimate the states of charge (SOC) and state of health (SOH) of the battery.

This study is divided into three parts; in the first part, the SOC of the battery is estimated utilizing electrochemical impedance spectroscopy (EIS) measurements. The EIS measurements are obtained at different SOC and temperature levels. The highly correlated measurements with the SOC are then extracted to be used as input features. Gaussian process regression (GPR) and linear regression (LR) are employed to estimate the SOC of the battery.

In the second part of this study, the EIS measurements at different SOC and temperature levels are employed to estimate the SOH of the battery. In this part, transfer learning (TL) along with deep neural network (DNN) is adopted to estimate the SOH of the battery at another outrange temperature level. The effect of the number of fixed layers is also investigated to compare the performance of various DNN models. The results indicate that the DNN with no fixed layer outclasses the other DNN model with one or more fixed layers.

In the third part of this dissertation, the co-estimation of SOC and SOH is conducted as SOC and SOH are intertwined characteristics of the battery, and a change in one affects the other variation. First, the SOH of the battery is estimated using EIS measurements by GPR and DNN. The

estimated SOH, along with online-measurable variables of the battery, i.e., voltage and current, are then utilized as input features for long-short term memory (LSTM) and DNN algorithms to estimate the SOC of the battery.

Dedication

To my parents.

To my brother.

To my friends.

Acknowledgments

I would like to express my truthful gratitude to my supervisor Dr. Afshin Rezaei-Zare for his dedication to help me. His advice helped me to pass the obstacles I had confronted and accomplish this part of my life.

I also would like to thank my beloved parents for their continuous encouragement through my whole life. To those who indirectly contributed in this research, your kindness means a lot to me. Thank you very much.

I would like to thank my committee members for helping to enhance my dissertation with their valuable comments.

Finally, I appreciate my friend's encouragement and support during these years for completing this task. A special thanks goes to my friend Moein Razavi for his advice in this very path.

TABLE OF CONTENTS

LIST OF TABLES

LIST OF FIGURES

List of Acronyms

AEKF	Adaptive Extended Kalman Filter
AKF	Adaptive Kalman Filter
BMS	Battery Management System
BEV	Battery Electric Vehicle
CC	Constant Current
CNN	Convolutional Neural Network
CV	Constant Voltage
DCNN	Deep Convolutional Neural Network
DNN-TL	Deep Neural Network using Transfer Learning
ECM	Equivalent Circuit Model
EKF	Extended Kalman Filter
EIS	Electrochemical Impedance Spectroscopy
EIM	Electrochemical Impedance Model

GA	Genetic Algorithm
GHG	Greenhouse Gas
GPR	Gaussian Process Regression
GRU	Gated Recurrent Unit
IC	Incremental Capacity
IUPF	Improved Unscented Particle Filter
KF	Kalman Filter
LS	Least Square
LSTM	Long-Short Term Memory
MAPE	Maximum Absolute Percentage Error
ML	Machine learning
MSE	Mean Squared Error
OCV	Open-Circuit Voltage
PEV	Plug-in Electric Vehicle
PF	Particle Filter

PHEV	Plug-in Hybrid Electric Vehicle
PSO	Particle Swarm Optimization
RMSE	Root Mean Squared Error
RNN	Recurrent Neural Network
RVM	Relevance Vector Machine
RW	Random Walk
SEI	Solid Electrolyte Interface
SOC	State of Charge
SOH	State of Health
SVM	Support Vector Machine
TL	Transfer Learning
TS	Test Size
UDDS	Urbane Dynamometer Driving Schedule

Chapter 1

Introduction

1.1 Motivation

Global warming resulting from the excessive emission of industry and transportation sections has prompted the emergence of renewable energy and plug-in electric vehicles (PEVs), including battery EVs (BEVs) and plug-in hybrid EVs (PHEVs) [1], [2]. According to the Environmental and Climate Change Canada [3], the transportation sector contributes to 25 % of greenhouse gases (GHG), as shown in Figure 1-1.

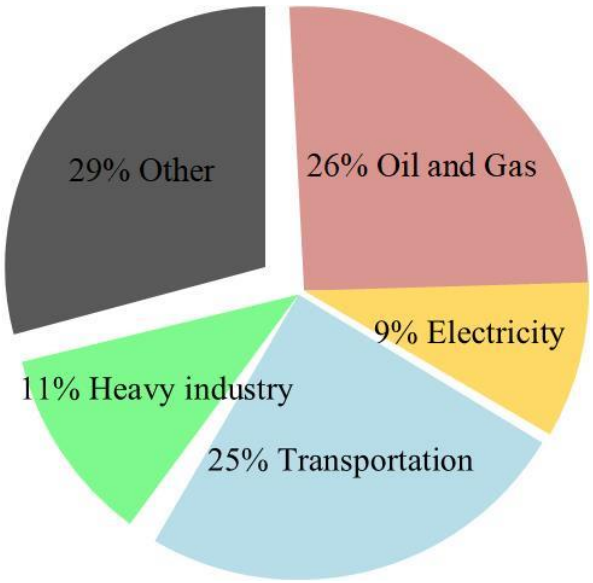

Figure 1-1. Canada's 2018 Greenhouse Gas Emissions Breakdown by Sector.

From the transportation sector's perspective, in order to deteriorate the adverse impacts of GHGs, the accelerated replacement of internal combustion engines (ICEs) with eco-friendly PEVs is a potent

solution [4], [5]. Moreover, PEVs can greatly be effective in reducing air pollution, such that based on Energy Information Administration, their contribution can lead to the reduction of 50% to 70 % of carbon emission [6]. In 2020, the number of EVs was about 7 million worldwide as compared to 5 million in 2019, which shows an increase of 40%. The range anxiety, high initial cost, and long charging duration have been some of the main issues of customers being addressed by advanced battery technology and modern charging station infrastructures [7]. Vast integration of charging stations for PEVs is one of the alternatives for addressing the above issues. Charging stations have been introduced to the market with various power levels and are divided into fast and slow chargers.

As another potential alternative, a lot of advances have been made toward the application of lithium-ion battery energy storage systems in PEVs. Lithium-ion batteries are extensively employed in electrified transportation due to their superiority of high energy density, low self-discharge, low costs, etc. [8], [9]. Nonetheless, lithium-ion batteries can sustain capacity fade during constant charging/discharging cycling primarily due to lithium inventory loss, solid electrolyte interface (SEI) layer growth, and impedance increase [10]. Efficient management of batteries is essential to safeguard EV operation, reduce drive-range anxiety, prolong the lifespan and decrease the cost of the batteries. Hence, A battery management system (BMS) is of substance in PEVs. BMS includes different components, such as sensors, controllers, and signal lines [11]. The BMS contributes significantly to charging/discharging processes, proper operation, and EV battery lifespan. The main task of BMS is to measure current, voltage, and the temperature of the batteries for estimation of different states of the battery, such as state of charge (SOC), state of health (SOH), and state of available power capability through implemented algorithms on the BMS [12]. SOC is the capacity of the battery at the current state compared to the battery's capacity at fully charged state. SOH is defined as the maximum available capacity of the battery proportionate to the nominal capacity of the battery, which typically is provided by the manufacturer.

Moreover, SOC and SOH cannot be measured directly from inner quantities such as internal resistance and capacitance of the battery. As a result, external quantitative indices are utilized for SOC estimation [13]. There are myriads of literature proposing various algorithms for the state estimation of lithium-ion batteries. The literature can be mainly divided into three categories: 1) SOC estimation methods, 2) SOH estimation methods, and 3) Co-estimation of SOC and SOH methods. For each of the mentioned categories, the methods are divided into three main classes, namely, model-free methods such as Coulomb counting methods, model-based methods such as equivalent circuit models (ECM), and electrochemical impedance models (EIM), which are utilized along with some filters, and finally data-driven methods. Given this, there are abundant studies that will be extensively discussed in the later chapters.

In this dissertation, we have investigated the effectiveness EIS measurements for states estimation of Li-ion batteries using different machine learning (ML) algorithms. Hence, the main contributions of this dissertation are as follows:

EIS measurements as information-rich datasets have been utilized for estimating two of the most important states of Li-ion batteries, i.e., SOC and SOH. Contrary to the conventional studies that use EIS measurements to build EIM to estimate SOC and SOH, in our study, the EIS measurements were utilized directly as input features in different ML algorithms to serve the mentioned purpose. Moreover, the conventional research uses some features, which are dependent on the charging/discharging procedures or are extracted from incremental capacity curves, for Li-ion battery states estimation. Sometimes additional mathematical computation might be required to obtain the features from charging/discharging schemes such as time to reach cut-off voltage or current. However, EIS measurements are not restrained by the charging/discharging procedures and can be acquired at any operational conditions without additional mathematical burden. In

contrast to the other features, at various operating conditions, EIS measurements provide profound insight about the electrochemical properties and characteristics of the Li-ion batteries with different chemistries. Therefore, they can be considered as potential dataset for the fulfillment of accurate states estimation. Given this, in our dissertation, the effectiveness of using EIS measurements directly as input features in various ML algorithms is investigated, and the performance of ML models is evaluated in states estimation.

In our study, first, it is intended to investigate the effectiveness of EIS measurements at different ambient temperatures as potential features in ML algorithms for solely SOC estimation. EIS measurements are used directly as input features instead of being used for building an electrochemical model. As EIS measurements are obtained at different frequencies, in order to decrease computational burden, highly correlated measurements with the SOC are selected as input features. Two ML algorithms, i.e., Gaussian process regression (GPR) and linear regression, are then adopted to serve the SOC estimation, and the results for each algorithm are compared.

Second, EIS measurements at different aging and temperature levels are employed to solely estimate the SOH of the battery, and their effectiveness in fulfilling this purpose is investigated. In this case, transfer learning (TL) technique with a deep neural network (DNN) is utilized to estimate the SOH of the battery at outrange temperatures. TL technique will help us avoid time-consuming experiments for collecting dataset form aging the batteries. In another word, using this technique enables us to achieve an accurate model by training our model using small-size dataset. This claim is proved by evaluating the accuracy and robustness of the proposed model, utilizing different sizes of test datasets. Moreover, the effect of the number of fixed layers on the performance of the model during transfer learning is also investigated, and the results of different models with different numbers of fixed layers are compared with the base DNN model.

Third, since the SOC and SOH are intertwined in the battery and mutually affect each other, in order to achieve a more precise and qualified SOC estimation, the effect of SOH should be considered as well. To serve this purpose, SOH should be utilized as an input feature along with any other features to estimate the SOC. In our study, the EIS measurements are utilized for SOH estimation using two ML algorithms, i.e., DNN and GPR (for comparison). The dataset utilized in this part has been obtained from a standard driving cycle. Therefore, it can accurately simulate the practical application of the proposed strategy. The estimated SOH, along with battery's measurable variables, such as voltage and current, are adopted as input features in two other ML algorithms, i.e., DNN and long-short term memory (LSTM) (two algorithms have been selected for comparison) to accurately estimate the SOC.

1.2 Overview of this dissertation

In this dissertation, the second chapter is dedicated to the fundamentals of lithium-ion batteries and the EIS tests and BMS fundamentals. The operation of lithium-ion battery in an electrical circuit during charging/discharging processes is discussed. The chemical and mechanical degradation processes and their impacts on each component of the cell are briefly explained. This chapter presents the constituting components of a lithium-ion cell and their key roles in the cell. Additionally, EIS procedure and its basics are presented. The key functionalities of BMS, such as cell monitoring, cell balancing, charging/discharging schemes, are briefly explained.

The third chapter presents the literature review pertaining to SOC estimation methods and our contribution in this regard. This chapter employs informative measurements of EIS obtained at different temperatures and SOC levels in ML, i.e., linear regression model and Gaussian process regression (GPR), to accurately predict the SOC of li-ion batteries. First, a feature sensitivity

analysis of the data is conducted to extract the most reliable features, i.e., the EIS impedances which are highly correlated with SOC, from EIS measurements. The feature sensitivity analysis is conducted using Pearson correlation method. Then, the ML models are fed by the chosen features. These models are designed to train the input features and establish the mapping relationship between the selected features and the SOC.

The SOH estimation using TL with DNN is presented in chapter 4. First, the base DNN model is trained and validated based on the source dataset containing EIS measurements at the temperatures of 25 °C and 35 °C. Then, the base DNN model is retrained and validated using different proportions, i.e., the first 50% and 20% of the target dataset, which contains EIS measurements at the temperature of 45 °C. This will create a new model called DNN-TL carrying the knowledge from the base model. The DNN-TL model is employed to predict the second proportions, i.e., the second 50% and 80% of the target dataset considered as missing data.

The co-estimation of SOC and SOH using different ML algorithms is discussed in chapter 5. ML approaches are adopted to estimate SOC of the battery, considering its state of SOH. First, the ML algorithm is employed to directly estimate the SOH using electrochemical EIS measurements as input features. The SOH is estimated separately using the EIS obtained at three SOC levels, i.e., 20%, 50%, and 80%. The SOC and SOH datasets used for this study have been obtained from the standard driving cycles, which aid the proposed method in generalizing to dynamic real-world EV applications. The effectiveness of direct usage of EIS measurements instead of using them to build EIM is verified and how informative they convey the health status of batteries at different SOCs is indicated. Additionally, its efficacy in SOC estimation is implicitly demonstrated by adopting the estimated SOH along with voltage and current as input features.

Finally, the conclusions and future works are drawn in chapter 6. Figure 1-2 shows the

overview of this study.

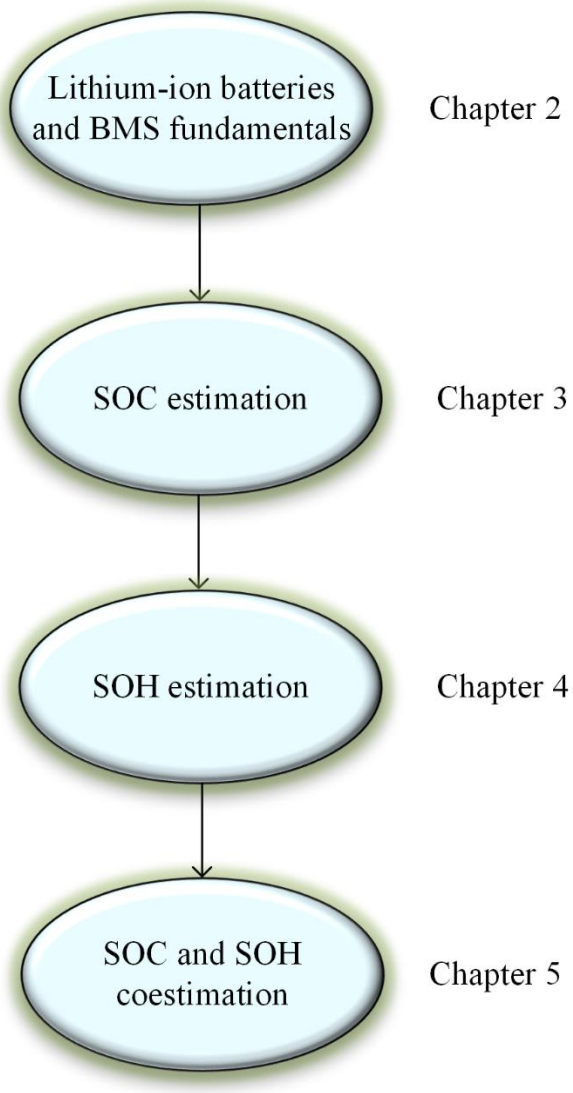

Figure 1-2. Overview of the dissertation

Chapter 2

Battery and BMS Basics

2.1 Lithium-ion battery fundamentals

Rechargeable batteries are the primary electrochemical energy storage in EVs. They can quickly respond to load variation and accept re-generated power [14]. A typical lithium-ion battery consists of the following main components: cathode, anode, electrolyte, and separator. Lithium-ion batteries contain two electrodes, i.e., cathode (the positive electrode) and anode (the negative electrode), whose chemical potentials are different. The chemical potential difference determines the cell's open circuit voltage (OCV). The electrolyte allows the lithium ions diffusion between the electrodes during charging/discharging cycles [15]. The separator is an inactive part of a lithium-ion battery that hinders the physical contact between the anode and cathode [15]. Upon the electronically connection of an external circuit to the two electrodes, electrons move from the anode to the cathode resulting in a balanced potential between the two electrodes. Positive lithium ions migrate through the electrolyte in the same direction. In this scenario, the chemical energy stored in the cell is then released as electrical energy in the external circuit. The discussed procedure occurs while discharging the battery. This procedure is reversible, implying that lithium ions can migrate back to the anode for charging the battery, whereby electrical energy is converted back to chemical energy [15]. Figure 2-1 demonstrates the working principle of a lithium-ion battery.

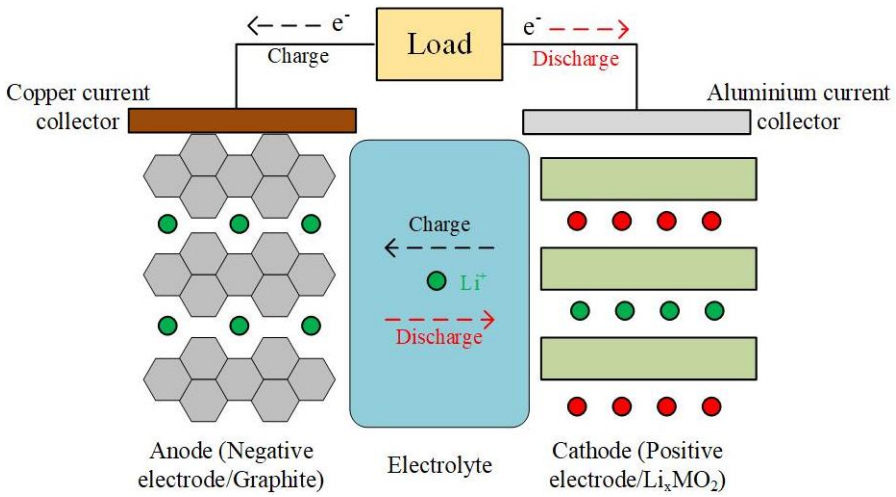

Figure 2-1. Battery's operation principle

2.2 Main components of lithium-ion battery

The four major components of a typical lithium-ion battery are as follows: anode, cathode, electrolyte, and separator. The cell life cycles, performance, and operating conditions are dictated by the interactivity of these components.

2.2.1 Electrodes

The electrodes consist of active materials, additives, and binders. The active materials are graphite and metal oxides for anodes and cathodes, respectively. Active materials' primary objective is to safely accommodate lithium for prolonged cycling [16]. During battery operation, lithium ions transfer back and forth between the two electrodes and experience intercalation and de-intercalation process. The additives are employed to improve the electronic conductivity within the electrode.

The anode of a lithium-ion battery has a Li intercalation compound covered into a thin layer on the copper current collector. Homogeneous and thin covers of the active materials are essential for

the batteries employing organic electrolytes (almost all the commercial cells available at present) [15], [16]. Hence, the process of anode manufacturing, including anode material mixing and covering, affects the properties of the battery, such as rate capability, battery capacity, and the aging mechanism of the cell. Deficiencies regarding the anode coating can contribute to cell thermal runaway and failure. Carbonaceous materials are utilized for the anode structure. The most widely used anode material is graphite, as they have demonstrated a reasonable rate of lithium intercalation/de-intercalation, improving the charge/discharge process. Although, the battery performance is affected due to SEI formation on the anode due to the electrolyte decomposition during cell operation [15].

The cathode consists of layered oxides such as $LiMO_2$ and LiM_2O_4. There are different materials used for the cathode in commercial lithium-ion cells such as lithium cobalt oxide ($LiCoO_2$), lithium manganese oxide ($LiMn_2O_4$), lithium iron phosphate ($LiFePO_4$), or mixed metal oxides, such as nickel manganese cobalt oxide (NMC). The cobalt-based cells have higher capacity, low-discharge rate, and high discharge voltage; however, they are expensive and toxic, and not environmentally friendly. Manganese-based cells are cheaper, but they restrict the performance of the cells as they tend to dissolve into the electrolyte during cycling resulting in further capacity fade of the cells. $LiFePO_4$ cells have lower voltage level but demonstrate higher power and density. Moreover, they are cheap and eco-friendly.

2.2.2 Electrolyte

An electrolyte is formed of one or more liquid solvents along with lithium salts. Electrolytes should have the following features [17]: (i) good ionic conductivity and electronic insulation to ease ion transport and minimize self-discharge. (ii) should be electrochemically inactive with oxidizing or reducing electrode surface. (iii) should not react with other components of the cells.

Electrolyte is typically composed of one or more liquid solvent with lithium salts. The widely-used salt is lithium hexafluorophosphate ($LiPF_6$). Non-aqueous electrolytes are the most common electrolytes for li-ion batteries. A mixture of linear and cyclic carbonate solvent such as ethylene carbonate and dimethyl carbonate is usually used in the electrolytes carry the merits of low viscosity, high ionic conductivity, and SEI-forming ability. It is worth mentioning that battery manufacturers are trying to replace liquid electrolytes with solid-state electrolytes. The advantages of solid-state electrolytes are having a wide range of operating temperatures, being non-flammable, improving energy density by using lithium as anode material and enabling bipolar electrode configuration [18]. Still, considerable time and effort are needed before commercializing solid-state batteries. So far, most sloid electrolytes suffer from inherently lower ionic conductivity and Coulombic efficiency compared to liquid electrolytes. Another contributing factor to the performance of solid-state batteries is their electrochemical stability. Finally, some solid electrolytes are significantly reactive to environmental exposure changing the chemistry and kinetics at their interfaces [18], [19].

2.2.3 Separator

A separator is a porous membrane between the anode and cathode. The critical task of the separator is to physically detach the anode and cathode to prevent the short-circuit inside the cell. The porosity of the separator allows the movement of lithium ions during charging/discharging cycling. A separator should have the following properties [15]: (i) good electronic insulation. (ii) proper mechanical and thermal stability and physical strength. (iii) chemical stability and resistance against deterioration. (iv) uniformity in thickness and tortuosity. (v) high ability to prevent migration of soluble species or particles between the two electrodes. (vi) low air permeability, i.e., low electrical resistance and high porosity.

Polyolefins are the most widely-used separators in Li-ion batterie. There are different types of polyolefins such as polyethylene, polypropylene, or laminates of polypropylene and polyethylene. [15]. Separators are categorized based on the number of polyolefins layers, i.e., monolayer and multilayer [20]. Although monolayer polyolefin has mechanical strength and chemical stability, they show high thermally induced dimensional shrinkage at high temperatures leading to short-circuit inside the battery. On the other hand multilayer separator tackle the mentioned problem by blocking the ion conductivity upon melting at high temperature condition [20].

2.3 Degradation mechanism in Li-ion batteries

Battery aging is defined as decline in lifespan, functioning, and reliability of the battery. Battery aging will result in either capacity reduction or power fading, or both of them. As the batteries consists of a complex set of intertwined components subject to the aging, a cell component's aging affects the functionality of other components, which will, in turn exacerbate the whole system aging [21]. Degradation mechanisms in batteries are significantly complicated, as all components of the cell contribute to the aging and mutually affect each other. The relationship between different components indicates that degradation mechanisms spring from both chemical and mechanical origins. Therefore, aging mechanism can be divided into the following:

2.3.1 Chemical degradation mechanism

Electrolyte decomposition, excessive SEI growth, binder decomposition, solvent co-intercalation, active material loss, gas venting, and loss lithium inventory are the main chemical degradation mechanisms in lithium-ion batteries [21]. The electrolyte can be reduced in anode and during low and very high potentials. Electrolyte impurities operates as catalyst for the side reactions. Temperature and cell voltage are contributing factors in the kinetics of side reactions

[22]. The interactions between the electrolyte and electrode results in formation of interface layers on the electrode which will lead to impedance increase and capacity fade.

2.3.2 Mechanical degradation mechanisms

Side reactions are not the sole cause for battery aging. Lithium insertion and extraction lead to the volume expansion or shrinkage in the electrodes. This process occurs heterogeneously.

Mechanical degradation mechanisms pertain to the volume changes and subsequent stress generated in the active material particles of the electrode during lithium intercalation and de-intercalation. As a result of tensile stress, active material may experience cracks, loss of physical contact between each other or from the current collectors, and isolation as well [23]. Charging and discharging cycling result in changes in structure of pores in separator and leads to lower lithium ion mobility. Mechanical degradations mechanisms are aggravated as the cell ages, compromising the cathode and anode structures as well as mechanical properties of the other component.

2.4 Degradation in cell components

2.4.1 Anode degradation

The reactions between the anode and electrolyte are believed to be the main cause of anode degradation [24]. The reactions between the anode surface and the electrolyte cause the electrolyte to decompose. The products of electrolyte decomposition will be deposited on the anode surface, forming a thin layer called SEI. The active lithium ions are consumed by the SEI layer which leads to resistance increase in the anode.

When SEI is initially formed, it benefits the cell by restricting the electrolyte from further decomposition and anode corrosion. Although the SEI grows continuously during the battery life, its growth takes place at lower rate compared to the initial stage as the kinetics of decomposition

reaction limits the SEI growth [25].

The SEI growth affects the resistance of both electrodes, porosity of separator, and wettability of the electrolyte. The SEI growth soars at lower anode voltage and higher temperatures [25]. Since SEI is the product of electrolyte decompositions and is formed onto anode surface, its characteristics are significantly dependent on the electrolyte solvent and salt and anode surface. Moreover, SEI is considered as the main reason of batteries degradation in the form of internal resistance increase and capacity fade or lithium inventory loss.

Another cause of anode degradation is lithium plating. This process is defined as the precipitation of lithium metal occurring at the surface of the anode while it voltage exceeds the threshold value [23]. Lithium plating creates lithium dendrites which can pierce the separator and consequently lead to short-circuit in the cell, an instant cell failure.

Changes in anode structure is another contributing factor to aging. Electrical/mechanical contact loss between the anode components leads internal resistance increase. One of the inevitable sources of contact loss is the change in the volume of anode active materials. The volume change leads to mechanical stresses and disintegration throughout the anode structure [22]. Contact loss occurs between: 1) carbon particles, 2) carbon and current collector, 3) carbon and binder, and 4) current collector and binder. Mechanical stress changes the porosity anode electrode as it is important for the anode electrode to let the electrolyte penetrate the bulk of anode.

Additionally, the current collector of anode electrode may face corrosion through reacting with electrolyte components, or when the anode voltage is too high. In such a case, mechanical or electronic contact loss between the current collector and other components of the anode electrode are resulted [26].

2.4.2 Cathode degradation

There are a couple of changes on the cathode which can impact the life of the lithium-ion batteries [26]:

- Active material aging
- Changes or degradation of electrode components such as binder, conducting agents, or current collector corrosion
- Electrolyte component oxidation and subsequent formation of surface film
- Aging product reaction with anode

The above-mentioned reactions do not necessarily occur separately and may be dependent on each other. Capacity deterioration in positive active materials have their roots in the following [26]:

- Structural changes within cycling
- Modification of surface film
- Chemical decomposition or dissolution reaction

Similar to anode electrode, degradation in cathode electrode is contingent upon SOC and cycling conditions. The insertion/extraction of lithium ions results in changes in positive active material volume that can create mechanical strains for the cathode components.

During insertion/extraction of lithium ions, some of the cathode oxide may experience the phase shift, leading to the crystal lattice distortion and mechanical strains [25]. The stains at the boundaries of the phase contribute to lack of coherence and nanoparticle cracking.

Active material dissolution in cathode is another source of capacity degradation and is mainly seen in Mn-based cathodes. The Mn dissolution into the electrolyte shows twice effect on the cell

aging. So active material dissolution, first caused the active material loss, second the dissolved active material migrates to the anode and will be deposited on its surface, increasing the resistance of the anode [21].

Isolation of the active particles in cathode electrode is one of the main causes of battery deterioration [22]. There are two justifications for this mechanism [21]:

- Crack formation in the active material
- Fracture of the binder, which connects the active particles

Therefore, the isolation of active material is stemmed from mechanical degradation of the active material and binder, as well as chemical degradation of the binder.

2.4.3 Separator degradation

Separator deteriorates mainly due to the lithium dendrite growth caused by separator pores, structural reduction from high temperature or cycling numbers, and the blocking of passageways in the separator over cycling [21]. At very high temperatures, the separator film softens and the pores close, making the ion transportation between the electrode difficult. In such a case the separator is called *shutdown* separator.

Although the chemical properties of materials used for separator is of substance, as they should be inert and do not impact the electrical output, their physical properties can significantly affect the cell performance and safety. To maintain a good functionality in lithium-ion batteries, separators should possess uniformity in their porous structure, low shrinkage, and low resistance [27]. The resistance of separator to penetration, separator thickness, separator porosity, and its toughness may vary by desirable cell characteristics and functions [27]. One of the ways to increase cell capacity is to use thinner separator; however, this method has some deficiencies, as thinner

separators can contain less electrolyte and do not show good mechanical strength. It has been demonstrated in [28] that one of the reasons of power fading originating from separator is due to the inherent increase in the separator ionic impedance. The ionic impedance is highly dependent on the number of cycling and temperature. The ionic impedance increase is resulted from the clogging of separator pores caused by the electrolyte decomposition products, which is accelerated at high temperatures.

2.5 EIS fundamentals

EIS is an information-rich technique for investigating processes taking place in batteries. From EIS measurements, one can effectively deconvolute electrochemical reactions into a series of basic procedures [29]. EIS is able to diagnose one or more processes in the cell, such as (i) electron movements from the current collector to the electrodes, (ii) lithium ion migration across the electrodes, (iii) double-layer capacitance at solid/liquid interfaces, and (iv) migration and diffusion of the ions inside separator and active storage particles [29]. EIS is a non-destructive and information-rich test which is conducted by galvanostatic or potentiostatic excitation signal over a wide range of frequencies to obtain the impedance of the battery during charging and discharging [30]. The excitation signals in galvanostatic and potentiostatic methods are commonly sinusoidal current and voltage; the corresponding response will be voltage and current, respectively. Based on these waveforms, the electrochemical impedance of the battery can be calculated. The impedance of the battery is obtained based on the following equations in galvanostatic mode [31]:

$$\Delta I = I_{max} \sin(2\pi f t) \quad \text{2-1}$$

$$\Delta V = V_{max} \sin(2\pi f t + \emptyset) \quad \text{2-2}$$

$$Z(f) = \frac{V_{max}}{I_{max}}\, e^{j\emptyset} \qquad 2\text{-}3$$

where ΔI is a sinusoidal current at frequency f , which is superimposed on the dc charging/discharging current and results in ΔV and phase angle $\emptyset$. Accordingly, 2-3 shows that the battery's impedance is frequency-dependent and characterized by its magnitude and phase angle. Figure 2-2 indicates a typical EIS spectrum. The horizontal axis indicates the real part of the impedance, and the vertical axis shows the negative of the imaginary part of the impedance. The EIS spectrum is drawn over a wide range of frequencies. The low-frequency tail indicates the diffusion of Li-ions processes inside the active material of the battery. The Li-ions diffuse in electrodes due to their gradient concentration in the components during charging/discharging process. The mid-frequency semi-circle indicates the double-layer capacitance effect. The double-layer capacitor is due to the charged ions in extremely short distance of the electrodes. Moreover, the semicircle indicates the charge transfer conductivity inside the battery cell. In the high-frequency region, the intercept of the EIS curve with the real axis is the indicator of the Ohmic resistance of the battery. This resistance is the sum of Ohmic resistance of all components including electrolyte, electrodes, and separator in the battery cell. The high frequency region also represents inductive impedance of the battery cell due to current collectors at each electrode and the wiring of the connected devices to measure the EIS. The Nyquist plot of Figure 2-2 does not indicate the frequencies at which the impedances have been measured. However, this representation of EIS measurements is sensitive to the changes of battery cell. An alternative representation of EIS measurements is Bode plot which indicates the magnitude and phase angle of the impedances at different frequencies in logarithmically scale. A general Bod diagram has been shown in Figure 2-3. Bode diagrams are not sensitive to changes but indicate the impedance at each frequency.

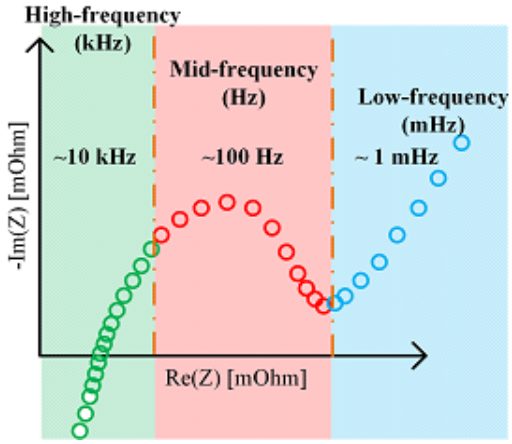

Figure 2-2. Typical EIS spectrum of lithium-ion battery

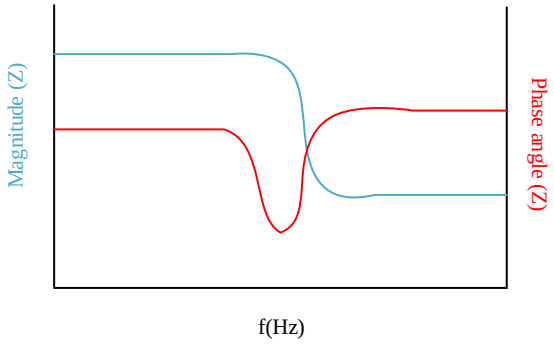

Figure 2-3. Typical Bode diagram for EIS measurements of lithium-ion battery

2.6 BMS

BMS is a control unit in battery energy storage systems responsible for the safe operation of the battery pack [32], [33]. The chief purpose of the BMS is to safeguard the battery cells inside the battery pack. Monitoring individual cells inside the battery pack is indispensable due to safety reasons, cell balancing, and aging issues [34]. BMS can disconnect the battery modules from the whole system in abnormal conditions. In EV applications, BMS and microcontroller unit (MCU) is responsible for energy management and distribution between different components of the EV, e.g., from the battery to the DC/DC converter and from the DC/DC converter to the DC/AC

converter, and finally to the electrical motor of the EVs [35]. Figure 2-4 indicates how the above electrical components are integrated together. Figure 2-5 show how a BMS in PEVs connects to the battery pack and rest of the systems. BMS will read and sample the data from the battery pack and send the information back to the data collection center, display terminal, and vehicle controller. The BMS communicates with the vehicle electronic parts through controller network area (CAN).

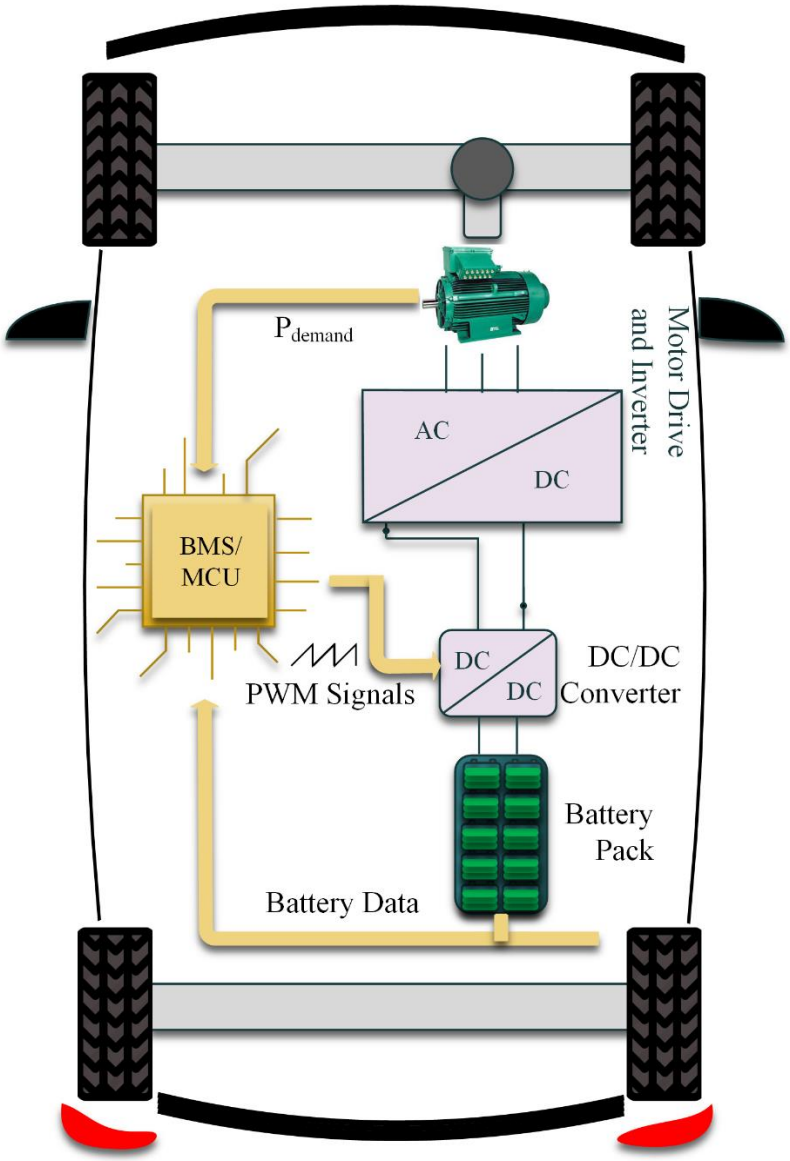

Figure 2-4. BMS in an EV

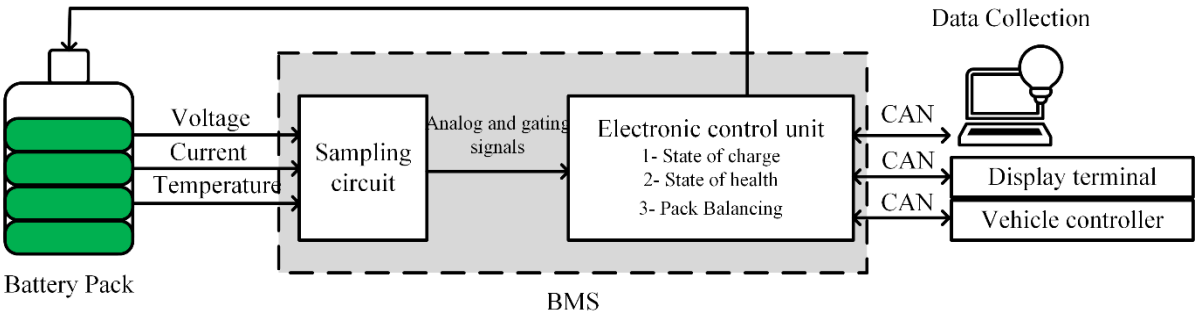

Figure 2-5. BMS integration with a battery pack

2.6.1 Components and topology

BMS is implemented along with other system modules to fulfill the desired tasks. For example, a battery energy storage system consists of BMS, a battery interface module, battery units, and battery supervisory control [36].

The topology of BMS is divided into three categories: distributed, centralized, and modular. In a distributed topology, each control unit is dedicated to each cell by a communication link. In a centralized architecture, a single control unit and battery cells are connected through wires. In a modular structure, some control units are integrated with particular battery cells, and all are connected to a central control unit [37]. Figure 2-6 shows different topologies of BMS.

2.6.2 Software architecture

BMS software is capable of multitasking. A BMS software's primary tasks such as voltage, current, and temperature measurements, over current/voltage protection, and protective relay actuation, must be carried out promptly to safeguard BMS safety. The BMS software includes a real-time operating system to perform real-time operations [38].

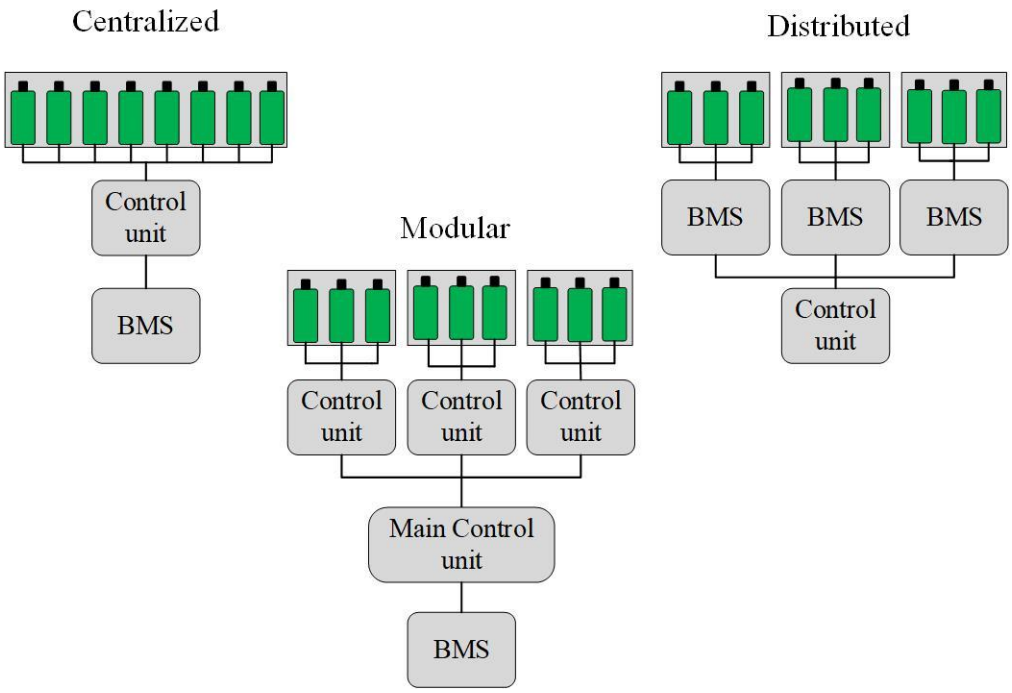

Figure 2-6. BMS topologies

2.6.3 Functionalities

BMS measures the typical battery quantities such as cell or pack voltage, current, impedance, and temperature to estimate the SOC, SOH, and operational key parameters of the cell or the battery pack. The above measurements improve battery performance and increase battery lifetime.

BMS consists of functional unit blocks and design techniques. Different applications determine the battery requirements for architecture, functional unit blocks, and electronic circuitry to design a BMS and its charging/discharging scheme [39]. In order to optimize the life of the battery pack, the following considerations should precede [39]:

- Battery pack functionality and safety features
- Robustness among the system units in various hazardous cases
- Energy management system with a user interface to control and evaluate the performance of the battery system in different system blocks

BMS should possess the following capabilities to ensure the safety of the battery pack: protection, stability and resiliency, automatic charging/discharging, cell balancing, and monitoring. Figure 2-7 shows the BMS functions.

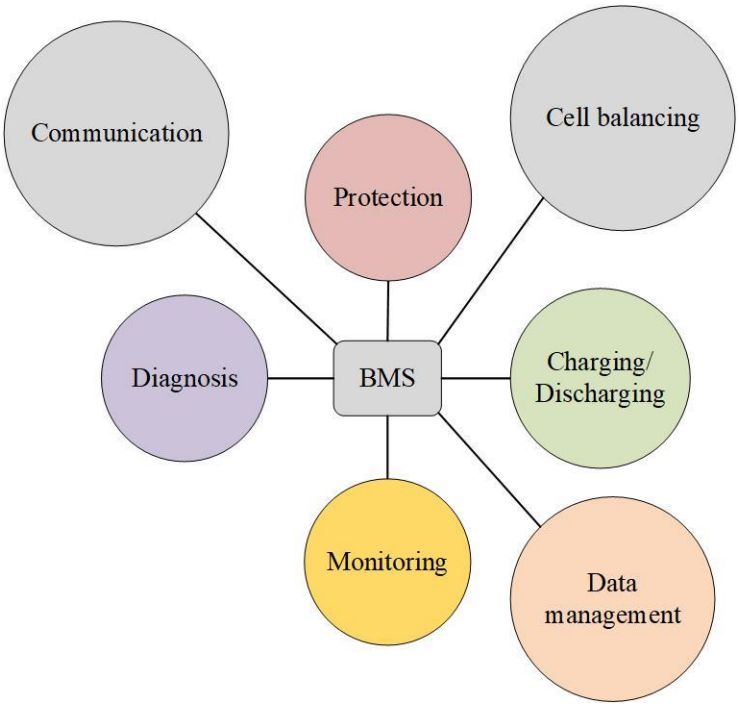

Figure 2-7. BMS functions

- **Monitoring**

BMS mainly observes cell or battery pack voltage, current, temperature, isolation, and interlocks. A faulty BMS may result in overvoltage and overcurrent in the battery pack or cell, which lead to irreversible damage to the whole battery pack [40]. On the other hand, overcharging causes cell venting. Vented gases inside the cells are flammable; they may create hazardous events. Analogously, low voltage and current impose permanent damage to the cells. Also, isolation is required to prevent physical contact between persons and electrical equipment of the battery pack. Temperature observation is another preeminent task of BMS; hot and below-zero temperatures negatively affect battery performance.

- **Protection**

BMS ought to protect the battery pack and related electrical equipment from hazards. The BMS protection scheme includes authenticating the system, detecting operating mode, setting fault criteria, predicting the pack or individual cell overvoltage/overcurrent, predicting the isolation fault, and detecting abnormal operating conditions [34]. Protection from environmental conditions is a dire need, since they can impact the cell or battery pack parameters over the long run.

- **Cell balancing**

Cell balancing is one of the most important functions of a BMS. Although it is preferred that each cell inside the battery pack perform identically, many contributing factors prevent this from happening. These factors, such as variances in the manufacturing process and inhomogeneous temperature distribution, will result in the uneven capacity fade of cells in a battery pack [41], [42]. The above factors result in individual cells undergoing slight differences in degradation and resistance. For example, in a study, a 20% variance in resistance and capacity of parallel connected cells was found to decrease pack lifetime by 40%, showing the adverse effect of having inconsistent cell characteristics [43]. Given this, it is essential to include a method of cell balancing in a BMS. There are two methods for cell balancing, namely, passive and active balancing. The former utilizes a resistive circuit to drain energy from the most charged cells and reduces their SOC to the SOC of the cell with the lowest SOC. The drained energy is wasted in a resistive load [44], [45]. While the latter utilizes complex circuitry to balance the cells. The active method employs capacitors [46], [47], inductors [48], [49], transformers [50], [51], and various power electronic converters [52], [53] to transfer the energy between the cells with minimized energy waste. The advantages of this method are fast balancing speed are high efficiency; however, this method suffers from high complexity and cost [54]. Figure 2-8 shows active and passive balancing

methods.

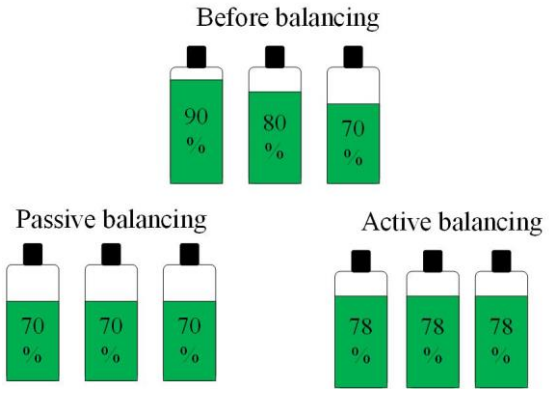

Figure 2-8. Cell balancing methods

- **Charging and discharging schemes**

The number of charging and discharging cycling and charging/discharging procedure influence the battery life and performance. BMS must ensure an efficient way of charging/discharging the battery pack/cell. The SOC and SOH of the battery are interconnected and affect each other mutually; hence, a BMS must maintain the appropriate SOC so that the battery's health is not compromised [55], [56]. To properly manage the charging/discharging scheme, the BMS should perform the following tasks: issue signals to active switches of the converters, monitor the charge current, run the pre-charge sequence, and conduct active or passive cell balancing [57].

Additionally, various charging schemes have been developed and improved to reduce charging duration and charging impact on battery degradation. Constant Current – Constant Voltage (CC-CV) is most widely-used; however, other charging schemes are listed below [58]:

- Constant Current
- Constant Voltage
- Pulse Current

In constant current method, as the name suggests, a constant current charges the battery till a pre-set voltage is reached. This method may impose overheating risks on the battery at the onset of charging process. In the constant voltage method, a constant voltage is applied to the battery and the charging process lasts till the charging current reach to a pre-set value. Because the charging current is less that to the one in constant current method, the charging duration is higher in this method. Combining the first and second methods will create faster charging process which is call CC-CV. This approach has been shown in Figure 2-9 (a). This charging process includes two stages: in the first one, charging process begins by injecting a constant current to the battery till the voltage of the battery reaches a pre-set value (V_{set}). In the second stage, the pre-set voltage is fixed upon the battery's terminal and the current starts declining as the battery charges. The current decreases till it reaches a pre-set value (around 0.1C or I_{set}) and the charging process is terminated.

In Pulse current method, current pulses with a specific duty cycle are injected to the battery. The magnitude of current pulses and their duty cycle can be varied during the charging procedure [58]. Charging process terminates when the battery voltage reaches a pre-determined voltage, and the frequency of pulses can be between 0.2 Hz and 100 Hz [44]. Figure 2-9 (b) shows this method of charging.

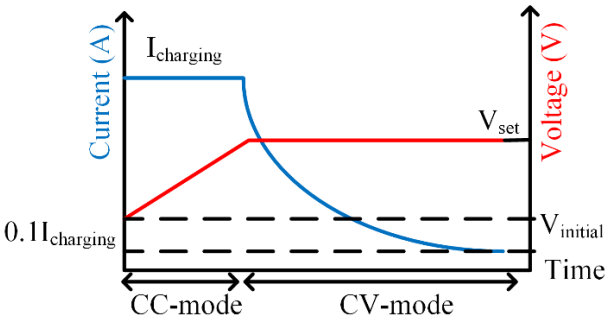

(a)

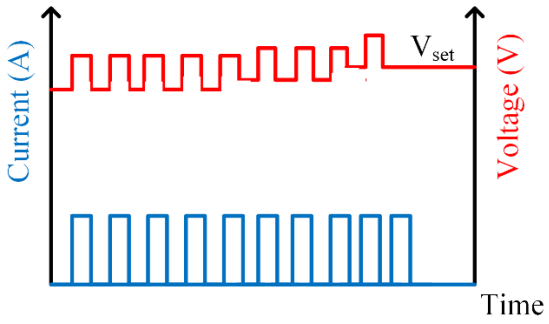

(b)

Figure 2-9. Charging schemes

- **Diagnosis**

BMS is responsible for detecting faults, such as fires, thermal runaway, and minimizing the repercussions of fault effects.

2.7 Conclusions

In this chapter, the fundamental operation of lithium-ion batteries was discussed, and the components of a lithium-ion batteries and their functionalities were presented. Basic information about one of the most information-rich tests, EIS, was provided. EIS can provide insightful details about the behavior of the battery at different SOC and SOH levels. Hence, it is potential data to be adopted for state estimation of the batteries.

Over the lifespan, lithium-ion batteries undergo capacity fade and degradation due to various operating conditions. Many factors contribute to the capacity loss of the batteries, such as ambient temperature and abnormal charging/discharging cycles. If proper management of the battery cell/pack is not considered seriously in any battery-powered devices and vehicles, the malfunction of the battery system may lead to hazardous events. Hence, BMS is of substance to prevent mal-operation of the battery. The key roles and functionalities of BMS, such as monitoring and

aggregating battery data, controlling charging/discharging procedures, and cell balancing in battery packs, were also briefly presented in this chapter.

Chapter 3

SOC Estimation Using EIS

3.1 Introduction

As discussed in Chapter 1, one of the main tasks of BMS is to measure the SOC of the battery. SOC is defined as the capacity of the battery at the current state compared to the battery's capacity at fully charged state. SOC can be calculated as follows [59]:

$$SOC(t) = \frac{C_r}{C_m} \times 100\% \quad \text{3-1}$$

where C_r is the current capacity of the battery and C_m is the capacity of the battery at fully charged state. SOC varies from 0 % to 100 %; the former denotes that the battery is fully discharged, while the latter denotes that the battery is fully charged. In practice, the battery should work between 20%-80% to avoid overcharging and over-discharging [60]. Alternatively, SOC can be measured using the initial SOC and current of the battery [61]:

$$SOC(t) = SOC(t_0) - \int_{t_0}^{t} \frac{I(t)\eta}{C_m} dt \quad \text{3-2}$$

where $SOC(t)$ and $SOC(t_0)$ are SOCs at time t and t_0, respectively. η denotes the Coulombic efficiency that presents the ratio of the battery discharge capacity to the charge capacity during the same cycle. $I(t)$ is the charging/discharging current. The discrete representation of the above equation is as follows:

$$SOC_k = SOC_{k-1} - \frac{\eta \Delta T}{C_m} . I_k \quad \text{3-3}$$

where ΔT is the sampling time, and I_k is the loading current.

In fact, the SOC can be calculated using the above formulas; however, the inaccurate initial SOC and accumulated error in the current due to flawed measurement devices can lead to considerable estimation error in practical application. Therefore, growing attention has been paid to advanced methods for more precise SOC estimation [62].

SOC cannot be measured directly from inner quantities such as internal resistance and capacitance of the battery. As a result, external quantitative indices are utilized for SOC estimation [13], [63]. Myriads of literature propose various SOC estimation methods, such as the look-up table method, Coulomb counting method, data-driven, and model-based estimation methods. Figure 3-1 shows the different methods for the estimation of battery SOC.

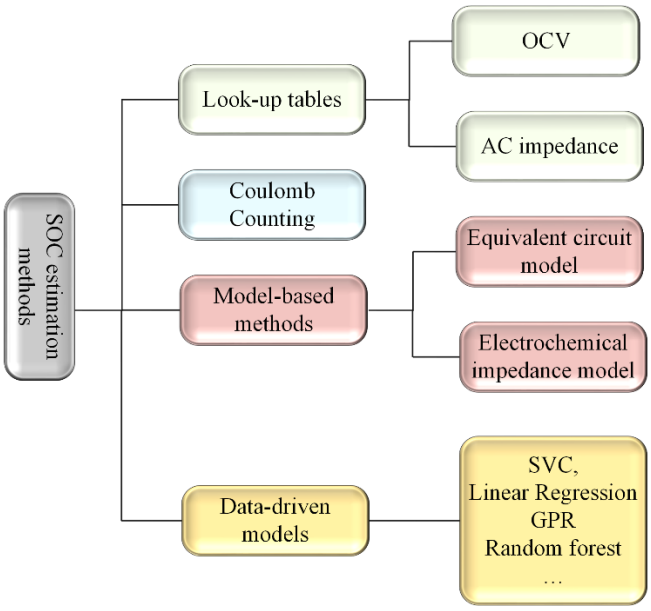

Figure 3-1. SOC estimation methods

SOC of batteries has a direct mapping relationship with their static characteristic parameters, such as the open-circuit voltage (OCV), impedance, etc. Thus, the SOC can be inferred by

measuring one or more parameters and then using the look-up table, which was built with the relationship between the SOC and the parameters, i.e., OCV or impedance [64]. Thus, knowing the OCV, SOC can be estimated through looking up the table between OCV and SOC. However, real-time usage of this method is very hard and cannot be utilized for a running EV, as the OCV should be measured while the battery is at rest for an extended period [11]. Moreover, the effect of temperature, material, hysteresis, and aging of the battery should be taken into account while measuring the OCV; otherwise, the measurement of SOC using this method does not lead to a reliable result [65]. There is also a relationship between impedance and SOC. When the current of a specific frequency is applied to the battery, multiple SOC-related parameters are identified by curve-fitting, then the impedance look-up table method is established [66].

The impedance parameters refer to internal ohmic resistance, polarization resistance, polarization capacitance, inductance, constant phase element, etc. [67]. The prediction error will be considerable if the amplitude of the impedance is small. The influence of aging, temperature, and current ratio should be taken into account in these methods for accurate estimation of SOC [65]. Thus, as mentioned, the main drawback of look-up table methods is that the battery should rest for a long-time period, and the accuracy of the methods is dependent on the accuracy of the SOC table.

As for Coulomb counting or ampere-hour counting (3-2 and 3-3), the SOC can be measured precisely if the initial SOC is known and the current of the battery can be measured accurately. There are three deficiencies with this method that should be dealt with. First, the initial SOC should be known. Second, the maximum available capacity of the battery should be recalibrated as it ages during its lifespan. Third, there are cumulative current measurement errors. Thus, this method is not considered as a highly accurate method for SOC estimation [11] [13].

In the model-based methods, ECMs and electrochemical models (EMs) are the major models derived from empirical data to predict the SOCs [68], [69]. ECMs and EMs are combined with various adaptive algorithms such as Kalman filter [70], [71], [72], extended and unscented Kalman filter [73], [74], central difference KF [75], [76], Particle filter (PF) [77], [78], and H-infinity observer [79], [80], to estimate or infer the internal state of the battery. Actually, the model-based methods are a kind of fusion method. They combine the ampere-hour method and looking-up table-based method through state equation of batteries. In such a case, the SOC of batteries provides a relationship between the ampere-hour method and the looking-up table-based methods. The terminal voltage of the battery can be estimated inaccurately if an imprecise SOC estimate calculated by the ampere-hour method brings an erroneous battery OCV. In such a case, if the best SOC is obtained, the minimum estimation error of battery terminal voltage can be obtained. In other words, the OCV can be used to correct the estimation error [11].

The EM is able to describe the macroscopic quantities such as cell current and voltage and local distribution on a microscopic scale for cell concentration, potential, current, and temperature [81]. The widely used EMs for battery SOC estimation are the one-dimension model [82] and the pseudo-two-dimensional model [83]. The single-particle model ignores the detailed distribution of local concentration and potential in the solution phase and instead accounts for a lumped solution resistance term. Forecasting methods based on the EM can provide insight into the effect of the kinetic process and charge transfer process in the battery. Identification of all parameters is difficult, although several simplifications have been made. Moreover, it needs high professional background. Thus, it is hard to be embedded in the BMS directly [11]. Figure 3-2 exhibits a general algorithm on how SOC is calculated in fusion-based methods. It is evident from Figure 3-2 that first, battery data, such as temperature and current, are sampled from the battery. Considering

EIM/ECM model of the battery and using initialized values for the model parameter and state-space equations the voltage of the battery is estimated. Then, the estimated voltage is compared with measured voltage and the output is utilized in filters algorithms to estimate the SOC of the battery.

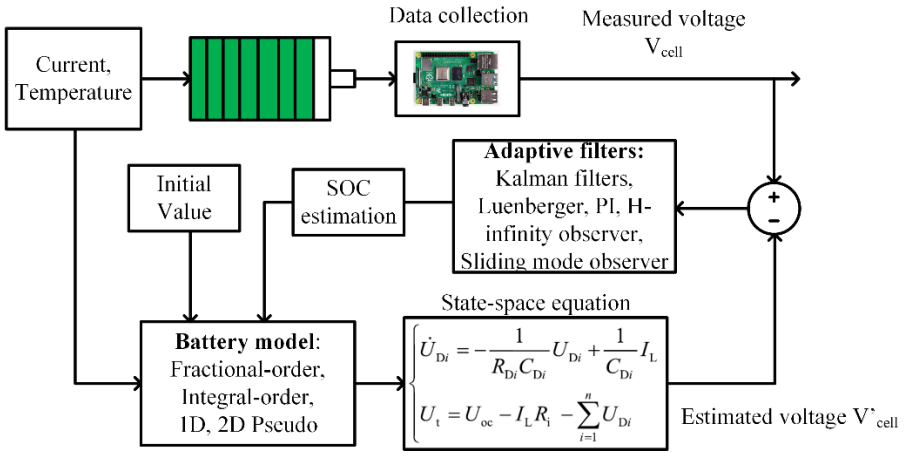

Figure 3-2. General algorithm for SOC estimation using EIM/ECM methods

As for the ECMs, they are divided into two categories, namely, integral-order equivalent circuit models and fractional-order equivalent models. Figure 3-3 shows a general diagram of the integral-order equivalent model. The simplest integral-order equivalent circuit model is the R_{int} model, which includes resistance in series with a voltage source [84]. The model structure of the R_{int} model is simple, but the polarization and diffusion phenomena are not considered. There is also literature considering different numbers of RC networks in their equivalent model in order to better model the dynamic and behavior of the battery, such as the charge and discharge process, to achieve better accuracy of the estimation [85], [86]. However, the more parameters are used in the model, the more intense the computational burden becomes. For the integral-order equivalent circuit models, the input/output relationship of the cell is easy to derive, and the models involve minor parameters. Therefore, the most commonly used approaches for online parameter

identification are the recursive least-squares methods [65]. The EIS and the bode plot are utilized to analyze the battery characteristics and to build the model structure. On the basis of the Bode plot obtained from EIS data, which will be fully explained in the next chapter, In the middle-frequency, the battery's Nyquist curve is not a standard semicircle, which means that the standard RC cannot simulate the battery behavior [65]. To address this issue, the constant phase elements can be used instead of the capacitors in RC networks. Figure 3-4 shows the diagram of the fractional-order equivalent model.

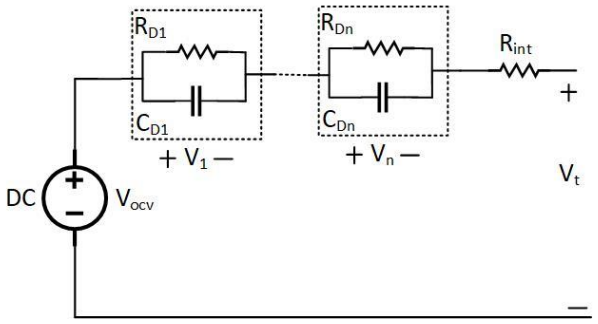

Figure 3-3. Integral-order equivalent circuit

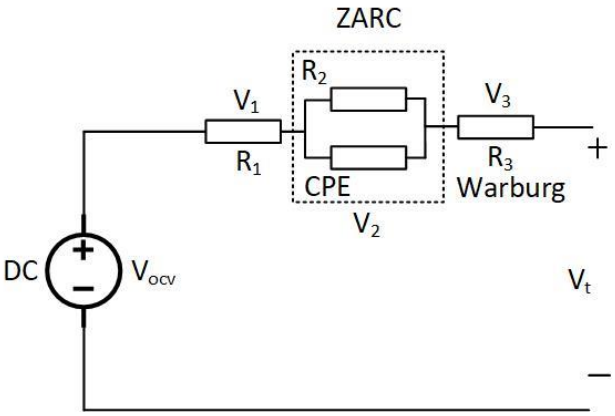

Figure 3-4. Fractional-order equivalent circuit

In [87], the relationship between SOC and the chemical composition of different types of batteries is studied. Then based on the proposed battery model, which utilizes the OCV and five other model parameters to make the closed-loop feedback system and to correct the error from

only using the OCV to estimate the SOC, the accurate prediction of SOC was estimated by adaptive extended Kalman filter (AEKF). The results indicated that the maximum error of SOC estimation is within 3%. Due to the fractional-order model having a better description of the battery behavior, the battery SOC was estimated by AEKF based on the fractional-order model. Moreover, the proposed fractional-order-AEKF can quickly track the unknown and time-invariant (or slow time-varying) noise variance and then improve the accuracy of SOC estimation [88]. A joint estimation method of SOC and capacity based on the AEKF multi-time scale framework is proposed in [89] to solve the problem of interference of current measurement offset to SOC estimation. The proposed method effectively increases the robustness and precision of SOC estimation. The maximum error of SOC estimation is found to be less than 3.3%. Moreover, electrochemical impedance spectroscopy measurements are utilized in ECMs to estimate SOC. In [90], the EIS data is derived only at one SOC, which prevents the model from being an inclusive model, but on the other hand, a wide range of temperatures is considered for modeling the battery based on ECM. The EIS data at above-zero temperature and SOCs between 10% to 90% and 10% to 100% have been derived in [91] and [92], respectively, which, however, decrease the accuracy and reliability of the estimation for SOCs at sub-zero temperatures and SOCs below 10%. Xu *et al.* [91] analyze the EIS data of a Li-ion battery. A fractional-order calculus modeling method is presented to be utilized as an impedance mode to estimate the SOC. The fractional Kalman filter is used to estimate the SOC based on the impedance model. The results indicate that the proposed estimation method based on the fractional-order model excels that based on the RC model. The estimated SOC of the proposed method can quickly converge to the reference SOC and trace it well with a small error confined to ±1%. However, the EIS measurement for the Li-ion battery has been obtained for SOCs between the range of 10% to 90% and at room temperature, and it does not cover a wide

range of temperatures.

Data-driven models are only dependent on historical data, and they do not need complicated equivalent or mathematical models. However, the challenge of data-driven models is the acquirement of informative inputs to construct a robust model for predicting the battery characteristics. Additionally, effective extraction of the features from historical data still remains a challenging task [93], [94]. In [95], different ML algorithms are employed to predict SOC, and a subtractive clustering-based adaptive neuro-fuzzy interface system architecture for electric vehicles SOC estimation under diversified driving cycles is proposed. In comparison with other advanced algorithms, such as the backpropagation neural network and Elman neural network, the proposed algorithm yielded better SOC estimation results. In addition, the sensitivity analysis results demonstrated that battery module temperature and heat removed from the battery are the most important parameters, while actual power loss has the least influence on SOC estimation for the subtractive clustering-based adaptive neuro-fuzzy interface system model. In another study [96], ML systems such as gradient tree boosting and multi-layer perceptron neural networks were applied in satellite lithium-ion battery sets for impedance estimation, which is used in the determination of their state of charge. Six different input features including F1- during the charge cycle, the time interval between the nominal voltage and the cut of voltage, F2- during the charge cycle, the time interval between the nominal current and the cut of current, F3- during the discharge cycle, the time interval between two predefined voltages, F4- average temperature during the time interval F1, F5- average temperature during the time interval F2, and F6- during the discharge cycle, cut off voltage are utilized for ML algorithms. The obtained root mean square error of both is found to be below 0.10. The gated recurrent unit-recurrent neural network (GRU-RNN) for SOC estimation of lithium-ion batteries is proposed in [97]. Battery variables such as voltage, current,

and temperature are employed as the input features to train the GRU-RNN network, while the SOC is used as the network output. A step-by-step searching strategy is provided to find the optimal GRU structure for SOC estimation. The impact of network parameters on SOC estimation is explored. The effectiveness of the proposed method was verified on the lithium-ion battery. Under varying temperatures, the root mean squared error (RMSE) of SOC estimation was less than 3.5% for the LFP battery. Three-layer and multi-hidden-layer wavelet neural network basing the Levenberg-Marquardt algorithm is used in SOC estimation, and they are optimized by PSO algorithm and a combining piecewise-network method, respectively [98]. Current, voltage, and the sign of current are used as input data for the proposed method. The maximum absolute error of the method is found to be less than 5%. The first-order RC model with one-state hysteresis is applied to model the dynamic response of a lithium-ion battery [99] . The parameters of the battery model are online identified by the dual AEKF algorithm. Aiming at the plateau region of the OCV-SOC curve, the dual AEKF and the ampere-hour counting with current correction are combined to estimate SOC. Then, the advanced data-driven algorithm, namely, the least square support vector machine (LS-SVM) as the advanced pattern of standard SVM, is employed to online predict the available capacity [99]. A five-element vector containing temperature, two impedance parameters, voltage change, and present voltage are utilized as the input feature data of the LS-SVM model. The parameters of the LS-SVM model are optimized by the genetic algorithm (GA) to reduce the capacity prediction error. The proposed capacity prediction and SOC estimation methods are finally coupled together to estimate SOC at different temperatures and aging levels of the battery, and the maximum RMSE is found to be less than 5%. The DNN is used in [100] to map the measured battery signals, such as voltage, current, and temperature, directly to SOC to estimate the SOC of the battery. Secondly, the DNN self-learns all its weights, which reduces the

computational burden and costly processes. In addition, the DNNs can eliminate measurement offsets and noise due to deficiencies in the vehicle's measurement devices and achieve great estimation performance. However, identifying and extracting reliable features become the main bottleneck of the adoption of the data-driven approaches, and thus, more research is required in this regard.

On the other hand, EIS measurements over a wide range of frequencies provide rich information about the dynamic characteristics of the battery and pave the way for precise estimation of the battery status. Nevertheless, none of the reviewed papers have adopted the EIS measurements directly as input data for ML models to predict SOC except for [101], in which the EIS data obtained for SOCs above 30% and at room temperature have been utilized in a deep NN. The model does not employ the EIS data in a wide range of temperatures and at different SOC points [101]. At the same time, such a data exclusion decreases the accuracy and reliability of the model. Also, the reported error of the model of [101] is less than 5%.

This chapter investigates the effectiveness of direct employment of the EIS measurements data as input features for estimating the SOC of the li-ion batteries using ML techniques. The proposed method’s advantages are higher accuracy of the models and lower computational burden by eliminating irrelevant input features, i.e., EIS impedances with low correlations. Therefore, highly correlated impedances are first identified and then extracted from EIS spectrum measurements obtained at SOCs from 0% to 100%. The chosen impedances are utilized as input features for the linear regression model and GPR. The models are designed to train the input features and establish the mapping relationship between the selected frequencies and the SOC. Finally, the trained models are employed to achieve SOC prediction. Moreover, since the ML algorithm is neither dependent on the model of the battery nor the method that the battery is charged/discharged, and

only the input and output of the dataset matter here, the model can predict the SOC by interpolating or extrapolating the dataset, regardless of charging or discharging mode of the battery. In contrast to many other studies that only take into account the EIS data obtained at above-zero temperatures, this study considers the EIS data for both above-zero and sub-zero temperatures, i.e., as low as -20 °C. The results demonstrate an error of less than 3.8 % for the GPR model.

3.2 EIS Experimental Data

In this chapter, the experimental data from [102] have been utilized, where a Panasonic NCR18650PF lithium-ion battery, an NCA chemistry cell similar to the cells used in Tesla's electric cars, was tested. The battery specifications have been presented in Table 3-1. In the test, EIS measurements were conducted over SOCs from 0% to 100% and a temperature range of -20 °C – 25 °C for frequency sweep of 1 mHz to 6 kHz.

Table 3-1. Panasonic 18650PF Cell Parameters

Nominal open circuit voltage	3.6 V
Min/Max Voltage	2.5 V / 4.2 V
Mass / Energy storage	48 g / 9.9 Wh
Capacity	2.75 Ah
Cycles to 80% Capacity	500 (100% DOD, 25 ℃)
Minimum Charging Temperature	10 ℃

Figure 3-5 shows the battery's impedance spectroscopy at different temperatures for the given SOC of 50 %. It can be observed from Figure 3-5(a) that the semicircle enlarges as the temperature decreases. It is due to the fact that the charge transfer rate decreases in the solid electrolyte interface (SEI) layer (or charge transfer resistivity increases), and in the electrode-electrolyte interface at

lower temperatures. Figure 3-5(b) shows that as the temperature decreases, the polarization resistance of the battery (where –Im Z = 0) increases due to a decrease in ion transfer in the electrolyte at lower temperatures.

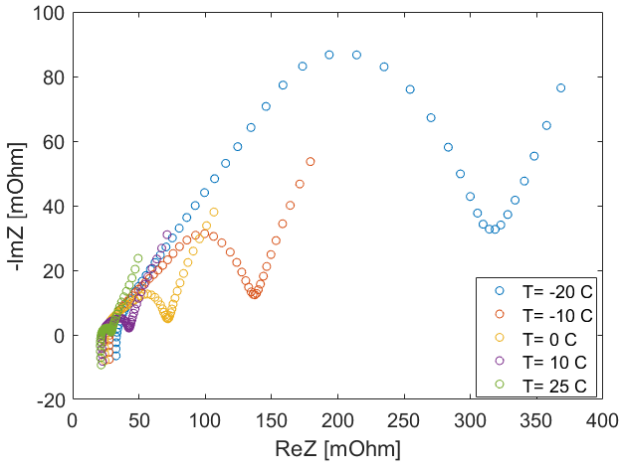

(a)

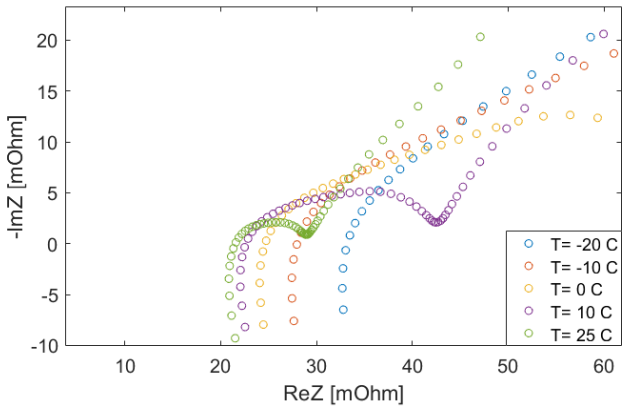

(b)

Figure 3-5. EIS spectrum of the battery at (a) SOC of 50% and different ambient temperature, (b) zoomed-in version of (a)

Figure 3-6 (a), Figure 3-6 (b), and Figure 3-6 (c) plot the EIS measurements of the battery at different SOCs and temperatures of +25 °C, 0 °C, and -20 °C, respectively. This figure manifests that at above zero temperatures, the SOC is less effective on impedance spectra, while at zero and sub-zero temperatures, SOC significantly affects the impedance curve, especially in the mid-

frequency regions. Thus, the effects of SOC on the impedance spectra at different temperatures are different. It is evident from Figure 3-6, that generally at any ambient temperature, the pure Ohmic resistance of the battery cell (where –Im Z = 0) including the Ohmic resistance of the components such as electrodes, electrolyte, and separator is decreasing as the SOC level increases. Typically, the semicircle enlarges and the impedances of low-frequency region increase as the SOC increases at above zero ambient temperature, however at very low SOC and at zero and sub-zero temperatures, the impedances of the mentioned regions are extremely higher, and it has its roots in very low diffusion of Li ions and charge transfer conductivity at low temperatures.

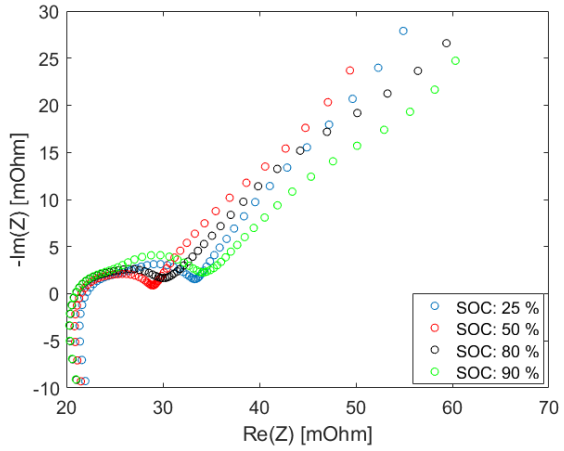

(a)

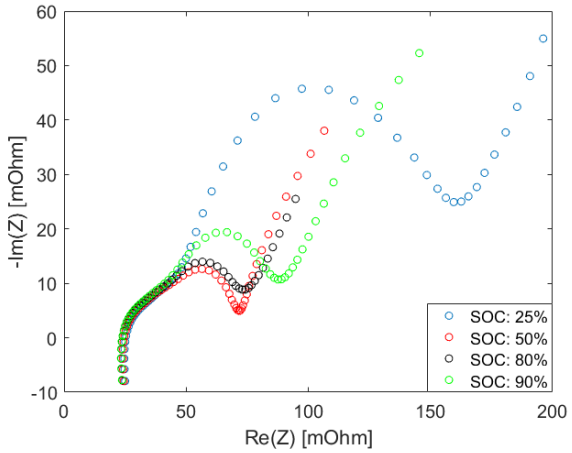

(b)

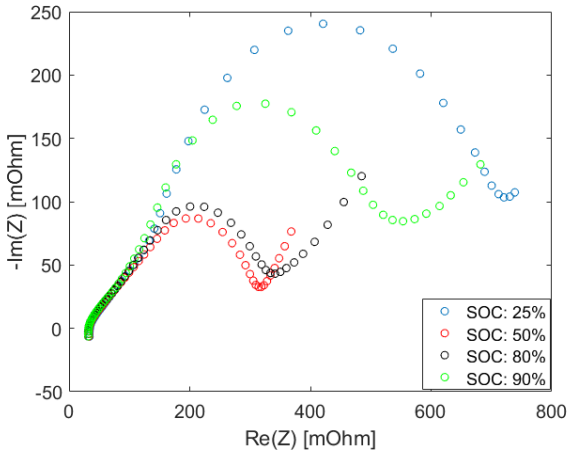

(c)

Figure 3-6. EIS spectrum of the battery at (a) 25 °C, (b) 0 °C, and (c) -20 °C and at different SOC levels

3.3 Methodology

This section is dedicated to the feature sensitivity analysis to capture the highly correlated EIS features, i.e., highly correlated EIS impedances with SOC of the battery, and then the selected reliable features are utilized for training and testing of the ML models.

3.3.1 Feature sensitivity analysis

Extracting highly relevant features to the ML models' output, i.e., SOC, is essential for accurately predicting the output. To this end, the correlation matrix, which indicates the dependency of two or more variables on each other, is calculated and then shown on a color-coded image plot. The calculation of the correlation is performed by the Pearson correlation coefficient as follows:

$$\rho_{X,Y} = \frac{E(X,Y) - E(X)E(Y)}{\sqrt{E(X^2) - E(X)^2}.\sqrt{E(Y^2) - E(Y)^2}} \quad 3\text{-}4$$

where E is the expected value operator, and X and Y are two random variables. Figure 3-7 is a 2-D graphical representation that indicates the dependency of the features of the dataset. The features

in the used dataset are electrochemical impedances at the corresponding frequencies that they were measured. In this case, the number of the features is 54 since the impedances were measured at 54 frequencies, sweeping from 1mHz to 6kHz. In Figure 3-7, the correlation between the features varies from -1 to 1. The positive correlation has been shown in the spectrum of light to dark red, and the negative correlation has been shown in the spectrum of light to dark blue. The positive and negative correlations mean that the output varies in the same or opposite direction of the input variables' variations. The heatmap is a symmetric figure; thus, the last row or the last column represents the relation of the input variables, i.e., impedances at different frequencies with the output, i.e., SOC of the battery. Figure 3-7 shows the heatmap of the dataset at temperatures of (25 °C) – (-20 °C), respectively. Figure 3-7 (a) shows that the first few features are highly and negatively correlated with the SOC and these features lie in the high and mid-frequency regions of the EIS spectrum. The negative correlation of the high frequency impedances is in accordance with what has been explained for Figure 3-6. As also depicted in Figure 3-7 (a), it is apparent from Figure 3-7 (b)-(e) that as the temperature decreases, some other features from mid-frequency appear to be positively correlated with the SOC. Another remarkable result deduced from Figure 3-7 is that the low frequencies are significantly less correlated with the SOC. The reason is that according to Figure 3-5 and Figure 3-6, the number of features, i.e., EIS impedances at lower frequencies, is significantly less than the number of features at higher frequencies. In other words, most of the EIS impedances which have lower magnitudes exist in all of the conditions in Figure 3-5 and Figure 3-6, and they lie in high and mid-frequency regions; however, the EIS impedances with larger magnitudes only exist in extreme conditions, i.e., at the temperature of -20 °C in Figure 3-5 and SOC of 20% in Figure 3-6. Therefore, heatmaps are useful for extracting reliable features to build an accurate and fast model for prediction purposes. Moreover, a pairgrid plot is also

utilized to show the relationships of highly correlated features obtained from the heatmap with the SOC and their distribution in the dataset. Only four high-correlation features f1, f2, f4, and f5 have been shown as examples at 25 °C. The diagonal plots represent the distribution of single-variable and off-diagonal plots, which are mirror image of each other and show the relations between every two variables of the dataset along with the regression plots. It is worth noting that Figure 3-8 shows only the negatively correlated features with the SOC at different temperatures. It is observed that with the increase of features f1, f2, f4, f5 in magnitude, the SOC decreases. Therefore, feature analysis helps identify the most influential features that contribute to the variation of the output variable.

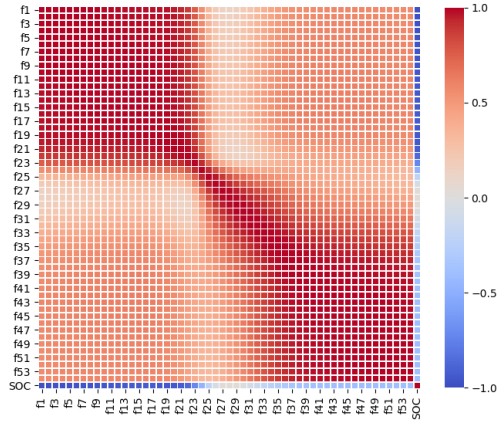

(a)

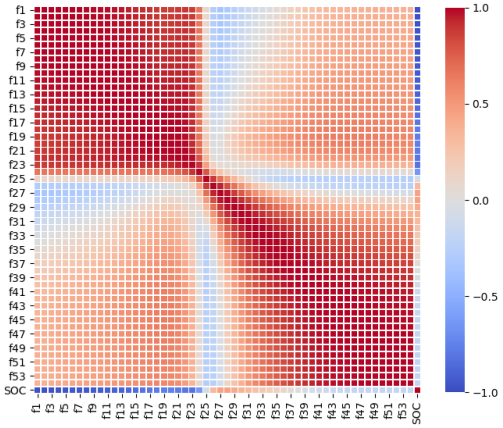

(b)

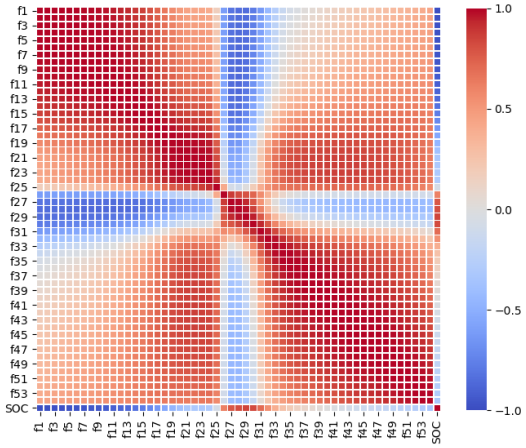
f1
f3
f5
f7
f9
f11
f13
f15
f17
f19
f21
f23
f25
f27
f29
f31
f33
f35
f37
f39
f41
f43
f45
f47
f49
f51
f53
SOC
1.0
0.5
0.0
−0.5
−1.0

(c)

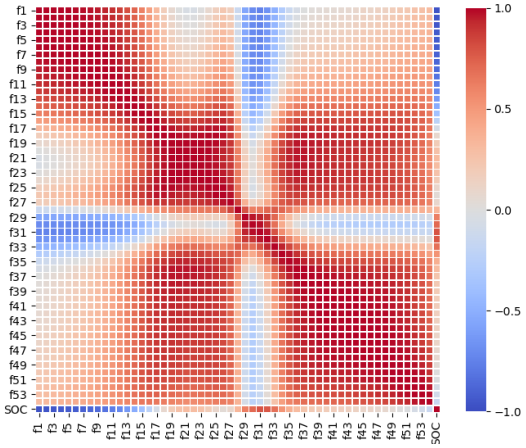
f1
f3
f5
f7
f9
f11
f13
f15
f17
f19
f21
f23
f25
f27
f29
f31
f33
f35
f37
f39
f41
f43
f45
f47
f49
f51
f53
SOC
1.0
0.5
0.0
−0.5
−1.0

(d)

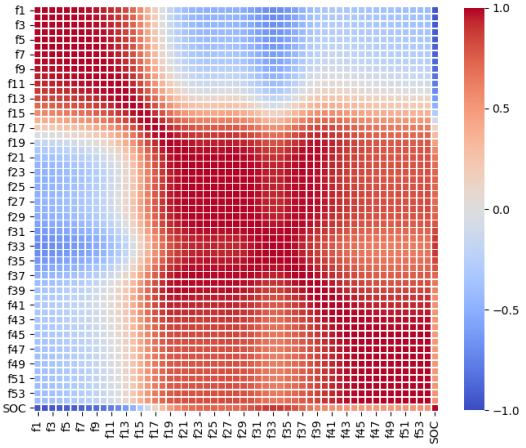
f1
f3
f5
f7
f9
f11
f13
f15
f17
f19
f21
f23
f25
f27
f29
f31
f33
f35
f37
f39
f41
f43
f45
f47
f49
f51
f53
SOC
1.0
0.5
0.0
−0.5
−1.0

(e)

Figure 3-7. Heatmap for feature sensitivity analysis of EIS spectrum at (a) 25 °C. (b) 10 °C, (c) 0 °C, (d) -10 °C, (e) -20 °C

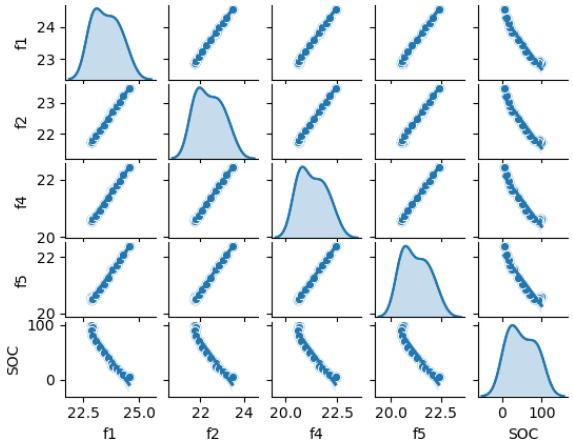

(a)

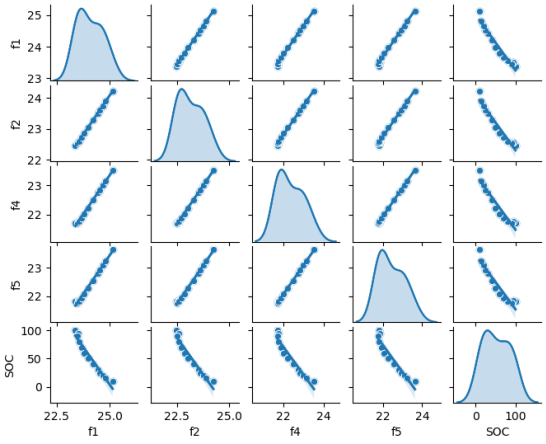

(b)

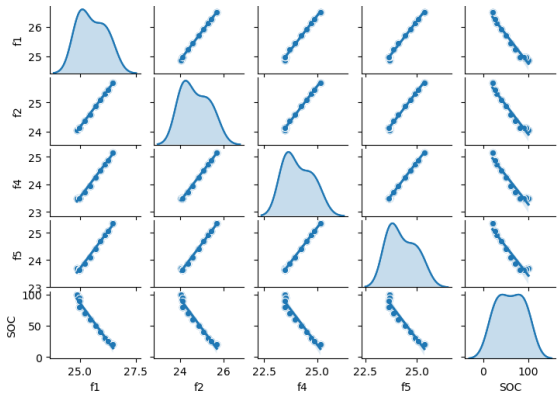

(c)

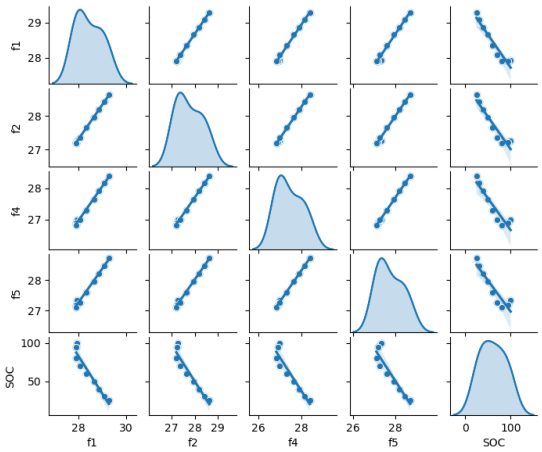

(d)

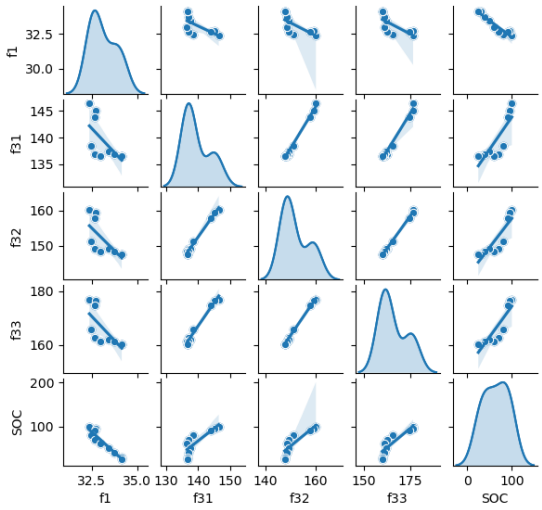

(e)

Figure 3-8. PairGrid for reliable features of EIS spectrum at (a) 25 °C, (b) 10 °C, (c) 0 °C, (d) -10 °C, (e) -25 °C

3.3.2 Linear regression algorithm

A linear regression algorithm is used for identifying the relationship between a dependent variable and one or more independent variables. In this case, the impedances at different frequencies are the independent variables, and the SOC is the dependent variable. The basic multiple regression model of a dependent variable Y on a set of k independent variables (x_k) can

be expressed as [103]:

$$\begin{cases} y_1 = \beta_0 + \beta_1 x_{11} + \cdots + \beta_k x_{1k} + e_1 \\ y_1 = \beta_0 + \beta_1 x_{21} + \cdots + \beta_k x_{2k} + e_2 \\ \vdots \\ y_n = \beta_0 + \beta_1 x_{n1} + \cdots + \beta_k x_{nk} + e_n \end{cases} \quad 3\text{-}5$$

Therefore:

$$y_i = \beta_0 + \beta_1 x_{i1} + \cdots + \beta_k x_{ik} + e_i \quad 3\text{-}6$$

where y_i is the i_{th} case of the dependent variable Y, x_{ij} is the value of the j_{th} independent variable (X_j) for the i_{th} case of the dependent variable, β_0 is the Y-intercept of the regression surface, each β_j is the slope of the regression surface with respect to variable X_j, and finally, e_i is the random error component for the i_{th} case. In each equation in 3-5 , the error is distributed with zero mean and standard deviation, and it is independent of the errors in the other equations. Since the variables are fixed quantities, the randomness of Y results from the randomness of error terms in each equation; although, in terms of correlation, the input variables are taken into account random variables, and the input variables are independent of the error terms. In matrix notation, 3-5 can be written as:

$$Y = X\beta + e \quad 3\text{-}7$$

where:

$$Y = [e_1\ e_2\ \ldots\ e_n]^T \quad 3\text{-}8$$

$$\beta = [\beta_1\ \beta_2\ \ldots\ \beta_{k+1}]^T$$

$$X = \begin{bmatrix} x_{11} & \cdots & x_{1(k+1)} \\ \vdots & \ddots & \vdots \\ x_{n1} & \cdots & x_{n(k+1)} \end{bmatrix}$$

where Y is the target vector, e is the error vector, which is a column vector of length n, and β is

the vector of parameters, which is a column vector of length $(k+1)$. Matrix X is the input matrix, which is n by $(k+1)$ matrix. To do the estimation, β and e should be calculated. The structure of the regression model has been shown in Figure 3-9.

3.3.3 Gaussian process regression

For a given training dataset of $T = \{(x_i, y_i), i = 1, 2, \dots, n\}$ with *n* pairs of inputs x_i, which may have one or more than one features, and output y_i, the GPR model computes the predictive distribution of unobserved test datasets with y^* as output and x^* as input [8]. In this study, *X* and *Y* are defined as $X = [x_1, x_2, \dots, x_n]^T$ and $Y = [y_1, y_2, \dots, y_n]^T$, respectively. In this case, $x_i = [EIS\ impedances]$ is the EIS impedances and the output y_i is the SOC of the cells. It is also assumed that $y_i = f(x_i + \varepsilon_i)$ where $\varepsilon_i \sim \aleph(0, \sigma^2)$ is an independent and identically distributed Gaussian noise. The outputs $F = (f(x_1) + \cdots + f(x_n))$ are modeled as Gaussian random field $F \sim \aleph(0, K)$ where $K_{ij} = k(x_i, x_j)$ is the covariance kernel. In this case, the radial basis function is utilized for covariance kernel as well. The joint distribution of the training dataset $\{(x_i, x_j), i = 1, 2, \dots, n\}$ and the predicted test output (x^*, y^*) is:

$$\begin{bmatrix} Y \\ y^* \end{bmatrix} = \aleph\left(0, \begin{bmatrix} K(X,X) + \sigma^2 I & K(X,x^*) \\ K(x^*,X) & K(x^*,x^*) \end{bmatrix}\right) \quad 3\text{-}9$$

Conditioning on the training set yields the predicted mean on x^*:

$$\bar{y}^* = K(x^*,X)(K(X,X) + \sigma^2 I)^{-1} Y \quad 3\text{-}10$$

And its predicted variance is:

$$\Delta^2 = K(x^*,x^*) - K(x^*,X)(K(X,X) + \sigma^2 I)^{-1} K(X,x^*) \quad 3\text{-}11$$

The linear regression model is chosen since the computational costs for SOC estimation is low; as a linear model using EIS measurements to estimate the SOC, its performance should be investigated.

GPR is also utilized as this model learns from the dataset itself and estimates the output SOC by interpolating the observed (training) datasets. Moreover, GPR's accuracy is investigated as a non-linear model using EIS measurements for SOC estimation.

3.3.4 Data preparation

To avoid the malfunction of the ML models over a new dataset, the dataset should be split into two partitions, i) training set and ii) test set. The training set is used to construct the models and contains known output. The ML models are fitted to the training data and calculate the regression coefficients. Then, the test set is utilized to observe the performance of the ML models over unknown data. This implies that the test set serves as a criterion for the evaluation of the model predictions. In contrast to many other studies, the effect of different test-size (TS) is observed in this study for the dataset with the selected features and different correlation values.

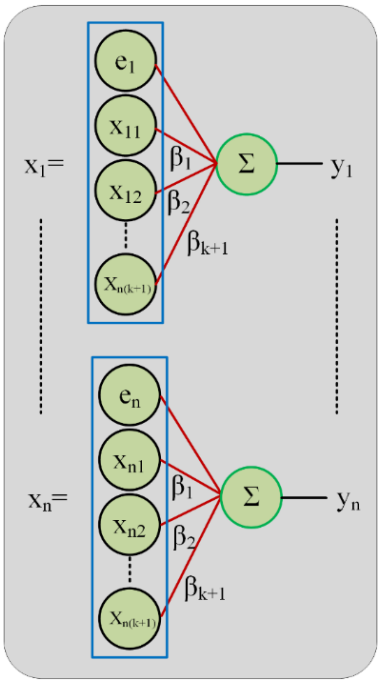

Figure 3-9. Linear regression structure

3.3.5 Accuracy estimation

The indices used for the evaluation of the performance of the proposed models are:

- R-squared:

Goodness-of-fit R-squared (R-squared) is defined as:

$$R^2 = 1 - \frac{\sum_{i=1}^{n}(y_i - \hat{y}_i)^2}{\sum_{i=1}^{n}(y_i - \bar{y}_i)^2} \quad 3\text{-}12$$

where y_i is the actual value, $\bar{y}_i$ is the mean value, and $\hat{y}_i$ is the predicted value for the i_{th} case. $R2$ ranges between 0 and 1. The closer to 1, the better the goodness of the fit.

- Mean absolute percentage error (MAPE)

MAPE is used to compare the precision of the prediction and is defined as follows:

$$MAPE = \frac{100}{n}\sum_{i=1}^{n}\left|\frac{y_i - \hat{y}_i}{y_i}\right| \quad 3\text{-}13$$

The smaller the MAE, the better the estimation.

- Root mean squared error

The root square of the above equation provides the standard deviation of the random error term. Root mean square error is an estimate of the standard deviation of the random component in the data and is defined as follows:

$$RMSE = \sqrt{\frac{\sum_{i=1}^{n}(y_i - \hat{y}_i)^2}{n}} \quad 3\text{-}14$$

3.4 Results and Discussions

In this study, Python and MATLAB have been harnessed to perform the statistical analysis and prediction of the SOC. Figure 3-10 shows the flowchart of the proposed methodology for predicting the SOC of the battery using EIS measurements. In this section, the models' performance at

different temperatures is discussed, considering the effect of reliable features extraction based on their correlation value and portioning of the dataset. The statistical evaluation indices discussed in the previous section have been recorded in Table 3-2 in different conditions.

As mentioned earlier, some datasets have been introduced to the ML models with different portioning. The default portioning is that 80% of the dataset is dedicated to the training set, and 20 % (test_size = 0.2) is dedicated to the test set. However, to see the effect of TS, other values for this variable have also been taken into account. For corr_value of 0.5, different evaluation indices have been obtained at different temperatures, as presented in Table 3-2. The linear regression model can perfectly predict the battery's SOC based on the values of R-squared, MAPE, and RMSE at the mentioned temperatures except for 10 °C and 0 °C. The MAPE for 25 °C, -10 °C, and -20 °C temperatures is less than 4.9%, but for 10 °C and 0 °C, the MAPEs are 8.9% and 17.5%, respectively. Moreover, it is clear that for TS of 0.4, the highest accuracy is achieved for temperatures 10 °C and 0 °C. As for the corr_value of 0.7, we can observe that for the temperatures of 25 °C, -10 °C, and -20 °C, the evaluation indices values have not changed significantly. However, in the cases of 10 °C and 0 °C temperatures, the improvement of evaluation criteria is noticeable such that the MAPEs have reduced to 5.5% and 9.7%, respectively. Moreover, one may observe the influence of TS on the mentioned temperatures, as the TS increases, an increase in R-squared and a reduction in MAPE and RMSE are observed. Considering the corr_value of 0.9, the MAPE for all the cases is achieved with a value of less than 7%. Since the extracted features are reliable, it is expected that the MAPE and RMSE decrease, but on the contrary, they increase. This is because when highly correlated features are selected, most of the other features are lost, and the ML model may lose accuracy if the dataset is not big enough. Thus, the performance of the model over a dataset is of importance. Although the linear regression model functions properly for corr_values of 0.9, with

a maximum error of 7%, a more accurate and reliable model, i.e., GPR, is used for this corr_value. The GPR model results for corr_value of 0.9 and the best TS have been presented in Table 3-2. The MAE for 25 °C, -10 °C, and -20 °C temperatures is less than 2.8%, but for 10 °C and 0 °C, the MAEs are 3.8% and 8.7%, respectively. As an example, the training and test data and their predicted values at different temperatures have been shown in Figure 3-11.

The study results demonstrate that in addition to identifying and extracting reliable features, the learning ability of the model and partitioning of the data for training are highly crucial for precise prediction. Considering the above-mentioned elements' effects, we also observed that the GPR model outperforms the linear regression model.

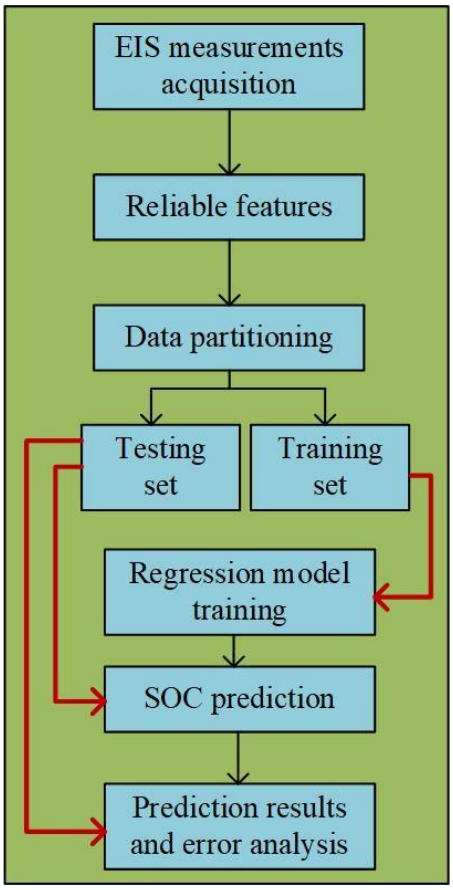

Figure 3-10. Algorithm of the proposed model for predicting the SOC of the battery using EIS measurements

Table 3-2. Evaluation indices under different conditions

ML Model	Corr_value	Temp (°C)	R-squared	MAPE(%)	RMSE
Linear Regression	0.5	25 (TS=0.2)	0.978	4.84	5.99
		10 (TS=0.2)	0.742	8.93	20.098
		0 (TS=0.4)	0.62	17.44	20.098
		-10 (TS=0.2)	0.989	2.90	3.3387
		-20 (TS=0.2)	0.982	4.23	4.3
Linear Regression	0.7	25 (TS=0.2)	0.975	4.845	5.99
		10 (TS=0.4)	0.698	9.546	17.913
		10 (TS=0.6)	0.942	5.562	8.44
		0 (TS=0.4)	0.734	13.66	16.797
		0 (TS=0.5)	0.876	9.73	11.48
		-10 (TS=0.2)	0.987	3.0525	3.602
		-20 (TS=0.2)	0.977	4.9398	4.842
Linear regression	0.9	25 (TS=0.2)	0.952	6.27	8.27
		10 (TS=0.4)	0.782	15.23	17.69
		10 (TS=0.6)	0.899	6.99	11.216
		0 (TS=0.4)	0.4345	15.09	24.528
		0 (TS=0.5)	0.8785	9.087	11.38
		0 (TS=0.6)	0.925	6.91	8.87
		-10 (TS=0.3)	0.982	3.23	3.56
		-20 (TS=0.5)	0.875	6.55	9.98
		-20 (TS=0.6)	0.93	6.11	6.88
GPR	0.9	25 (TS=0.2)	0.998	1.34	1.46
		10 (TS=0.4)	0.981	3.81	4.4
		0 (TS=0.3)	0.903	8.68	9.96
		-10 (TS=0.3)	0.983	2.72	3.45
		-20 (TS=0.2)	0.988	2.74	3.55

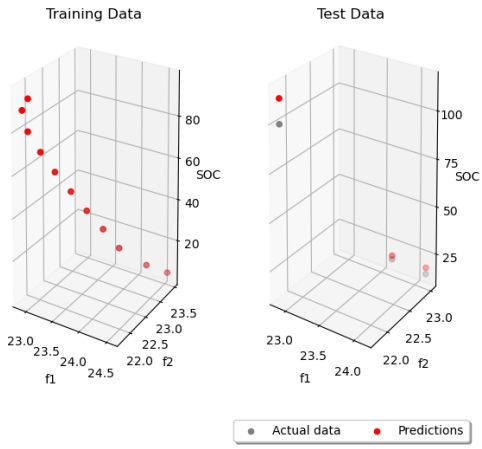
Training Data
Test Data
SOC
f1
f2
Actual data
Predictions

(a)

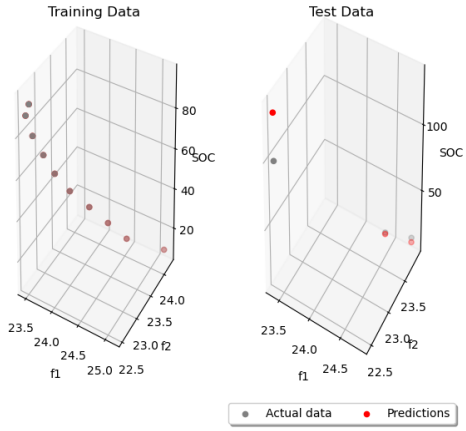
Training Data
Test Data
SOC
f1
f2
Actual data
Predictions

(b)

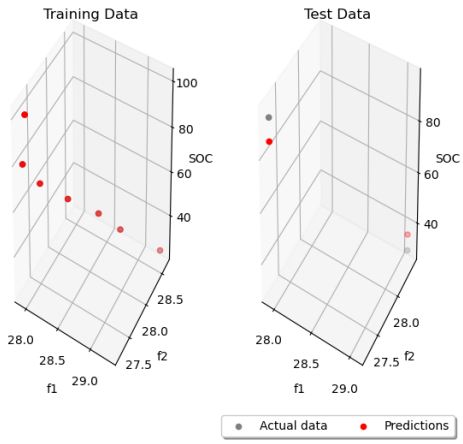
Training Data
Test Data
SOC
f1
f2
Actual data
Predictions

(c)

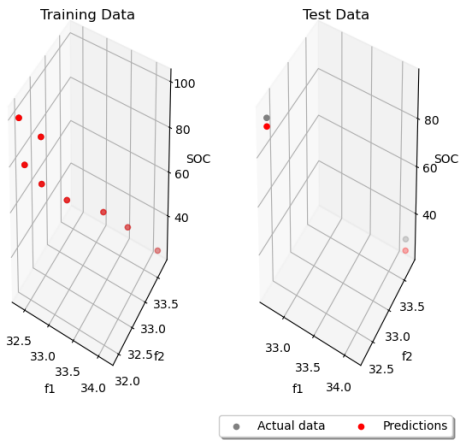

(d)

Figure 3-11. SOC prediction of the proposed model at temperatures of (a) 25 °C, (b) 10 °C, (c) -10 °C, (d) -25 °C

3.5 Conclusions

In this investigation, the prediction of li-ion battery SOC using EIS measurements was performed based on an ML approach. This study was conducted based on extracting reliable features according to their correlation value with the SOC of the battery. The features are the impedances of EIS measurements over the range of desired frequencies, i.e., from 1 mHz to 6 kHz. After selecting the reliable features of different datasets at various temperatures and different SOCs, the linear regression model and GPR were trained, and the prediction was performed by the trained models over the test set. Statistical indices such as R-squared, MAPE, and RMSE were used to evaluate the accuracy and robustness of the models. The results indicated that the proposed models are able to precisely predict the SOC of the battery using the reliable features. The models trained by the features with a corr_value of above 0.9 indicated the best performance among the others, such that the error of the GPR model was found to be less than 3.8 %. Furthermore, the impact of test-size on the model precision was evaluated. It was observed that for some cases, the larger test-size results in higher accuracy.

Chapter 4

SOH Estimation

4.1 Introduction

One of the main functions of BMS is to estimate the capacity accurately and, ultimately, the SOH of the battery and control the charge-discharge cycle and thermal behavior of the battery [104], [105], and [106]. The cell SOH is defined as the ratio of the cell capacity in the current stage of operation to its initial capacity or the rated capacity provided by the cell manufacturer. Therefore, if the calculated capacity is divided by the constant value of the initial capacity, SOH is provided. It implies that the capacity and SOH of the battery can convey the same meaning and can be used interchangeably. SOH is calculated by the following formula:

$$SOH = \frac{C_a}{C_{rated}} \times 100\% \qquad 4\text{-}1$$

where C_a is the cell capacity at current stage of operation and C_{rated} is the nominal capacity of the cell.

The effective estimation of the above measure is the topic of this chapter. Estimation of SOH is studied and implemented historically using three methods. These methods are grouped under direct calibration, model-based, and data-driven in approach and methodology [107].

Direct calibration methods calculate the battery SOH through specific empirical operations. For example, fully discharging the battery after a complete charge [108]. Direct calibration

methods are relatively easy to implement. However, acquiring precise current and voltage in an open-loop approach is of great challenge. In order to address the restrictions of direct calibration methods, model-based methods relate the measured battery data such as voltage, current, temperature, and EIS to the SOH based on equivalent electrical or electrochemical models [109], [110], [111]. The model-based methods are often used in combination with observers or adaptive filters algorithms such as EKF [112], [113] [114], PF [115], and H-infinity filter [116] to achieve online capacity estimation. Zhang *et al.*[117] used the Markov chain Monte Carlo algorithm to address sample starvation in the improved unscented PF (IUPF) algorithm. Since the IUPF is proposed based on the PF, it can attenuate the particle's existing degradation in the standard PF to increase the precision of the model. An EKF along with dual fractional-order is utilized for capacity estimation [118]. In [119], GA and recursive least square are employed to get the internal resistance of the battery based on ECM. Moreover, to track the internal resistance under various depth of discharge, pulse approaches have been adopted in [120]. Then, the mapping between the real-time resistance and the maximum and minimum resistances determines the capacity of the battery. The performances of EKF, PF, and recursive least squares in terms of precision and computational burden were compared in several studies and analyzed for accuracy [121]. However, building a precise battery model is a daunting task since it requires a large amount of physical knowledge or experimental data under sophisticated designed and well-controlled circumstances to be effective. Moreover, due to the internal complex chemical reaction process and uncertain external operating conditions of the batteries, achieving sufficient model precision remains a challenge for the above model-based methods.

Data-driven models can aid in providing the data needed in the model-based approach as they do not need mathematical expressions to connect the battery signals to capacity or SOH estimation,

and the relationship can be constructed by training the historical data. Li *et al.* [122] proposed a study using a GPR-based method to predict the battery SOH using the health features extracted from partial incremental capacity (IC) curves. IC-values are utilized in [123] for capacity estimation from cell level to battery pack level. Feng *et al.* [124] developed an SVM-based online SOH estimation method. The SVM model is first implemented offline, utilizing features extracted from the battery charging curves of cells at different SOHs. The SOH is predicted by comparing the features of the measured signals and the stored models. Guo *et al.* [125] extracted health features such as the area under the current curve/temperature curve of constant current (CC) phase/constant voltage (CV) phase/whole charge process, CC time, CV time, the ratio of CC time to CV time, the ratio of area under temperature curve to the corresponding area under the current curve, and the maximum slope of the current curve in CC phase/CV phase from charging measurements, and they are used as the inputs to a relevance vector machine (RVM) model. Hu *et al.* [126] manually choose five cell features that are representative of the cell capacity from partial charge and then utilize RVM to build a relationship between the selected features and the battery capacity. The proposed RVM model, after being trained offline, was applied to online estimate the capacity of a battery cell based on the five selected charge-related. In [127], a data-driven method has been developed to estimate the capacity of the battery using charge voltage and current curves. In this approach, the k-nearest neighbor is adopted to establish the relationship between the capacity and charge-related factors, and PSO is employed to the parameters of the k-nearest neighbor. Bai *et al.* [128] adopted an NN to estimate the terminal voltage, and then the method is used along with a dual EKF for online capacity estimation. In another study [129], the IC peaks, IC valleys, and their corresponding voltage values are used as the features to estimate battery SOH. The drawbacks of these methods are two-fold: (1) the redundancy of health features is not

considered, which will lead to over-fitting and low accuracy of the model, (2) these methods are dependent on the manually extracted features provoking significant computational efforts, which becomes impractical. To tackle this issue, deep learning algorithms have recently attracted much attention due to their ability to extract features automatically. You *et al.* [130] proposed a recurrent neural network (RNN) model using long short-term memory (LSTM). The model takes the current and voltage data during a charge cycle as its input. Shen *et al.* [131] proposed a deep convolutional neural network (DCNN) model for cell-level capacity estimation based on the voltage and current measurements during a partial charge cycle. The performance of a feed-forward neural network, LSTM, and CNN for capacity estimation have been compared in [132], and the test results indicated the difficulty of the resultant models in coping well with limited battery data on hand. It can be concluded that these data-driven models have proven significant potential in capacity prediction, yet their performance can be alleviated if they are not trained with sufficient datasets. Only models trained with enough data can achieve satisfactory precision. In turn, obtaining a large dataset for degrading batteries requires many cycling tests, which is highly time-consuming and costly. Moreover, in another situation where the operating conditions are different, new datasets should be recollected, and models should be retrained again to achieve desired efficacy.

Given this background, TL technique can be associated with these methods to improve the prediction performance on a small or unknown dataset. In this case, knowledge extracted from a related domain can be utilized to assist an ML algorithm performs better in the target domain. In [133], the battery health was estimated by combining the kernel ridge regression and TL to improve the prediction accuracy. The input features were collected from the charge/discharge and IC curves of four battery cells from the NASA battery degradation dataset. In [108], TL was applied to achieve accurate prediction based on an LSTM model. The features of this article were obtained

only based on the voltage data of the CC charging process. A CNN model combining the concepts of TL and ensemble learning was used for capacity estimation in [134], with voltage, current, and charge capacity as the network's inputs. In [135], the CNN model combined with TL utilizes voltage, current, and charge capacity as input variables. A fixed length of 225 data points and a flexible starting point are directly used as the model inputs and are generated by a signal-to-image transformation to estimate the battery capacity using only partial charging segment. Shu *et al.* [136] have combined TL and LSTM for SOH prediction using partial voltage data acquired from the voltage curves during the CC charging process and the specified charging interval for the pre-set voltage range as the input of the base model.

To this end, the reviewed studies have employed different input features, among which many of them are dependent on IC curves and the charging process, such as CC-CV, CC, or CV, for SOH or capacity prediction of batteries. In contrast, scant attention has been given to one of the most information-rich datasets, EIS, for the same purpose. Although there is literature employing equivalent electrochemical models using EIS for capacity prediction [137], [138], and [139], there are very few studies that adopt EIS measurement directly as an input feature for SOH estimation [8]. This chapter proposes a DNN in conjunction with TL for capacity estimation of Li-ion batteries adopting EIS measurement directly as input features without further computational algorithms to extract additional features such as the ones mentioned for IC curves and the CC-CV charging process. The contributions of our research are three-fold: (1) contrary to the reviewed literature that only considers the datasets for a fixed temperature, this paper takes the different operational temperatures of degrading batteries into account such that the model can predict the capacity of the battery for out-range temperatures. (2) the effect of the number of fixed layers, i.e., non-trainable layers of the pre-trained model adopted in TL, is examined on the target dataset. (3) the

effect of the target dataset's size to foster our proposed DNN-TL model is also investigated, resulting in a DNN-TL model that is retrained only based on the first 50% and 20% of the target dataset, and subsequently, the results are compared to the stand-alone DNN model.

4.2 EIS Experimental Data

The experimental data from [8] has been utilized in this study. The experiment applies a continuous charge-discharge cycle on 12 commercially available 45 mAh Eunicell LR2032 Li-ion coin cells. The cell chemistry is LiCoO2/graphite. The cells are cycled in three climate chambers set to 25 °C (25C01–25C08, Cells' number from 01 to 08 at 25 °C), 35 °C (35C01 and 35C02, Cells' number from 01 to 02 at 35 °C) and 45 °C (45C01 and 45C02, Cells' number from 01 to 02 at 45 °C), respectively. Each cycle consists of a 1C-rate (45mA)(1C-rate indicates that the 1A discharge current will discharge the entire battery in 1 hour.) CC-CV charges up to 4.2 V, and a 2C-rate (90 mA) CC discharges down to 3 V [8]. EIS is measured at nine different stages of charging/discharging during every even-numbered cycle in the frequency range of 0.02 Hz–20 kHz with an excitation current of 5 mA [8]. However, in our study, we use the EIS measurement at two stages, i.e., before the onset of charging and after 15 minutes rest of charging process at the state of charge (SOCs) of 0% and 100 %, respectively. The loss in capacity is determined after every odd-numbered cycle.

We use the EIS and capacity datasets of 10 cells out of the 12, i.e., 25C01–25C03, 25C05-25C07, 35C01-35C02, and 45C01-45C02 cells. The datasets and implementation details section will extensively discuss how to divide the datasets into the training and testing groups to gain insight.

It is evident from Figure 4-1 that the EIS characteristic differs from each other at different

temperatures and lifetime levels. In Figure 4-1, “New” means when the battery cell EIS is measured at its first cycle (100% of initial capacity), “Middle age” means when the battery cell EIS is measured at middle cycles, and “Old” means when the battery cell EIS is measured at its end of life as energy storage for electric vehicles (usually 80% of its initial capacity). The research goes well beyond the pure resistance of the battery, i.e., the intersection of EIS with the x-axis increases and takes into consideration the semicircle and the tail part of EIS enlarge. This indicates that EIS at different temperatures and lifetime levels provides rich information about the battery's capacity and can be considered a potential criterion for the capacity prediction of batteries during their longevity.

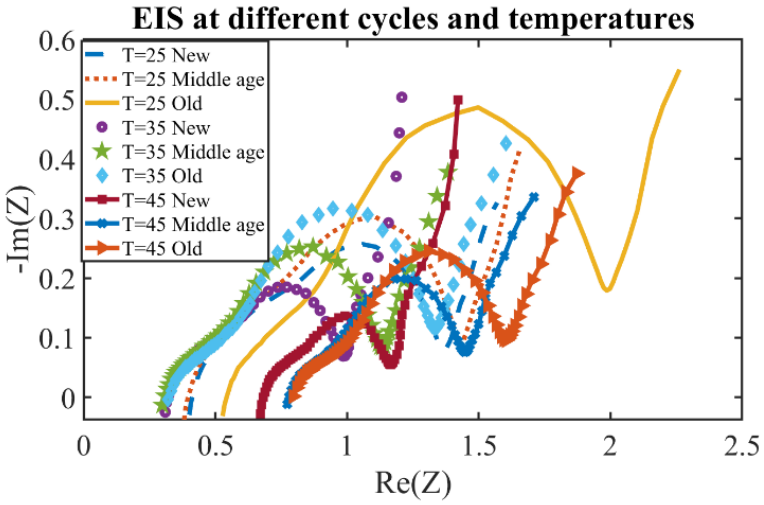

Figure 4-1. EIS at different cycles and temperatures

4.3 Methodology

4.3.1 Deep neural network

DNN is a supervised learning requiring the output and input data for the training and the prediction. DNN model has been adopted in this study to investigate its capability in capturing the EIS measurements patterns at different aging and ambient temperature levels for SOH or capacity

estimation of li-ion battery cell. The number of hidden layers and neurons can be determined based on one's needs. The weights between the layers are first initialized ad hoc and then adjusted continually during training [140]. Figure 4-2 shows the general structure of the used DNN. Where $\{x_1, x_2, \ldots, x_n\}$ denotes the input layer, which in our study is the magnitude of EIS measurements for the frequency range of 20 mHz to 20 kHz at different temperatures and lifetime levels. The output of each neuron in the first and the next hidden layers is calculated by (4) and (5), respectively:

$$h_i^1 = f\left(b_1 + \sum_{i=1}^{n} W_i x_i\right) \quad \text{4-2}$$

$$h_i^{j+1} = f\left(b_{\mathrm{j}+1} + \sum_{i=1}^{m_j} w_i^j h_i^j\right) \quad \mathrm{j} \geq 1 \quad \text{4-3}$$

where in 4-2, f is the activation function, x_i is the i_{th} neuron in the input layer, W_i is the i_{th} neuron's weight in the input layer, b_1 denotes the deviation from the input layer to the first hidden layer, n is the number of input neurons. In 4-3, $b_{\mathrm{j}+1}$ denotes the deviation from the j_{th} hidden layer to the $j + 1_{th}$ hidden layer, m_j is the number of neurons in the j_{th} hidden layer, w_i^j is the weight of i_{th} neuron in the j_{th} hidden layer, and h_i^j is the output of i_{th} neuron in the j_{th} hidden layer. The final output, which in our study is the predicted capacity of the battery, can be calculated by the following formula:

$$y = f\left(b_{\mathrm{p}+1} + \sum_{i=1}^{m_p} w_i^p h_i^p\right) \quad \text{4-4}$$

where w_i^p is the weight of i_{th} neuron in the last hidden layer, h_i^p is the output of i_{th} neuron in the last hidden layer, p is the number of the hidden layers, and p_{th} layer is the last hidden layer. The

calculated output of the DNN model is compared to the real value from the dataset to calculate the loss function. An optimization algorithm is then utilized to minimize the loss function and tune the values for the weights and deviations. Table 4-1 indicates the configuration of the layers and activation function utilized in this study.

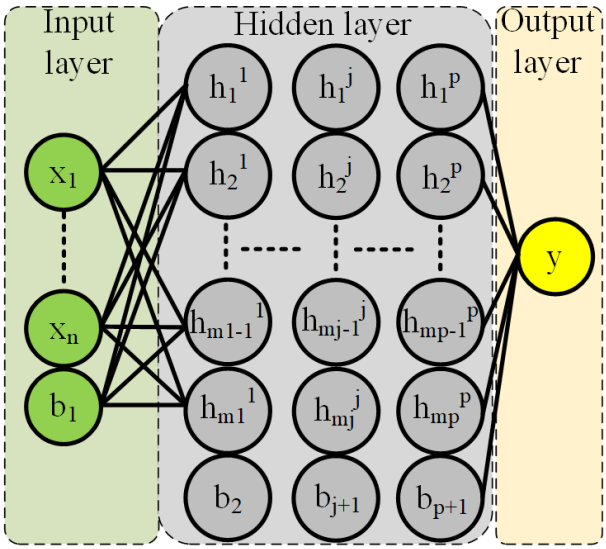

Figure 4-2. A general indication of the DNN model

Table 4-1. the configuration of the layers and activation function of the proposed DNN

Layers	Neurons	Activation function
Input layer	62	
First hidden layer	32	ReLU
Second hidden layer	16	ReLU
Third hidden layer	8	ReLU
Output layer	1	ReLU

4.3.2 Transfer learning

Typically, ML algorithms are presumed to be trained and tested by training and test datasets from the same distribution. However, this presumption may not be true in real-world applications.

When the test dataset alters, the ML algorithm should be retrained based on a substantial amount of newly produced training dataset, which is expensive and time-consuming, to maintain precision [134]. To prevent the malfunction of ML algorithms confronting a new test dataset distribution, TL has arisen. TL transfers the learned knowledge from the previous source dataset to ease the model building of the target source. In other words, a small amount of newly produced training data is sufficient to rebuild an ML algorithm, while the data may not necessarily be obtained from similar test data distribution [133]. TL technique will help us avoid time-consuming experimental tests for battery aging.

The main goal of this chapter is to employ the application of TL in conjunction with DNN for the capacity estimation of Li-ion batteries using EIS measurements as the input features. According to Figure 4-3, TL is achieved through the following two steps in this study: first, the base DNN model is trained and validated based on the source dataset, then the knowledge is transferred to rebuild (retrain and validate) a new model based on a specific portion of the target dataset and the rest of the dataset is utilized to test the rebuilt model. In other words, the TL fine-tuning strategy is adopted to adjust the parameters of one or more hidden layers using the target dataset, while the parameters of other layers remain unaltered, and the results for each case are compared. In this manner, the TL model is built. The resultant DNN model after TL is denoted as DNN-TL in the remainder of the paper. Simultaneously, the proposed DNN-TL model can transfer the lifetime data and the previously trained model of the source dataset to the newly built model of the target dataset for easier capacity prediction. Its significant learning capability can connect the rich information in the EIS measurements and model between two domains to facilitate the prediction model construction of the target dataset, thus mitigating the requirement of cycling data and improving the training efficiency.

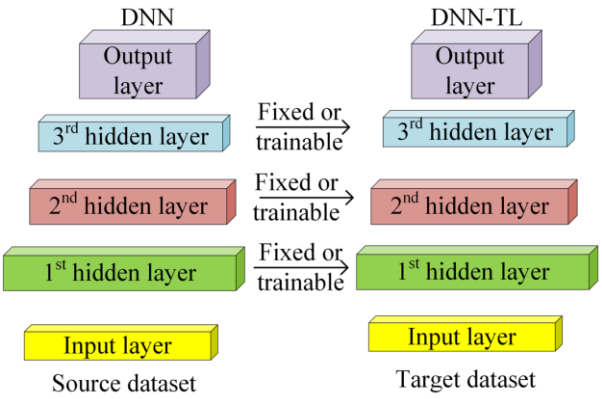

Figure 4-3. DNN-TL model construction

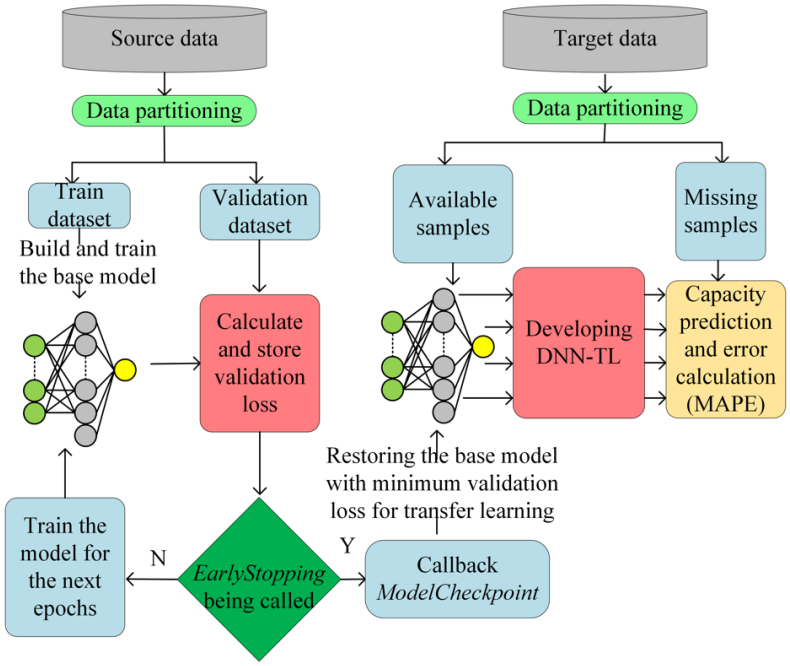

Figure 4-4. DNN-TL algorithm for capacity prediction

4.3.3 Implementation details

Figure 4-4 represents the general algorithm for capacity prediction of the battery using TL.

In this study, the source dataset, according to which the base DNN model is trained and validated, consists of the EIS measurements and capacity of the batteries 25C01–25C03, 25C05-25C07, and 35C01-35C02. The source dataset is divided into training and validation datasets, and the samples are selected randomly for each dataset. The ratio of training dataset to the validation

dataset is set to be 8:2. The prediction models were built by *Keras* upon *Tensorflow* backend in Python. The DNN model is trained for 4000 epochs; an epoch refers to one cycle through the entire training dataset. Typically, training a DNN takes more than a few epochs. In other words, DNN is fed on the training data for more than one epoch in different patterns for better generalization when given a new unobserved input (test data). However, on the one hand, overfitting may occur if the number of epochs is too large, and on the other hand, too few epochs may result in an underfit model. We used early stopping, which is a method that allows us to determine a randomly large number of training epochs and stop the model from being trained once the model performance halts to be improved on a holdout validation dataset. Therefore, a validation dataset is required during training the DNN model for using early stopping method. The loss function, which is validation loss (mean squared error (MSE)) to be optimized for the DNN model, is calculated at the end of each epoch. *EarlyStopping* is a method backed by *Keras* that stops the training early through a callback. This callback will observe the MSE improvement and trigger the training process once the improvement is stopped. However, the first sign of no further improvement may not be the best time to stop training because the model may coast into a plateau of no improvement or even get slightly worse before getting much better. To tackle this problem, a delay is added to the trigger in terms of the number of epochs on which there is no improvement in MSE. This can be done by setting the “patience" argument, which *Keras* also support. The *EarlyStopping* callback will stop training once called, but the model at the end of training may not be the model with the best performance on the validation dataset, i.e., minimum MSE. An additional callback needs to be triggered to store the best model observed with minimum validation loss during training for later use. The *ModelCheckpoint* is the callback function for this purpose.

Then, to transfer the knowledge from the base DNN to DNN-TL, the EIS measurements at 0%

and 100% SOCs of the batteries 45C01and 45C02 are employed as the target dataset. For the target datasets at each SOC, namely, 0% and 100%, two case studies are conducted in this paper to investigate the efficacy and comprehensiveness of the proposed DNN-TL model: i) the first 50% and ii) the first 20% of the target datasets are utilized for re-training and validation of the DNN-TL model based on the method explained in the previous paragraph. The remaining portion of the target dataset, which is considered missing data, is employed to predict the battery's capacity. Moreover, the effect of the number of fixed layers during the re-training of DNN-TL is studied. The versatility of DNN-TL can be demonstrated in this study such that only a small amount of EIS measurements and capacity of the battery at the temperature of 45 °C is obtained for some cycles through the experiments, and the rest can be predicted using TL. Eventually, the proposed DNN-TL model results are compared with the stand-alone DNN based on the target dataset.

4.3.4 Accuracy evaluation

The indices used for the evaluation of the performance of the proposed model are:

- MAPE

MAPE is used to compare the precision of the prediction and is defined as follows:

$$MAPE = \frac{100}{n}\sum_{i=1}^{n}\left|\frac{y_i - \hat{y}_i}{y_i}\right| \qquad 4\text{-}5$$

where y_i is the actual value of i_{th} sample, $\hat{y}_i$ is the estimated output of i_{th} sample, and n is the number of the samples. The smaller the MAPE, the better the prediction.

- MSE

Mean square error is an estimate of the standard deviation of the random component in the data and is utilized for optimizing the validation loss while training the models and is defined as

follows:

$$MSE = \frac{\sum_{i=1}^{n}(y_i - \hat{y}_i)^2}{n} \quad 4\text{-}6$$

where y_i is the actual value of i_{th} sample, $\hat{y}_i$ is the estimated output of i_{th} sample, and n is the number of the samples.

- Coefficient of determination

The coefficient of determination or R-squared is defined to demonstrate the goodness of the fit and how well the missing or unobserved samples can be predicted. The best possible value is 1, and the value can be negative too, which indicates that the model cannot follow the actual datasets. R-squared is defined as follows:

$$R_{squared} = 1 - \frac{\sum_{i=1}^{n}(y_i - \hat{y}_i)^2}{\sum_{i=1}^{n}(y_i - \bar{y})^2} \quad 4\text{-}7$$

where y_i is the actual value of i_{th} sample, $\hat{y}_i$ is the estimated output of i_{th} sample, $\bar{y}$ is the mean of the actual samples, and n is the number of the samples.

4.4 Results and Discussions

To verify the state of the art of the proposed capacity prediction method based on TL, we compared the performance of DNN-TL with no fixed-layer, 1 fixed-layer, 2 fixed-layer, and 3 fixed-layer models with the stand-alone DNN model, which is considered as the benchmark model, on different datasets, with the same ratio for training and testing. The difference between the DNN-TL models and the stand-alone DNN model is that the former is retrained and rebuilt by the training dataset from the target dataset, having their neurons' weights initialized based on the previously trained base model; however, for the latter, the neurons' weights are initialized during the model training.

4.4.1 Prediction results using target dataset at SOC 0%

In this scenario, the target dataset, i.e., EIS measurements at SOC 0% for the batteries 45C01 and 45CO2, is utilized for training, validation, and prediction.

- Using the first 50% of the target dataset for training

100% of the target dataset of the battery 45C01 and the first 50% of the target dataset of the battery 45C02 (from 0-250 cycles) with a ratio of 8:2 is employed for training and validating the DNN-TL and stand-alone DNN models. Fig. 6 depicts the predicted capacity against the true capacity value based on the validation dataset for DNN-TL with no fixed-layer, DNN-TL with 1fixed-layer, and the stand-alone DNN model. The reason that DNN-TL with 2 and 3 fixed-layer have not been shown in Figure 4-5 , is that these models did not demonstrate accurate performance toward the concept of TL. One may conclude that during the TL, the most important layers are the last two layers of the DNN-TL models, as they are responsible for transferring the knowledge and accurate prediction on the target dataset. Therefore, on account of preventing the last two layers of DNN-TL with 2 and 3 fixed-layer from being re-trained, these models could not demonstrate satisfying performance on capacity prediction for an unseen dataset. Figure 4-6 indicates the performance of DNN-TL with no fixed-layer and 1 fixed-layer compared to the stand-alone DNN model. It is evident from this figure that the DNN-TL model outclasses the stand-alone DNN model. Table 4-2 indicates the MAPE values for predicting the capacity of the battery 45C02 after 250 cycles, i.e., the second 50% of the target dataset of the battery 45C02, which is considered as missing data. The MAPE for DNN-TL with no fixed-layer, 1 fixed-layer, 2 fixed-layer, 3 fixed-layer, and the stand-alone DNN model is 0.605%, 0.495%, 0.663%, 8.238%, and 2.773%, respectively, which indicates that DNN-TL outclasses the stand-alone DNN model. The evaluation indices of Table 4-2 prove the above-mentioned conclusion about the DNN-TL with 2 and 3 fixed-

layer, as these values are relatively high for these two models. The R-squared from Table 4-2 for the DNN-TL with no fixed-layer, 1 fixed-layer, 2 fixed-layer, 3 fixed-layer, and the stand-alone DNN model is 0.9551, 0.9668, 0.9026, -4.420, and 0.2092, respectively. The closer the R-squared value is to 1, the better the model can follow and fit the unobserved or actual missing dataset. The negative value of the R-squared indicates that the model cannot fit the actual missing dataset. Given this, the DNN-TL with no fixed-layer and 1 fixed-layer has the best R-squared. The negative value of the R-squared for DNN-TL with 3 fixed-layer indicates the model is not working correctly and cannot follow the actual missing data. The low R-squared value of the stand-alone DNN model indicates its incapability to fit the actual unobserved dataset.

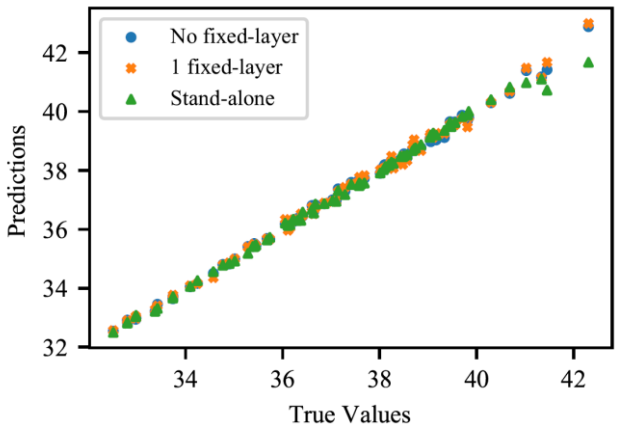

Figure 4-5. Prediction results vs. true values of capacity (mAh) for validation dataset at SOC 0% when the first 50% of target dataset is utilized for training and validation

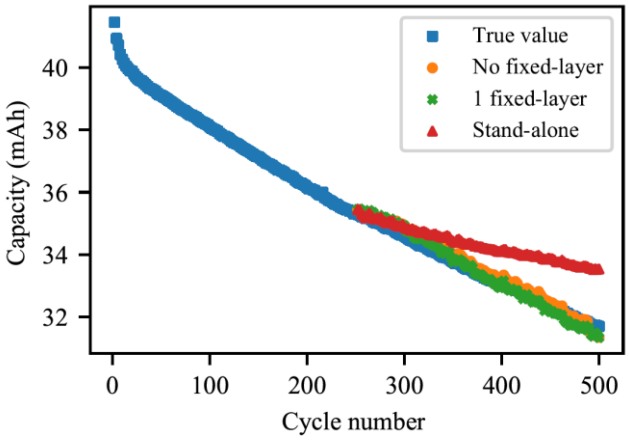

Figure 4-6. Capacity prediction for the battery 45C02 at SOC 0% when the second 50% of the target dataset is considered as missing data

- Using the first 20% of the target dataset for training

This case study follows the same steps as the previous one with the difference that only the first 20% of the target dataset of the battery 45C02 (from 0-100 cycles) with the ratio of 8:2 is employed for training and validating the DNN-TL and stand-alone DNN models. Figure 4-7 depicts the predicted capacity against the true capacity value based on the validation dataset for DNN-TL with no fixed-layer, DNN-TL model with 1fixed-layer, and the stand-alone DNN model. For the same reason, DNN-TL with 2 and 3 fixed-layer have not been shown in Figure 4-7. Figure 4-8 indicates the performance of DNN-TL with no fixed-layer and 1 fixed-layer compared to the stand-alone DNN model. It is evident from this figure that the DNN-TL model outperforms the stand-alone DNN model. Another remarkable point is that only the first 20% of the target dataset has been exploited for re-training and validating the model, and the remaining, which is a missing dataset, can be predicted by the DNN-TL model. Table 4-2 indicates the MAPE values for predicting the capacity of the battery 45C02 after 100 cycles, i.e., the second 80% of the target dataset of the battery 45C02, which is considered as missing data. The MAPE for DNN-TL with no fixed-layer, 1 fixed-layer, 2 fixed-layer, 3 fixed-layer, and the stand-alone DNN model is 0.999%, 2.703%, 2.168%, 12.114%, and 4.262%, respectively, which indicates that DNN-TL outclasses the stand-alone DNN model. Table 4-2 also demonstrates the robustness of the DNN-TL model with no fixed-layer, as for the different sizes of the target dataset, the model exhibits accurate performance. The R-squared from Table II for the DNN-TL with no fixed-layer, 1 fixed-layer, 2 fixed-layer, 3 fixed-layer, and the stand-alone DNN model is 0.9526, 0.7006, 0.7821, -7.865, and 0.008, respectively, which indicates that DNN-TL with no fixed-layer has the best R-squared.

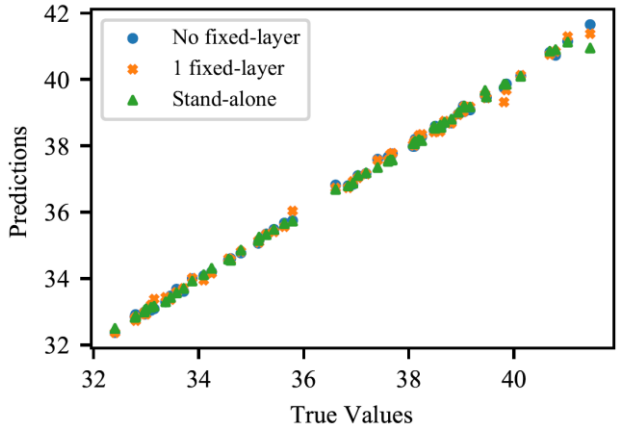

Figure 4-7. Prediction results vs. true values of capacity (mAh) for validation dataset at SOC 0% when the first 20% of target dataset is utilized for training and validation

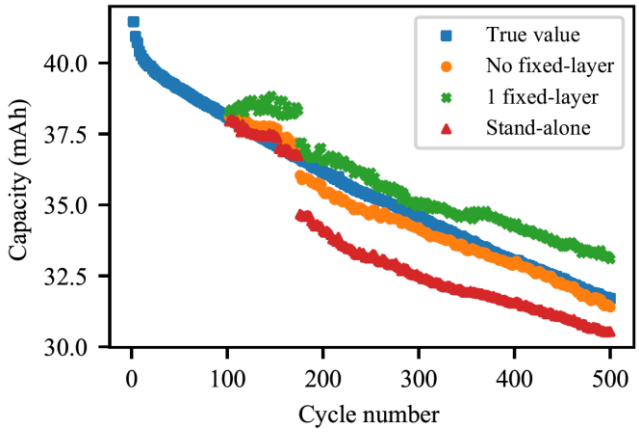

Figure 4-8. Capacity prediction for the battery 45C02 at SOC 0% when the second 80% of the target dataset is considered as missing data

Table 4-2. MAPE (%) and R-squared values for DNN-TL and DNN on (1) first 50% of, (2) first 20% of target dataset at SOC 0%

MAPE (%)	DNN-TL				DNN
	No Fixed-layer	1 Fixed-layer	2 Fixed-layer	3 Fixed-layer	
(1)	0.605	0.495	0.663	8.238	2.773
(2)	0.999	2.703	2.168	12.114	4.262
R-squared					
(1)	0.9551	0.9668	0.9026	-7.865	0.008
(2)	0.9526	0.7006	0.7821	-4.420	0.2092

4.4.2 Prediction results using target dataset at SOC 100%

In this scenario, the target dataset, i.e., EIS measurements at SOC 100% for the batteries 45C01

and 45CO2, is utilized for training, validation, and prediction.

- Using the first 50% of the target dataset for training

Following the same steps as the previous scenario, Figure 4-9 demonstrates the performance of the models based on the validation dataset. Figure 4-10 indicates the performance of DNN-TL with no fixed-layer and 1 fixed-layer compared with the stand-alone DNN model. It is evident from this figure that DNN-TL with no fixed-layer model outclasses the other two models. Table 4-3 indicates the MAPE values for predicting the capacity of the battery 45C02 after 250 cycles, i.e., 50% of the target dataset of the battery 45C02, which is considered as missing data. The MAPE for DNN-TL with no fixed-layer, 1 fixed-layer, 2 fixed-layer, 3 fixed-layer, and the stand-alone DNN model is 0.362%, 6.517%, 9.185%, 11.020%, and 2.24%, respectively, which indicates that DNN-TL outclasses the stand-alone DNN model. The R-squared from Table 4-3 for the DNN-TL with no fixed-layer, 1 fixed-layer, 2 fixed-layer, 3 fixed-layer, and the stand-alone DNN model is 0.9808, -4.0876, -7.4699, -11.321, and 0.3567, respectively, which indicates that DNN-TL with no fixed-layer has the best R-squared. The rest of the models cannot follow the actual missing dataset at this condition.

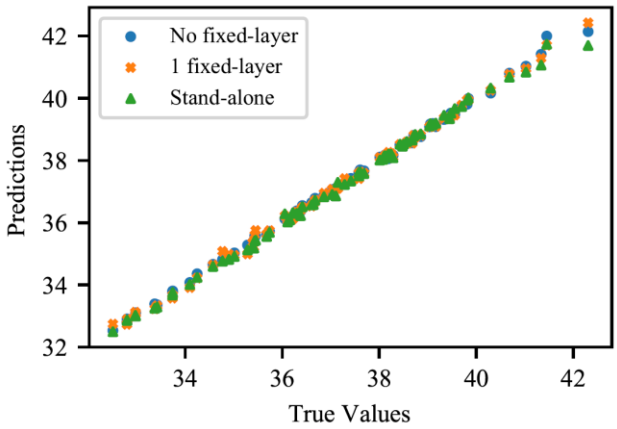

Figure 4-9. Prediction results vs. true values of capacity (mAh) for validation dataset at SOC 100% when the first 50% of target dataset is utilized for training and validation

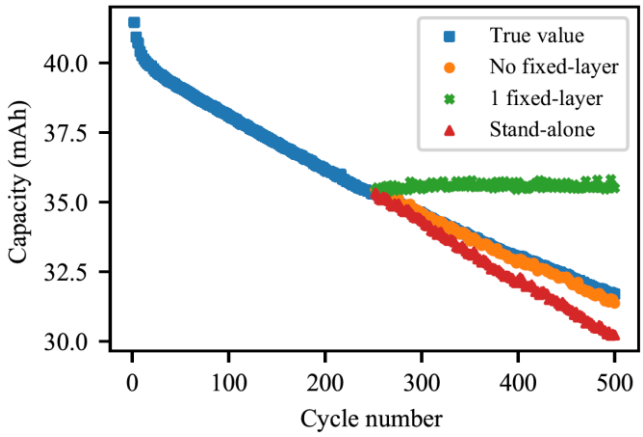

Figure 4-10. Capacity prediction for the battery 45C02 at SOC 100% when the second 50% of the target dataset is considered as missing data

- Using the first 20% of the target dataset for training

In this case study, the same analysis is conducted. The performance of the models on the validation dataset has been shown in Figure 4-11. Figure 4-12 manifests the estimation characteristics of DNN-TL with no and 1 fixed-layer and that of the stand-alone DNN model. Figure 4-12 indicates that DNN-TL with no fixed-layer performed best in these conditions among the other models. The evaluation indices have been recorded in Table 4-3. The MAPE for DNN-TL with no fixed-layer, 1 fixed-layer, 2 fixed-layer, 3 fixed-layer, and the stand-alone DNN model is 0.501%, 5.684%, 8.913%, 12.366%, and 1.025%, respectively, which indicates that the same conclusion can be made as the previous case study. The R-squared from Table 4-3 for the DNN-TL with no fixed-layer, 1 fixed-layer, 2 fixed-layer, 3 fixed-layer, and the stand-alone DNN model is 0.9850, -0.3255, -2.018, -4.554, and 0.9309, respectively, which indicates that DNN-TL with no fixed-layer and the stand-alone DNN model have the best R-squared. The rest of the models cannot follow the actual missing dataset at this condition.

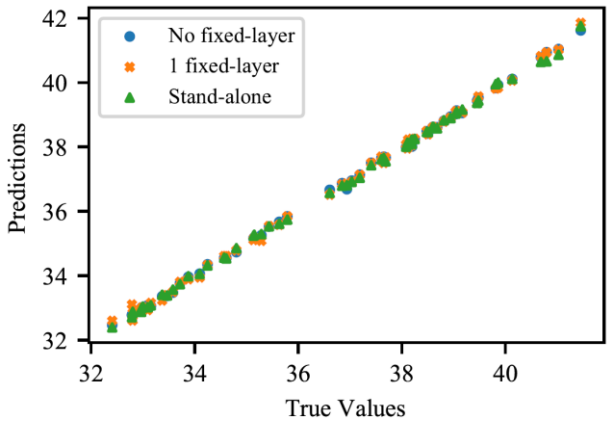

Figure 4-11. Prediction results vs. true values of capacity (mAh) for validation dataset at SOC 100% when the first 20% of target dataset is utilized for training and validation

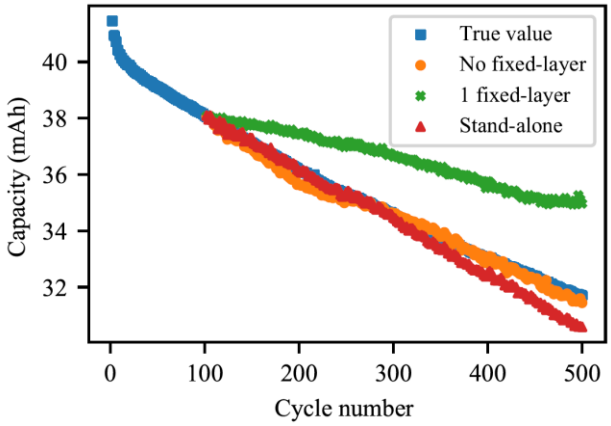

Figure 4-12. Capacity prediction for the battery 45C02 at SOC 100% when the second 80% of the target dataset is considered as missing data

Table 4-3. MAPE (%) and R-squared values for DNN-TL and DNN on (1) first 50% of, (2) first 20% of target dataset at SOC 100%

	DNN-TL				DNN
MAPE(%)	No Fixed-layer	1 Fixed-layer	2 Fixed-layer	3 Fixed-layer	
(1)	0.362	6.517	9.185	11.020	2.24
(2)	0.501	5.684	8.913	12.336	1.025
R-squared					
(1)	0.9808	-4.0876	-7.4699	-11.321	0.3567
(2)	0.9850	-0.3255	-2.018	-4.554	0.9309

Figure 4-13 indicates the histogram error bar for all the above scenarios. It is evident that for the DNN-TL with no fixed-layer, the number of predicted samples with the error of less than 1%

is significantly higher than the other models, especially the stand-alone DNN model. In contrary to the other models, the histogram plot of the DNN-TL with no-fixed layer almost follows the same pattern in all the scenarios, which indicates its well performance at different conditions.

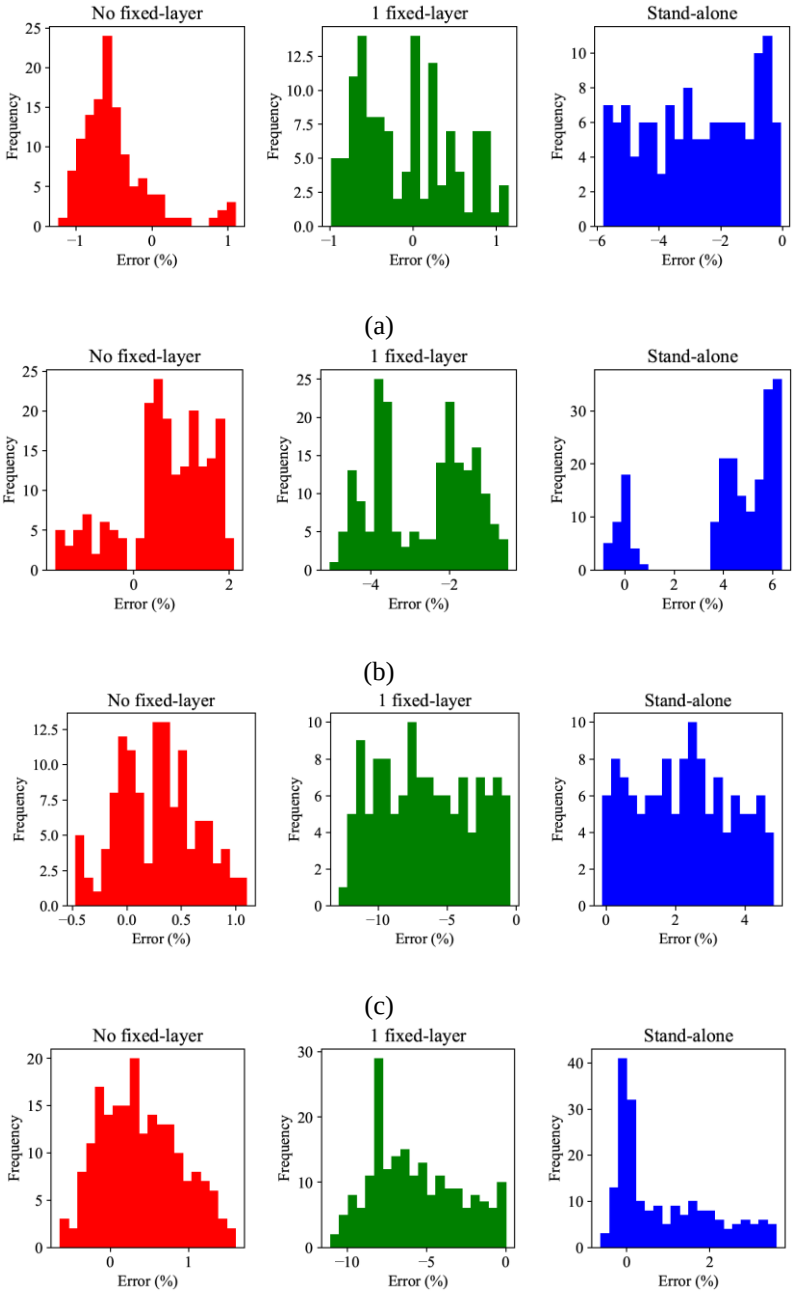

Figure 4-13. Capacity prediction for the battery 45C02 (a) at SOC 0% when the second 50% of the target dataset is considered as missing data, (b) at SOC 0% when the second 80% of the target dataset is considered as missing data, (c) at SOC 100% when the second 50% of the target dataset is considered as missing data, (d) at SOC 100% when the second 80% of the target dataset is considered as missing data.

The effect of the number of fixed layers in the DNN-TL model was demonstrated, and DNN-TL with no fixed-layer proved an outstanding performance compared to the other models, specifically the stand-alone DNN model. This proves that every single layer in DNN-TL carries the knowledge to transfer and accounts for better estimation of capacity for an utterly unobserved dataset with different distributions. The stand-alone DNN model achieves an acceptable accuracy with an average MAPE of 2.575%. The proposed DNN-TL model with no fixed-layer outclasses the other DNN-TL models and the benchmark model, i.e., the stand-alone DNN model, with the average MAPE of 0.616% for the same scenarios. The average R-squared of 0.9683 was achieved by the DNN-TL with no fixed-layer, which indicates the goodness of its fit and its capability to follow the actual missing datasets. Although the stand-alone DNN model has an acceptable MAPE, it demonstrates a poor R-squared, which means that it cannot follow the actual missing dataset.

The two different scenarios with two various target datasets for EIS measurements at SOC 0% and 100% were tested to demonstrate the effectiveness of direct usage of EIS measurements instead of using it as equivalent circuit modeling and how rich they are in conveying the information about the health status of batteries at different SOCs. One may question the comprehensiveness of the proposed model as the other SOC values have not been tested. The data for other SOC values were not available to be included in our datasets; however, interpolation cannot be denied in neural network models. It is evident from Fig. 2 that EIS measurements follow a predictable pattern in accordance with temperature and aging. A predictable pattern of EIS measurement based on the mentioned parameters further enhances the ability of the model to interpolate between other values of SOC. EIS characteristic is also dependent on the SOC and follows a similar pattern. The results confirm the performance of the models based on the validation dataset.

4.5 Conclusions

A novel battery capacity prediction method using TL with DNN was proposed. This study employed EIS measurements directly, which is not dependent on the charging/discharging process and IC curves, for three ambient temperatures of 25 °C, 35 °C, and 45 °C. The effect of the number of fixed layers during retraining of the DNN-TL was also investigated, and the results of capacity prediction on the target dataset were compared between DNN-TL models that are DNN-TL with different numbers of fixed layers and the stand-alone DNN model, which was used as the benchmark model. The maximum MAPE, when the first 50% and 20% of the target dataset were used for retraining the DNN-TL with no fixed-layer, were found to be 0.605% and 0.999%, respectively. As the results of the chapter indicate, an average MAPE of 0.616% was achieved for the DNN-TL with no fixed-layer in four different scenarios with different sizes of the target dataset, while the stand-alone DNN model achieved an average MAPE of 2.575%. The average R-squared of 0.9683 was achieved by the DNN-TL with no fixed-layer, which indicates the goodness of its fit and its capability to follow the actual missing datasets.

Chapter 5

Co-estimation of SOC and SOH

5.1 Introduction

Despite numerous literatures on estimating SOC and SOH separately, it is known that with the degradation of the batteries, the increase in battery resistance and the decrease in its capacity will lead to a dramatic SOC deviation [141]. Therefore, in order to achieve a qualified SOC estimation method, it should account for health status of the battery. In other words, the SOH should be used as an input to SOC estimation method for joint estimation, and in such case higher estimation accuracy can be achieved. To enhance the performance of SOC estimation method, considerable studies have been tailored toward the joint estimation of SOC and SOH. There are myriads of works leveraging ECM and EIM for joint estimation of SOC and SOH [142], [143], [144], [145], [146], and [147]. In [148], a fractional-order model is adopted to joint estimate the SOC and SOH of the battery. In this approach, the parameters of the model are optimized using a hybrid GA/PSO technique. The validity of the proposed method is verified on the Dynamic Stress Test and Federal Urbane Driving Schedule datasets. A dual fractional-order EKF is integrated into the model for co-estimation. In [85], a second-order equivalent circuit model considering the temperature effect is implemented to model the electrical performance. The particle swarm optimization (PSO) is then utilized to instantly update the parameters of the battery model. The charging duration is chosen as the input feature. The SOH is estimated by the LSTM method, and then the estimated

value is used in a second-order ECM with the square root cubature Kalman filter to estimate the SOC. In [149], an ECM is exploited to model the battery behavior with recursive least squares, which identifies the model parameters. A minimalist EIM is proposed to evaluate the SOH. The capacity degradation is measured by identifying the amount of lithium inventory loss in the battery. Based on the capacity value the SOC of the battery is then estimated. The data used in the mentioned study are for the batteries which have undergone random walk (RW) tests. So, the dataset does not simulate the real-world driving cycle scenarios. In [150], a battery SOH and SOC co-estimation algorithm is proposed based on the first-order ECM. First, the recursive least square method and AEKF are employed to jointly achieve online model parameters identification and SOC estimation. Partial voltage curves during the charging/discharging process are employed to estimate the battery age. The Elman neural network is then employed to estimate battery SOH in real-time, which provides the foundation for battery SOC estimation. Although these model-based methods achieve high accuracy for co-estimation of battery states, they rely on the complicated testing procedure, and constructing an accurate battery model is a daunting task requiring an enormous amount of knowledge about the battery physics and chemical reactions [151].

Compared to the model-based methods, data-driven methods extract a relationship between the inputs and outputs from the dataset. In such a case, no information is required about the chemistry of the battery, its physical interoperation, and testing procedures. Because of the potential pros of data-driven modes, such as flexibility and nonlinear mapping, different ML models, e.g., ANN [152] and SVM [153]. In [151], the battery is degraded using a dynamic stress test, and SOH is estimated using measurable terminal voltage and current by LS-SVM. The current SOH along with the other two measurements, are then employed in unscented PF for SOC estimation. The direct mapping of input features and output eliminate parameter identification and updating, which are

highly time-consuming. In [154], a multilayer NN model is used to estimate the SOH. The estimated SOH at three conditions is then utilized to estimate the SOC of the battery. The voltage during the discharge process at each cycle is measured and utilized as input features for SOH estimation. The battery data were collected based on CC-CV charging/discharging process, which does not accurately mimic the behavior of the battery under real-world conditions. In [155], a dynamic RNN with the ability of dynamic updating is constituted on the basis of nonlinear autoregressive with exogenous input architecture. A self-adaptive weight PSO algorithm is then utilized for training the network. The SOC and SOH are then jointly estimated under various conditions, including temperature, current, and degree of aging, to evaluate the robustness and accuracy of the model. Although different operating conditions have been considered, the corresponding dataset is obtained in CC-CV charging/discharging procedures, which does not qualify the dataset for real-world driving cycles simulations. In [156], the charging time of segment voltage is introduced as an input feature. LS-SVM is then utilized to estimate the SOH of the battery. The estimated SOH along with other features such current and voltage are utilized in nonlinear autoregressive with exogenous algorithm to estimate the SOC of the battery. In [157], a unified data-driven method, namely, LSTM-RNN is utilized to co-estimate the SOH and SOC of the battery. The SOH dataset has been obtained from CC-CV charging/discharging process. Although the same charging process is conducted for SOC dataset, the discharge procedure only consists of different CC with periodic transformation until cutoff voltage is reached.

To this end, the discussed literatures have employed various input features, among which some of them rely on the charging/discharging process, such as the charging time of segmented voltage. In contrast, insufficient attention has been dedicated to the EIS measurements as one of the most informative datasets for the same purpose. Although there are some studies employing EIM using

EIS for co-estimation of SOC and SOH [158], [146], there are very few works employing EIS measurements directly as input features for SOH estimation only [8], [159]. In this chapter, a novel method is proposed for the joint estimation of SOC and SOH. First, the EIS measurements are adopted directly as input features in two ML algorithms, i.e., GPR and DNN, to estimate the SOH of the battery (Two algorithms for the sake of comparison). The estimated SOH values in conjunction with the real-time measurable battery's voltage and current are then fed to two other ML algorithms, i.e., LSTM and DNN, to estimate the SOC of the battery. In such a manner, the aging effect of the battery is considered for SOC estimation of the battery. The contributions of our research are multiple-fold: (1) In contrary to the reviewed studies that employ the datasets obtained from simple CC-CV or random walk charging/discharging processes, The SOH and SOC datasets of this study are provided from real-world driving cycles which results in more practical and realistic use of the proposed method for joint estimation of SOC and SOH. (2) Compared to the other studies that utilize EIS measurements at some specific frequencies, the EIS measurements are obtained for a wide range of frequencies, i.e., 1 mHz-10 kHz. (3) The SOH is estimated using EIS measurements obtained at three SOC levels, i.e., 20%, 50%, and 80%. The estimated values are then utilized with the voltage and current of the battery to estimate the SOC of the battery under operation. This implies the robustness of the model to joint estimate the SOH and SOC using EIS obtained at any given SOC.

5.2 EIS Experimental Data

The experimental datasets from [160] are utilized in our study. The dataset is composed of EV standard driving cycle profiles and diagnostic tests, i.e., capacity and EIS tests, for ten INR21700-M50T NMC cells over a period of 23 months. It is worth mentioning that in our study, we use six out of the ten cells, namely, V4, V5, W5, W8, W9, and W10. The cell specifications have been

recorded in Table 5-1. To regenerate the degradation exposed to the lithium-ion cells during real-world EV operation, the charging/discharging profiles shown in Figure 5-1 were used. This figure shows an entire cycle which will be explained thoroughly below. In this dataset, a cycle is composed by the sequence of 6 steps, summarized in Table 5-2. A cycle starts with a CC charge performed at a C-rate (1C-rate indicates that the 1A discharge current will discharge the entire battery in 1 hour) of C/4, C/2, 1C, or 3C, as specified in the second column of Table 5-3 (Step 1). Once the battery voltage reaches 4V, a CV phase starts (Step 2) until the current goes below 50mA. Next, Step 3 (CC at C/4) and Step 4 (CV) are designed to bring the battery to 4.2 V, corresponding to 100% SOC. Step 5 is used to discharge the battery from 100% to 80% SOC at C/4 constant current. In Step 6, a concatenation of Urbane Dynamometer Driving Schedule (UDDS) cycles is used to discharge the battery from 80% to 20% SOC. The diagnostic tests, i.e., capacity and EIS tests, are run after some number of cycles (for the majority of the cells, every 25 cycles, see Table 5-3). Capacity test, performed at C/20 discharge from a fully charge cell, is used to evaluate the cell discharged capacity or its SOH. EIS is performed to assess the battery impedance between 1mHz and 10kHz at 20%, 50%, and 80% SOC.

Table 5-1. Technical specifications INR21700-M50T NMC cell

Model	INR21700-M50T
Positive electrode	LiNiMnCoO2
Negative electrode	graphite and silicon
Nominal capacity	4.85Ah
Nominal voltage	3.63V
Charge cutoff voltage	4.2V
Discharge cutoff voltage	2.5V
Cutoff current	50mA

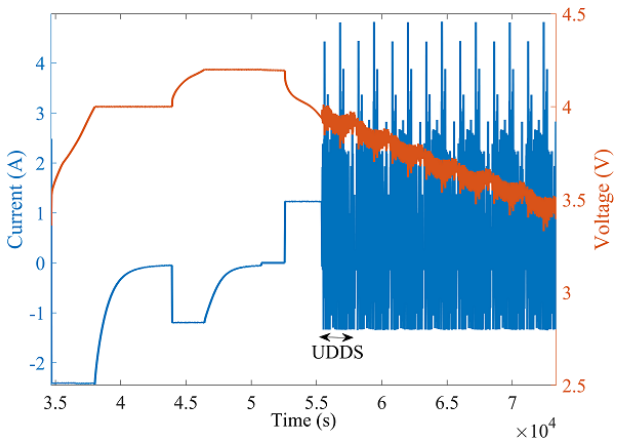

Figure 5-1. The charging/discharging cycle experienced by the cells

Table 5-2. Description of the experimental Cycle

Step	Action	Termination condition
1	CC charge at C-rate specified in the second column of Table III	4V is reached
2	CV charge	Current below 50mA
3	CC charge at C/4	4.2V is reached
4	CV charge followed by 30-minute rest	Current below 50mA
5	CC discharge at C/4	Reaching SOC 80%
6	UDDS discharge	Reaching SOC 20%

Table 5-3. Cells label, test charging condition, and diagnostic test number, all cells are tested at 23 ◦C.

		Diagnostic tests (capacity and EIS tests) [cycle]								
Cell	Charge	#1	#2	#3	#4	#5	#6	#7	#8	#9
W5	C/2	0	25	75	125	159	167	187	194	219
W8	C/4	0	25	75	125	148	150	151	157	185
W9	1C	0	25	75	122	144	145	146	150	179
W10	3C	0	25	75	122	146	148	151	159	188
V4	C/4	0	20	45	70	95	-	-	-	-
V5	1C	0	12	18	29	-	-	-	-	-

Figure 5-2 shows the SOH of the cells versus their cycling number. It is evident from Figure 5-3 3 that as the battery degrades, the EIS measurements increase; moreover, it can be observed that at any given cycle (at any SOH level), EIS measurements are different from each other at different SOC levels. This proves that EIS measurements at different SOC levels and lifetime levels provides informative data about the battery's status and can be considered a potential criterion for the SOH estimation of batteries during their longevity.

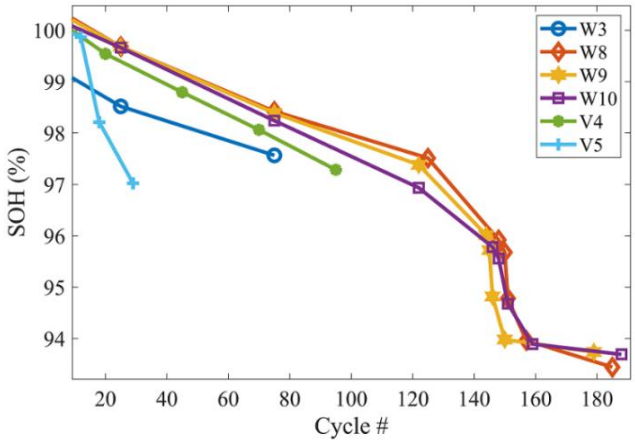

Figure 5-2. Aging of the cells

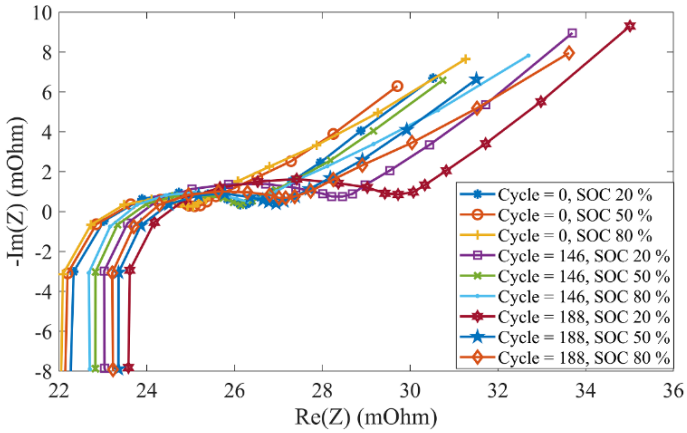

Figure 5-3. EIS measurements for cell W10 at different SOC and SOH levels

5.3 Methodology

For the sake of comparison, two ML models, i.e., GPR and DNN are leveraged in our study to estimate the SOH of the battery using EIS measurements conducted at three SOC levels, directly as input features. The effectiveness EIS measurements and the performance the mentioned ML models for SOH estimation investigated.

5.3.1 DNN and GPR structure for SOH estimation

- DNN structure

The DNN architecture has been discussed in section 4.3. However, in the current section, the

EIS measurements for the frequency range of 1 mHz to 10 kHz at different SOC and lifetime levels is the input layer, and the SOH is the output. Table 5-4 indicates the configuration of the layers and activation function utilized in this model.

- GPR structure

The GPR architecture has been discussed in section 3.3. However, in the current section, $x_i = [EIS\ measurments]$ and y_i is the SOH of the battery are the input and output, respectively.

Table 5-4. The Configuration of the layers and Activation function of the DNN for SOH estimation

Layers	**Neurons**	**Activation function**
Input layer	41	
First hidden layer	16	ReLU
Second hidden layer	8	ReLU
Third hidden layer	4	ReLU
Fourth hidden layer	4	ReLU
Output layer	1	ReLU

5.3.2 DNN and LSTM for SOC estimation

Similar to the SOH estimation methodology, two ML algorithms are adopted to perform the joint estimation of SOC. The performance of these models is compared when estimating the SOC through the cell's lifetime as the cell is aging using standard driving cycles (to simulate the real-world driving cycles).

- DNN structure

The structure of the DNN utilized for the SOC estimation is analogous to what was discussed in the previous part. However, in this model, the input features are the estimated SOH and the voltage and current from the UDDS driving cycle, and the output is the SOC of the battery. Table 5-5 indicates the configuration of the layers and activation function utilized in this model.

Table 5-5. The Configuration of the layers and Activation function of the DNN and LSTM for SOC estimation

LSTM		
Layer	**Neurons**	**Activation function**
Input layer	3	
First hidden layer	32	
Output layer	1	ReLU
DNN		
Layer	**Neurons**	**Activation function**
Input layer	3	
First hidden layer	64	ReLU
Second hidden layer	32	ReLU
Third hidden layer	16	ReLU
Output layer	1	ReLU

- Multilayer LSTM structure

In order to explain the LSTM structure, first, a brief introduction to RNN is required.

There are some forms of ML problems in which the order of input features to the model is of importance for predicting the output [161]. Time series predictions are classified as one of sequential problems.

According to Figure 5-4, the raw input data can be split into time step for a multilayer RNN, where $x^{<t>}$ is the input, $a^{<t>}$ is the hidden state passing through different cells at each time step, $y^{<t>}$ is the output for every t, and T_x is the input and output length. RNN considers the data at every time step in the sequence that it appears. This corresponding output passes from layer to layer is called hidden state. Essentially, the hidden state allows the RNN model to keep a memory of the corresponding states from the sequential data [162].

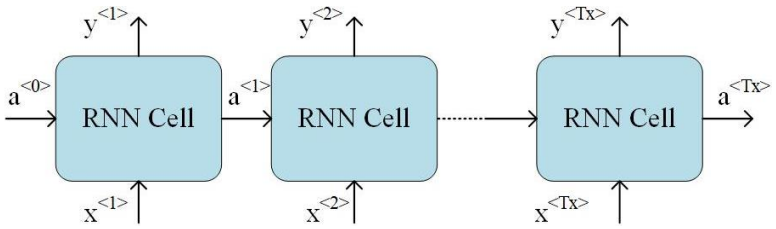

Figure 5-4. General structure of RNN

Figure 5-5 shows the structure of a single cell in the RNN model. RNN begins with the constitution of a single cell and then broadcasts to the number of time steps [163]. In this figure, $\tilde{y}^{<t>}$ is the predicted output, $a^{<t>}$ is the hidden state, $x^{<t>}$ is the input, and $a^{<t-1>}$ is the hidden state from previous cell. The current hidden state can be determined through Eq. 5-1 using *tanh* activation function. C_{aa} and C_{ax} are the hidden state and input parameters with a random value, respectively. b_a is the hidden state bias with the initial value of zero. Also $a^{<0>}$ can be set to zero. $\tilde{y}^{<t>}$ is calculated by Eq. 5-2, where C_{ay} and b_y are output parameter and bias, respectively. The initial output bias can be set to zero.

$$a^{<t>} = \tanh(C_{aa}a^{<t-1>} + C_{ax}x^{<t>} + b_a) \quad 5\text{-}1$$

$$\tilde{y}^{<t>} = \mathrm{ReLU}(C_{ay}a^{<t>} + b_y) \quad 5\text{-}2$$

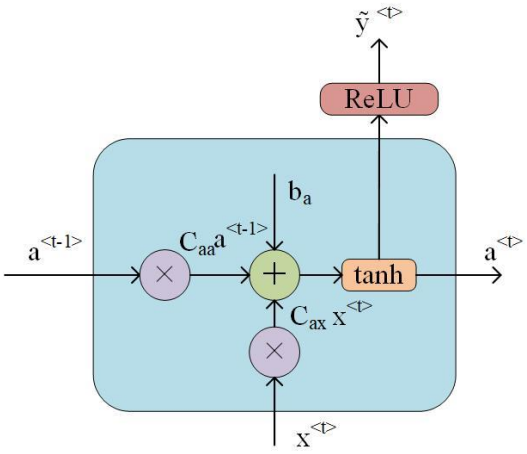

Figure 5-5. A single cell structure in RNN model

One of the deficiencies of the RNN models is that they do not work well with long-term dependencies because of the vanishing gradient problem during the training state. The problem stems from training the deep neural networks using gradient-based methods such as backpropagation [164]. The loss will decrease when it is propagated backward. Consequently, the loss decreases so much when it reaches the first few layers. Hence, it is almost impossible for the weights of the first few layers to be improved as a slight loss is propagated backward [164], [165]. The disappearing gradient problem means that RNNs will have poor performance in using long-term memory. In other words, the RNN models tend to remember everything, which leads to the failure to learn from long sequences [166]. In order to tackle this problem LSTM network has been proposed.

LSTM selectively forgets unnecessary inputs, and this allows it to deal with both short-term and long-term memories [167], [168]. A multilayer LSTM is leveraged in our study for SOC prediction. Figure 5-6 exhibits a general structure of a multilayer LSTM model.

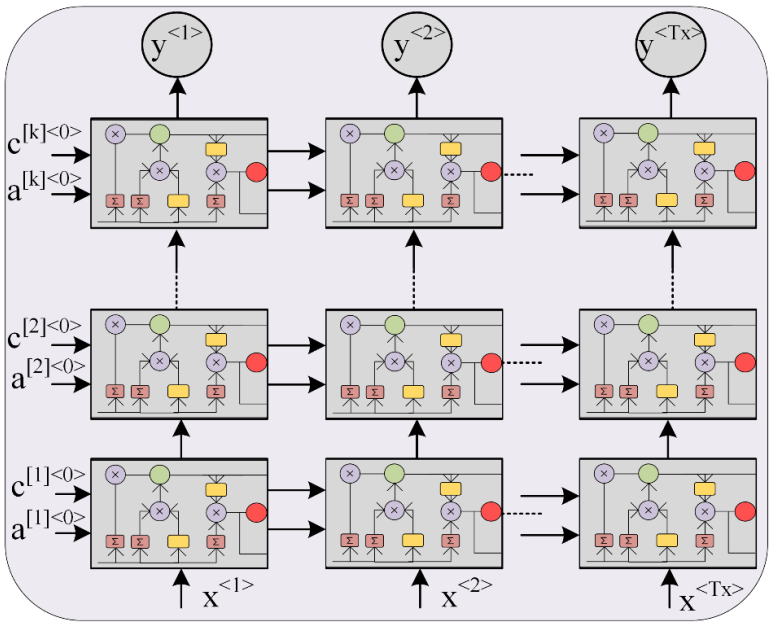

Figure 5-6. General structure of multilayer LSTM used in this study

Figure 5-7 indicates the structure of an LSTM cell containing four main gates, namely, Forget gate, Update gate, Input gate, and Output gate, to process the input data and estimate the desired output. According to this figure, the inputs of the LSTM-RNN model are fed to the model as a time series data:

$$\{(a^{<t-v-1>}, x^{<t-v>}), \dots, (a^{<t-2>}, x^{<t-1>}), (a^{<t-1>}, x^{<t>})\}$$

where v is the length of a time series, $a^{<t-1>}$ is the out state of hidden layer at step $t-1$, and $x^{<t>}$is the input vector at time t. For SOC estimation, t and $x^{<t>}$ represent second and the input vector at time t, i.e., $x^{<t>} = [\mathrm{SOH}, \mathrm{V}, \mathrm{I}]$. Moreover, there is another variable, $C^{<t>}$ which acts as the memory of the cell. It is responsible for passing the information, that must remain at the moment, from one structure to the next one. The function of each gate is explained below [169], [170]:

Forget gate ($\Gamma_f^{<t>}$): the proportion of the information to be disregarded from the memory cell is determined by this gate. A sigmoid activation function is adopted in this gate. It receives the inputs of $x^{<t>}$and $a^{<t-1>}$and generates a number between 0 and 1, which will be multiplied by $C^{<t-1>}$. If the value is close to zero, the gate prevents the information from passing to the next level. In other words, it forgets the information in the component of $C^{<t-1>}$. If the value is one, the information will pass. The output of forget gate is calculated as follows:

$$\Gamma_f^{<t>} = \sigma\left(W_f x^{<t>} + U_f a^{<t-1>} + b_f\right) \qquad 5\text{-}3$$

where W_f, U_f, and b_f are the two weights matrices and bias vector to determine the output of forget gate.

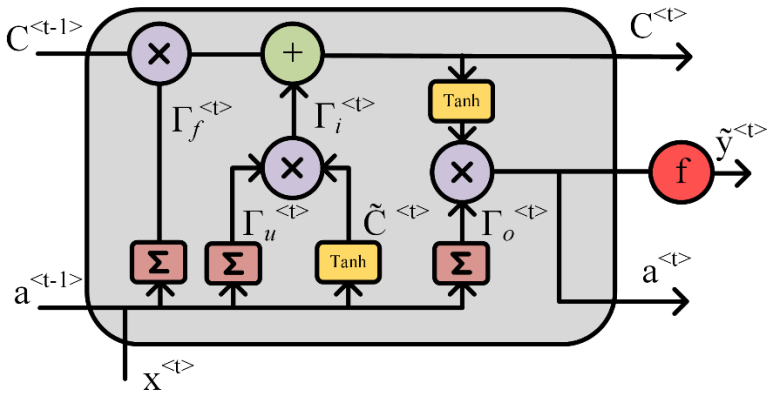

Figure 5-7. Structure of an LSTM cell

Update gate ($\Gamma_u^{<t>}$) and Input gate $\Gamma_i^{<t>}$: in order to update the cell state $C^{<t>}$, update gate and input gate are utilized. The input gate will decide how much information should pass to the current cell state, $C^{<t>}$. In such a case, first the update gate passes the $x^{<t>}$and $a^{<t-1>}$ to a sigmoid function, and the corresponding result is then multiplied by the output of a *tanh* function, i.e., $\tilde{C}^{<t>}$, which results in $\Gamma_i^{<t>}$as follows:

$$\Gamma_u^{<t>} = \sigma(W_u x^{<t>} + U_u a^{<t-1>} + b_u) \quad 5\text{-}4$$

$$\tilde{C}^{<t>} = tanh(W_C x^{<t>} + U_C a^{<t-1>} + b_C) \quad 5\text{-}5$$

$$\Gamma_i^{<t>} = \Gamma_u^{<t>} . \tilde{C}^{<t>} \quad 5\text{-}6$$

where W_u, U_u, W_C, and U_C are the two weight matrices for the update gate and $\tilde{C}^{<t>}$ gate, respectively. b_u and b_C are the bias vector for the Update gate and $\tilde{C}^{<t>}$ gate, respectively. Ultimately, the current cell state is provided by the following formula:

$$C^{<t>} = \Gamma_f^{<t>} . C^{<t-1>} + \Gamma_i^{<t>} \quad 5\text{-}7$$

Output gate: the amount of information to be retrained in the hidden state is determined by this gate. The output result of the gate is calculated below:

$$\Gamma_o^{<t>} = \sigma(W_o x^{<t>} + U_o a^{<t-1>} + b_o) \quad 5\text{-}8$$

where W_o, U_o, and b_o are the two weights matrices and bias vector to determine the output of output gate. The current hidden state $a^{<t>}$ is formulated as below:

$$a^{<t>} = \Gamma_o^{<t>}.\tanh(C^{<t>}) \quad 5\text{-}9$$

The predicted output is calculated as follows:

$$\tilde{y}^{<t>} = ReLU\left(W_y a^{<t>} + b_y\right) \quad 5\text{-}10$$

Table 5-5 indicates the configuration of the layers and activation function utilized in this model.

5.3.3 Implementation details

Figure 5-8 represents the general algorithm for joint estimation of SOC and SOH of the battery. In this study, the SOH and SOC datasets of the cells V4, V5, W5, W9, and W10 are utilized for training and validating the models, and the datasets of the cell W8 are utilized for testing the models. The prediction models are built by *Keras* upon *Tensorflow* in Python.

For the datasets for SOH estimation, the EIS tests are run for the cells in 9 diagnostic tests, indicating the SOH level of the batteries. Each diagnostic test is run after some number of cycles which have been presented in Table 5-3. At each session, the EIS measurements are collected at three different SOC levels, i.e., 20%, 50%, and 80%. The ratio of the training dataset to the validation dataset is set to be 8:2. For the sake of comparison, two ML models, namely, DNN and GPR, are utilized to estimate the SOH. For each ML model, the training and validation datasets containing EIS measurements obtained at three SOC levels, are utilized. Both models are then tested by totally unseen datasets of the cell W8 at each SOC level separately. For example, the GPR model will be tested three times, first with EIS measurements at SOC 20%, second with EIS measurements at SOC 50%, and third with EIS measurements at SOC 80%. Therefore, for each

actual measured SOH in the diagnostic test, there are three estimated SOH values by each of the models. This is done to evaluate the performance of each model when they are confronting a new set of unobserved EIS measurements at different SOC levels.

For the dataset for SOC estimation, the real-time measurable variables of the battery, i.e., voltage and current, are collected from the last UDDS driving profile at each session of the diagnostic test for all the cells. Additionally, the actual measured SOH at each diagnostic test is included as another feature of this dataset. The ratio of the training dataset to the validation dataset is set to be 8:2. For the sake of comparison, two ML models, namely, DNN and LSTM, are utilized to estimate the SOC. Both models are then tested by totally unobserved datasets of the cell W8. It is worth mentioning that for the test datasets, instead of using the actual measured SOH at the diagnostic tests, the SOH estimated from the previous models is utilized as an input feature of the test dataset, see Figure 5-8. To assess the universality and versatility of the proposed method, there are nine different test datasets to be performed on the selected ML models. To do this, three diagnostic tests are selected for test datasets. In the first, second, and third selected diagnostic tests, the actual measured SOH levels of the battery are 100%, 96%, and 93%, respectively. Therefore, for each of the actual measured SOH, there are three estimated SOH values from the previous models. Each of these estimated SOH values and their corresponding voltage and current of the last UDDS driving profile in each diagnostic test build one test dataset. In such a case, the effect of battery aging and degradation during its lifetime in an EV application is characterized for joint SOC and SOH estimation.

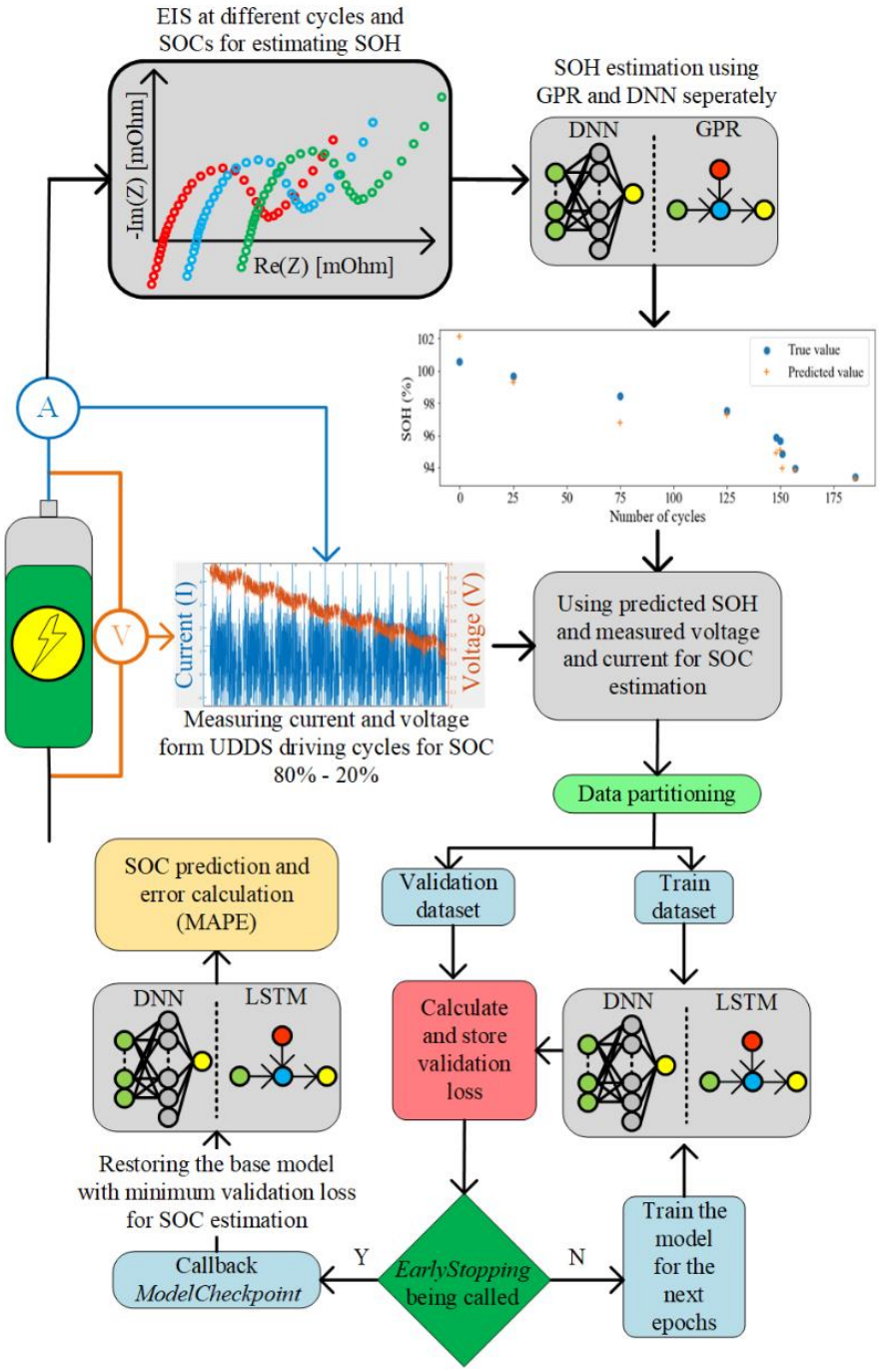

Figure 5-8. The proposed method algorithm for joint estimation of SOC and SOH

In this study, The DNN model for SOH estimation, the LSTM and other DNN model for SOC estimation are trained for 10000, 1000, and 1000 epochs, respectively; an epoch is defined as one cycle through the entire training dataset. Typically, training a DNN and an LSTM takes more than

a few epochs. In other words, the models are trained for more than one epoch in various patterns of training dataset for a better comprehension when given a new unobserved input (test data).

However, the training of the model may not be effective if the number of epochs is too large or too small. In the former case, overfitting may occur, and in the latter case, it will result in an underfit model. An early stopping technique is utilized to solve this issue. This technique provides the opportunity to select a randomly large number of training epochs and terminate the training of the model once the model performance halts to be improved on a holdout validation dataset. Therefore, a validation dataset is necessary during training the DNN and LSTM models for using early stopping technique. At the end of each epoch, the loss function, which is validation loss (MSE) to be optimized for the models, is calculated. The model training will be stopped early through a callback in *EarlyStopping* technique. This callback will monitor the MSE improvement and terminates the training process once the improvement is stopped. However, during the training, the model may fall into a plateau of no improvement or even get slightly worse before getting much better. To prevent this problem, the “patience" argument which is a delay, is added to the trigger in terms of the number of epochs on which there is no improvement in MSE. Although the *EarlyStopping* callback will stop training once called, the model at the end of training may not be the model with the minimum MSE. In such case, the *ModelCheckpoint*, which is another callback function, is utilized for the purpose of storing the best model, i.e., the model with the minimum MSE, and restoring it for later use.

5.3.4 Accuracy evaluation

The indices used for the evaluation of the performance of the proposed model are: MAPE and the R-squared. The lower MAPE, the better the estimation. R-squared represents the goodness of the fit. The best possible value is 1, and the value can be negative too, which indicates that the

model cannot follow the actual datasets.

5.4 Results and Discussions

To verify the state of the art of the proposed joint SOC and SOH estimation method, first, we compare the performance of the GPR and DNN model on SOH estimation. The estimated SOH values are then utilized to be leveraged as a feature input along with the voltage and current of the battery measured from a standard driving cycle.

5.4.1 SOH estimation results

To verify the state of the art of the proposed joint SOC and SOH estimation method, first, we compare the performance of the GPR and DNN model on SOH estimation. The estimated SOH values are then utilized to be leveraged as a feature input along with the voltage and current of the battery measured from a standard driving cycle. Figure 5-9 (a) and Figure 5-9 (b) indicate the performance of the DNN and GPR models for SOC levels of 20%, 50%, and 80%, respectively. This figure demonstrates that the models can follow the actual unseen data and estimate the SOH precisely. Table 5-6 indicates the MAPE and R-squared values for the models. The MAPE of the DNN model for the three SOC levels are 0.769%, 1.069%, and 0.557%, respectively. The MAPE of the GPR model for the three SOC are 0.803%, 0.816%, and 0.604%. The low MAPE values for both models prove the above-mention claim for the accuracy of the models. The average value of MAPE for the two models slightly differs from each other, which indicates that both models can precisely estimate the SOH of the battery. Moreover, the R-squared values indicate that the models can follow the actual data. In summary, if new unseen EIS measurements at any SOC level are input to the models, they can precisely estimate the SOH of the battery. This case study proved that since the evaluation criteria differ from each other at different SOC levels, it is necessary to

consider the effect of SOC on EIS measurements for the purpose of SOH estimation. The results indicated the universality and robustness of the models confronting the EIS dataset measured at different SOC levels.

Table 5-6. MAPE (%) and R-squared values for DNN and GPR for SOH estimation using EIS measurements obtained at three SOC levels

MAPE (%)	**DNN**	**GPR**
EIS at SOC 20%	0.769	0.803
EIS at SOC 50%	1.069	0.816
EIS at SOC 80%	0.557	0.604
R-squared		
EIS at SOC 20%	0.741	0.866
EIS at SOC 50%	0.787	0.871
EIS at SOC 80%	0.933	0.919

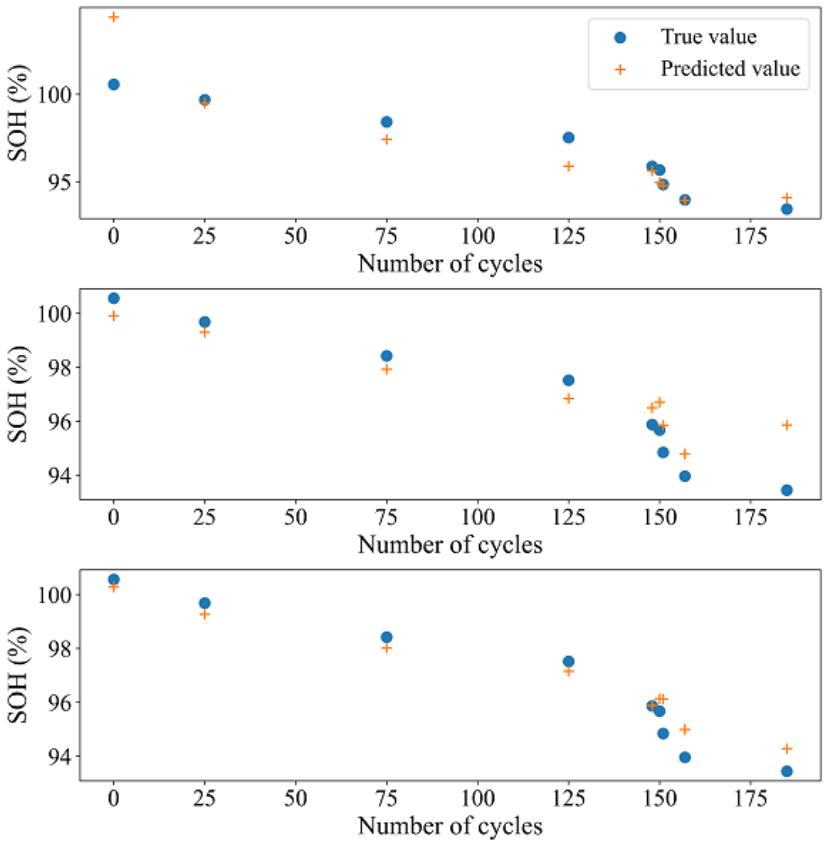

(a)

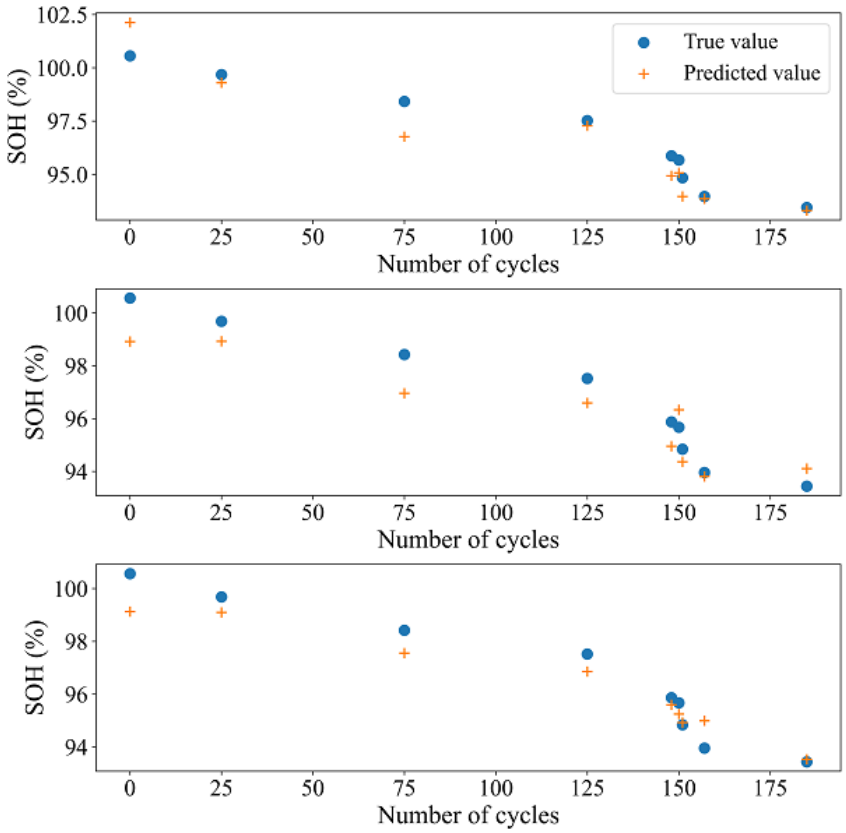

(b)

Figure 5-9. Estimated SOH at three different SOC levels, i.e., 20%, 50%, and 80% from top to bottom for cell W8, (a) using DNN model (b) using GPR model

5.4.2 SOC estimation

In this scenario, nine test datasets of cell W8 are utilized to assess the performance of the DNN and LSTM models on SOC prediction. It is worth mentioning that the estimated SOH values from the GPR model in the previous part, have been utilized in as an input feature, as the accuracy of this model was slightly better than the DNN model. Figure 5-10 (a) indicates the estimated SOC for the first selected diagnostic test (which corresponds to the actual measured SOH of 100%). Figure 5-10 (a) contains three plots which indicates the performance of the model for adopting the three different estimated SOH values.

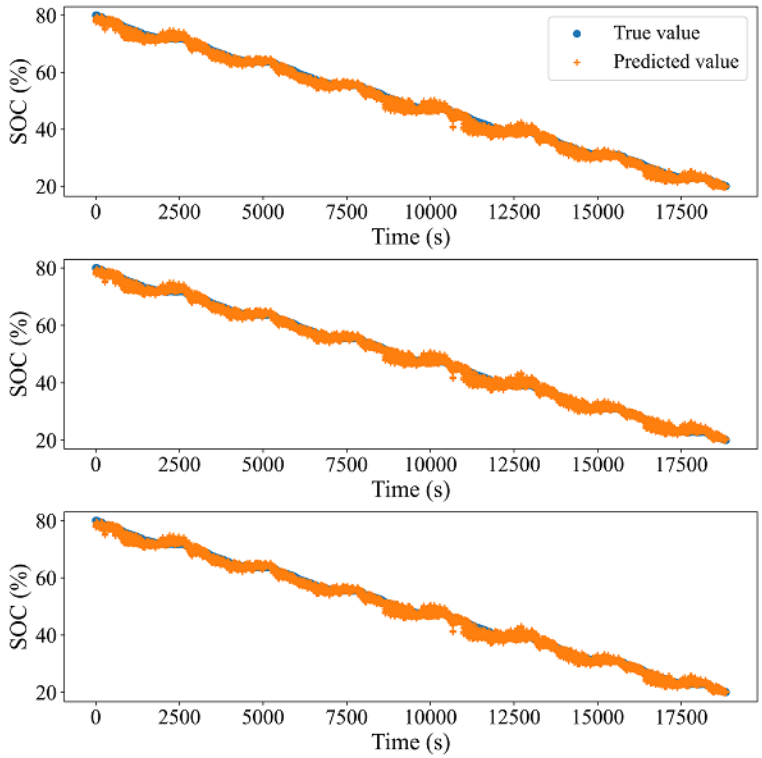
True value
Predicted value
SOC (%)
Time (s)
80
60
40
20
0
2500
5000
7500
10000
12500
15000
17500

(a)

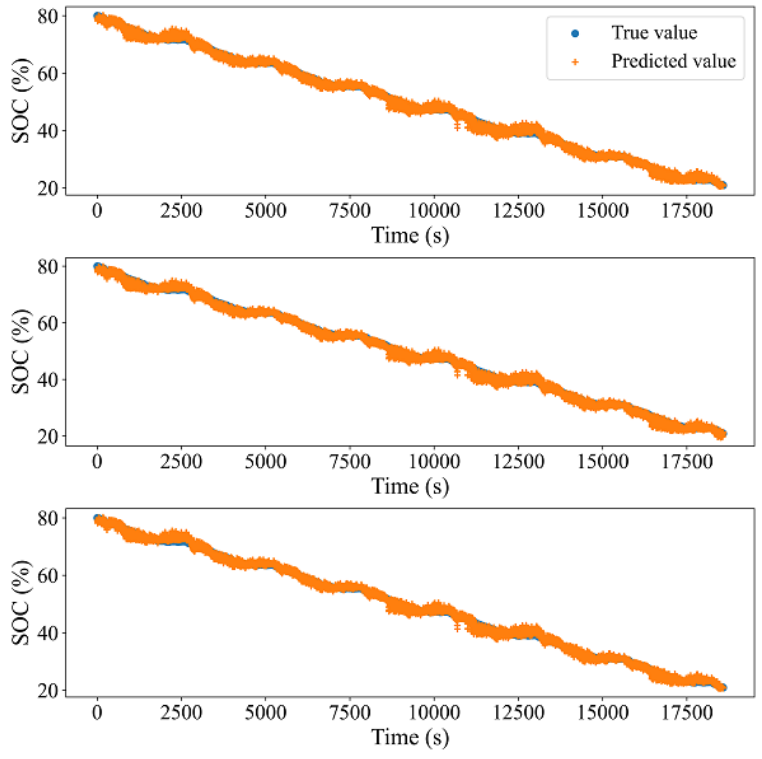
True value
Predicted value
SOC (%)
Time (s)
80
60
40
20
0
2500
5000
7500
10000
12500
15000
17500

(b)

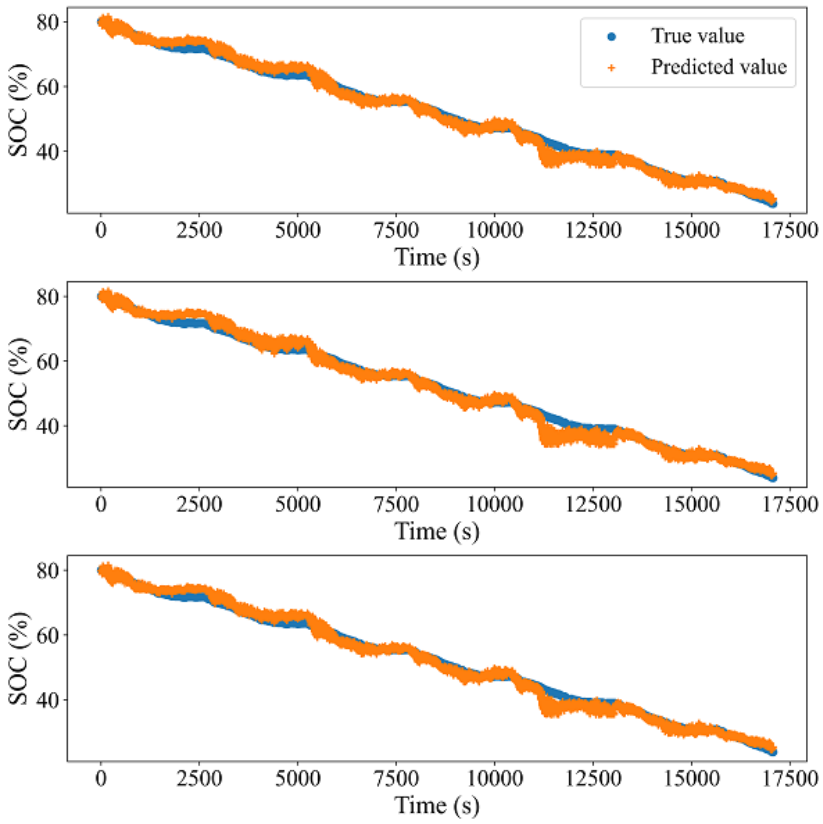

(c)

Figure 5-10. Estimated SOC at (a). SOH level of 100%, (b). SOH level of 96%, and (c). SOH level of 93% using DNN model adopting the estimated SOH at three SOC levels

Figure 5-10 (b) and Figure 5-10 (c) demonstrate the estimated SOC for the second and third selected diagnostic tests corresponding to SOH levels of 96% and 93%, respectively.

Figure 5-11 (a)-(c) demonstrate the ability of the LSTM model in accurate estimation of the SOC at the same diagnostic tests.

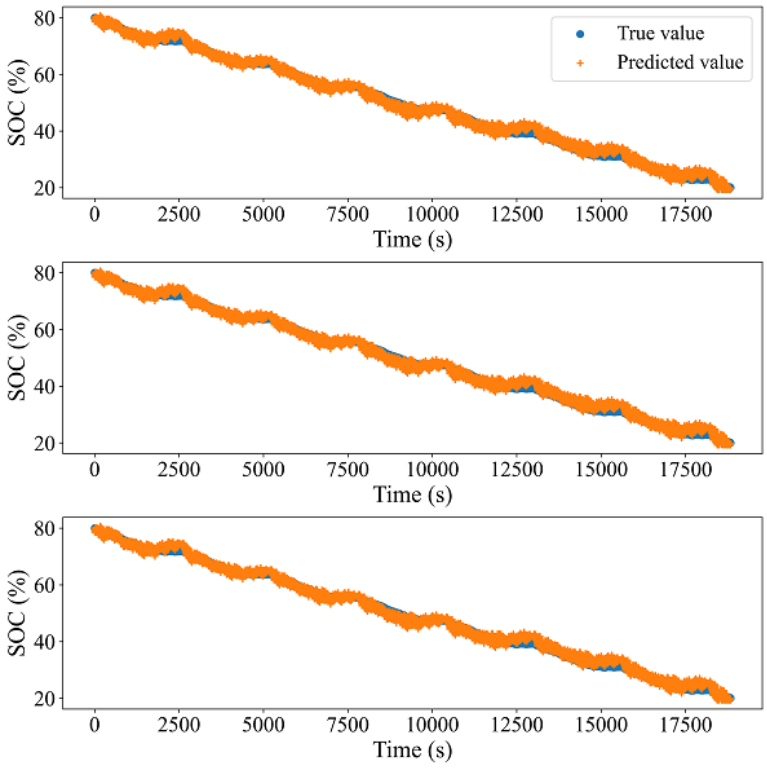
True value
Predicted value
SOC (%)
Time (s)
80
60
40
20
0
2500
5000
7500
10000
12500
15000
17500

(a)

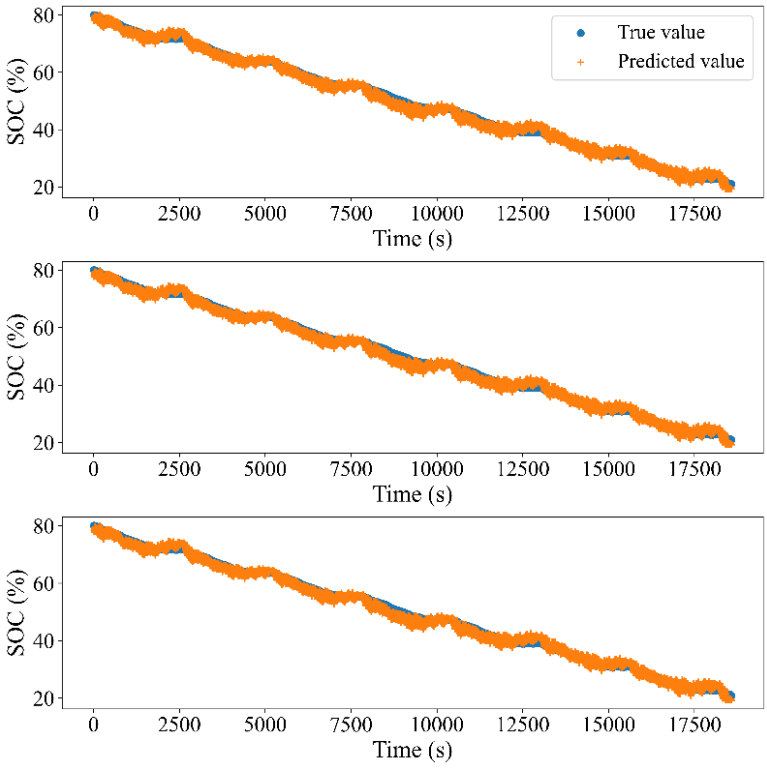
True value
Predicted value
SOC (%)
Time (s)
80
60
40
20
0
2500
5000
7500
10000
12500
15000
17500

(b)

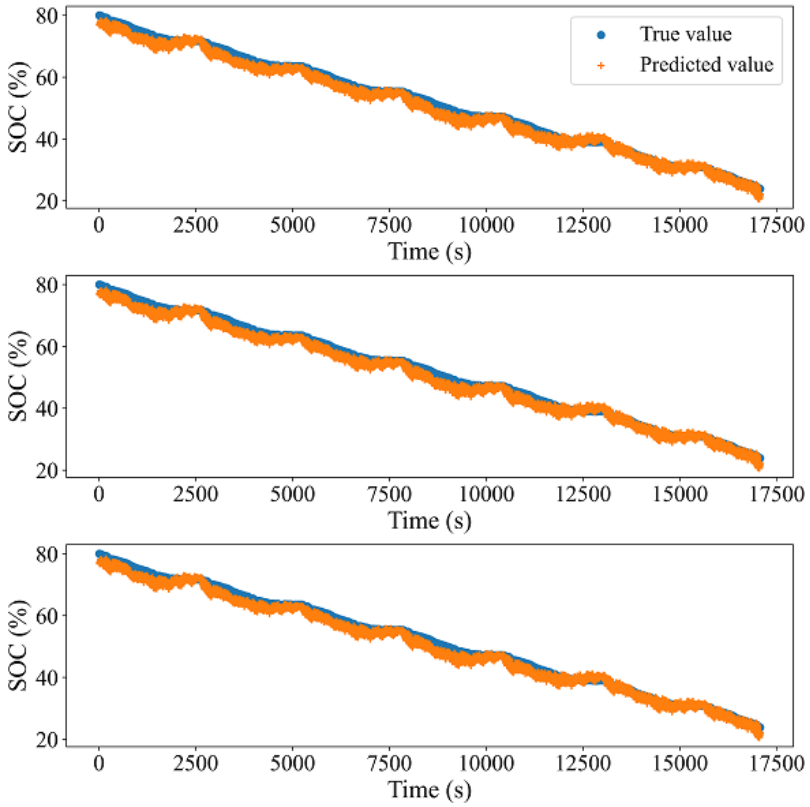

(c)

Figure 5-11. Estimated SOC at (a). SOH level of 100%, (b). SOH level of 96%, and (c). SOH level of 93% using DNN model adopting the estimated SOH at three SOC levels

According to Figure 5-10 and Figure 5-11, one may conclude that the DNN and LSTM models possess the ability to estimate the SOC precisely at different levels of battery health. Similarly, both models are able to effectively consider the effect of battery degradation on SOC estimation. Moreover, Figure 5-10 and Figure 5-11 imply that the effect of EIS measurements at different SOC levels have been passed through the model, which results in more accurate estimation and universality of the proposed method. The MAPE and R-squared of the DNN and LSTM models have been recorded in Table 5-7. The maximum MAPE value is found to be less than 3% for the models. The average MAPE value of the SLTM model is slightly less than the DNN model. It can

be concluded from the high R-squared values for the models, that models are able to follow the actual missing data. Regarding the low MAPE values and high R-squared values achieved by the models, one may conclude that the proposed method has constituted a precise algorithm for estimating the SOC obtained from the standard driving cycles while the effect of the battery's capacity fade has been considered.

Table 5-7. MAPE (%) and R-squared values for DNN and LSTM for SOC estimation for UDDS driving cycle at three SOH levels

MAPE (%)		**DNN**	**LSTM**
1st selected diagnostic test (Corresponding to SOH 100%)	(1)	2.035	1.759
	(2)	1.637	1.778
	(3)	1.773	1.768
2nd selected diagnostic test (Corresponding to SOH 96%)	(1)	1.508	1.652
	(2)	1.667	1.738
	(3)	1.497	1.701
3rd selected diagnostic test (Corresponding to SOH 93%)	(1)	2.364	2.375
	(2)	2.846	2.479
	(3)	2.481	2.398
R-squared			
1st selected diagnostic test (Corresponding to SOH 100%)	(1)	0.9956	0.9939
	(2)	0.9968	0.9938
	(3)	0.9963	0.9938
2nd selected diagnostic test (Corresponding to SOH 96%)	(1)	0.9972	0.9946
	(2)	0.9968	0.9941
	(3)	0.9973	0.9943
3rd selected diagnostic test (Corresponding to SOH 96%)	(1)	0.990	0.988
	(2)	0.985	0.987
	(3)	0.9895	0.987

According to the above discussion, the effectiveness of direct usage of EIS measurements instead of using it as EIM and how informative they are in conveying the health status of batteries at different SOCs, was indicated. Additionally, its effectiveness in SOC estimation was obliquely demonstrated by adopting the estimated SOH as an input feature. The SOC was estimated at three different levels of SOH, and high estimation accuracy was achieved by the models, which implies that models account for the capacity fade of the battery and are able to predict the SOC of the battery during its longevity. Moreover, the models for SOC estimation were trained by the standard

driving cycles, which mimics more practical use of the proposed method in an EV application. It can be deduced that any combination of the ML models for SOH estimation, i.e., DNN and GPR, with ML models for SOC estimation, i.e., DNN and LSTM, will constitute a comprehensive algorithm to jointly and precisely estimate the SOC and SOH of the battery. One may question the comprehensiveness of the proposed model as the other temperature values have not been tested. The data for other temperature values were not available to be included in our datasets; however, interpolation cannot be denied in ML models. It is well-known that EIS measurements follow a predictable pattern in accordance with temperature. A predictable pattern of EIS measurement based on the mentioned parameter further enhances the ability of the model to interpolate or extrapolate between other values of temperature.

5.5 Conclusions

This study employed EIS measurements directly, which are not dependent on the charging/discharging process and IC curves, at three SOC levels of 20%, 50%, and 80%, to estimate the SOH of the battery. To do this, two ML models, namely, GPR and DNN, were adopted for the sake of comparison. The SOH was estimated separately at the mentioned SOC levels. The MAPE achieved by both of the models is less than 1% for the three SOC levels. The average R-squared of 0.885 is also achieved by the models, which indicates the goodness of fit. The real-time measurable variables such as voltage and current of the battery obtained from standard driving cycles, were collected from three diagnostic tests corresponding to three SOH levels of 100%, 96%, and 93%. The estimated SOH and the voltage and current were then employed as input features for joint estimation of SOC. Two other ML models, i.e., DNN and LSTM, were exploited for the mentioned purpose. The maximum MAPEs for the SOC estimation for the three estimated SOH values is found to be less than 3%. The average R-squared for SOC estimation is 0.992,

which indicates the model can follow the unseen actual data. The results indicated that the proposed method effectively takes advantage of EIS measurements for SOH estimation and then utilizes the estimated SOH as an input feature to account for the capacity fade in joint estimate of SOC.

Chapter 6

Conclusions and Future Works

6.1 Conclusions

Chapter 1 presented the motivations for the proposed dissertation, and it concluded the need for transferring to an electrified transportation. It highlighted the significant factors to the global warming. This chapter provided incentives for developing advanced BMSs for better and more efficient management of battery storage systems, specially the lithium ones in battery-powered vehicles. To serve this purpose, accurate SOC and SOH estimation using advanced data-driven models implemented on BMS is of great substance. This not only prevents the malfunction of the battery energy storage in battery-powered vehicles but also ease the transfer to electrified transportation.

Chapter 2 presented fundamental information regarding the lithium-ion cell operation in an electrical circuit. Moreover, different components of the lithium-ion cell and their functionalities were discussed. Basics of EIS were outlined in this chapter, and how EIS measurements are obtained has been briefly presented. Additionally, the key roles and functionalities of BMS, such as monitoring and aggregating battery data, controlling charging/discharging procedures, and cell balancing in battery packs, were briefly presented in this chapter.

In Chapter 3, the prediction of li-ion battery SOC using EIS measurements was performed based on an ML approach. This study was conducted based on extracting reliable features according to

their correlation value with the SOC of the battery. After selecting the reliable features of different datasets at various temperatures and different SOCs, the linear regression model and GPR were trained, and the prediction was performed by the trained models over the test set. The results indicated that the proposed models are able to precisely predict the SOC of the battery using the reliable features. The models trained by the features with a corr_value of above 0.9 indicated the best performance among the others, such that the error of the GPR model was found to be less than 3.8 %. Furthermore, the impact of test-size on the model precision was evaluated. It was observed that for some cases, the larger test-size results in higher accuracy.

A novel battery capacity prediction method using TL with DNN was proposed in Chapter 4. This study employed EIS measurements directly, which is not dependent on the charging/discharging process and IC curves, for three ambient temperatures of 25 °C, 35 °C, and 45 °C. The maximum MAPE, when the first 50% and 20% of the target dataset were used for retraining the DNN-TL with no fixed-layer, were found to be 0.605% and 0.999%, respectively. As the results of the chapter indicate, an average MAPE of 0.616% was achieved for the DNN-TL with no fixed-layer in four different scenarios with different sizes of the target dataset, while the stand-alone DNN model achieved an average MAPE of 2.575%. The average R-squared of 0.9683 was achieved by the DNN-TL with no fixed-layer, which indicates the goodness of its fit and its capability to follow the actual missing datasets.

Chapter 5 employed EIS measurements directly, which are not dependent on the charging/discharging process and IC curves, at three SOC levels of 20%, 50%, and 80%, to estimate the SOH of the battery. To do this, two ML models, namely, GPR and DNN were adopted for the sake of comparison. The SOH was estimated separately at the mentioned SOC levels. The MAPE achieved by both of the models is less than 1% for the three SOC levels. The average R-

squared of 0.885 is also achieved by the models, which indicates the goodness of fit. The real-time measurable variables, such as voltage and current of the battery obtained from standard driving cycles, were collected from three diagnostic tests corresponding to three SOH levels of 100%, 96%, and 93%. The estimated SOH and the voltage and current were then employed as input features for joint estimation of SOC. Two other ML models, i.e., DNN and LSTM, were exploited for the mentioned purpose. The maximum MAPEs for the SOC estimation for the three estimated SOH values is found to be less than 3%. The average R-squared for SOC estimation is 0.992 which indicates the model can follow the unseen actual data.

6.2 Future works

This dissertation demonstrates state estimation algorithms using EIS and machine learning techniques. However, further research is required to expand this study. This section provides some recommended future works:

- **Cloud-based computations**

  The developed algorithm can be implemented in a cloud-based platform and the corresponding calculation, information, and results can be transferred through the internet of things (IoT). It is well-known that wireless BMSs are developing, and once this technology is commercialized, it should be compatible with cloud-based platform and features. Hence, advanced machine learning algorithms that conventional BMS cannot burden their computational cost, can be utilized in cloud-based computation systems. In such a case, the data from wireless BMS can be sent and stored in the clouds via IoT and processed according to the desired needs.

  The proposed method can benefit from acquirement of more comprehensive datasets.

The datasets can be obtained in more ambient temperature especially at extreme hot and cold conditions. Moreover, the EIS datasets can be obtained for SOC levels with less increments, e.g., 5 % for better interpolation and extrapolation of the proposed model.

In addition to the ambient temperature and SOC level, obtaining dataset for different cell chemistry will benefit our models. In the case of cloud-based platform, these datasets can be stored in the cloud and be employed when an update of the model is of mandate.

Stochastic methods such as Markov-chain and Monte Carlo can be implemented in cloud-based platform as well, to compare their performance with the ML models for co-estimating the SOC and SOH of the battery cells. The stochastic models can be considered as potent models as they use time-dependent variables, such as, voltage, impedance, and current of the battery to estimate the desired output, i.e., SOC and SOH.

- **Energy management system for hybrid energy storage vehicles**

  In addition to developing sophisticated SOC and SOH estimation methods that can decrease the capacity fade of battery packs in EVs, utilizing another energy storage system, such as ultracapacitors, along with the battery pack, can reduce the degradation of battery pack. In such a case, a meticulous energy management system is required to optimize the power allocation between the two energy sources in the EV to minimize the capacity fade for both sources.

- **Experimental implementation**

  To investigate the real-world performance of the proposed method in this study, an experimental evaluation through hardware in the loop (HIL) test needs to be conducted. In this way, feasibility challenges can be effectively assessed and addressed.

References

[1] S. Habib, M. M. Khan, F. Abbas, L. Sang, M. U. Shahid, and H. Tang, "A Comprehensive Study of Implemented International Standards, Technical Challenges, Impacts and Prospects for Electric Vehicles," *IEEE Access*, vol. 6, pp. 13866–13890, 2018, doi: 10.1109/ACCESS.2018.2812303.

[2] I. Babaeiyazdi, A. Rezaei-Zare, and S. Shokrzadeh, "Fast Charging Systems to Enable Electrification of Transportation: An Operational Constrained Based Analysis," in *ITEC 2019 - 2019 IEEE Transportation Electrification Conference and Expo*, 2019, pp. 14–19. doi: 10.1109/ITEC.2019.8790478.

[3] P. Adoba and M. Dioha, "Strategic Development of Electric Vehicles in Canada," *IAEE Energy Forum*, vol. 2017, no. First Quarter, pp. 26–31, 2021.

[4] Q. Yan, B. Zhang, and M. Kezunovic, "Optimized Operational Cost Reduction for an EV Charging Station Integrated With Battery Energy Storage and PV Generation," *IEEE Trans. Smart Grid*, vol. 10, no. 2, pp. 2096–2106, 2019.

[5] I. Babaeiyazdi, A. Rezaei-Zare, and S. Shokrzadeh, "DFACTS-Based Mitigation of Power System Voltage Unbalance for Wide Adoption of EV Fast Charging Systems," in *2021 IEEE Electrical Power and Energy Conference, EPEC 2021*, 2021, pp. 396–401. doi: 10.1109/EPEC52095.2021.9621705.

[6] Z. Ding, Y. Lu, L. Zhang, W. J. Lee, and D. Chen, "A Stochastic Resource-Planning Scheme for PHEV Charging Station Considering Energy Portfolio Optimization and Price-Responsive Demand," *IEEE Trans. Ind. Appl.*, vol. 54, no. 6, pp. 5590–5598, 2018, doi: 10.1109/TIA.2018.2851205.

[7] "Global ev outlook 2021."

[8] Y. Zhang, Q. Tang, Y. Zhang, J. Wang, U. Stimming, and A. A. Lee, "Identifying degradation patterns of lithium ion batteries from impedance spectroscopy using machine

learning," *Nat. Commun.*, vol. 11, no. 1706, 2020, doi: 10.1038/s41467-020-15235-7.

[9] A. Zahedi, I. Babaeiyazdi, R. Ostadian, and A. Rezaei-Zare, "Globally Optimal Energy Management in a Battery-Ultracapacitor Electric Vehicle," in *2022 IEEE International Conference on Environment and Electrical Engineering and 2022 IEEE Industrial and Commercial Power Systems Europe (EEEIC / I&CPS Europe)*, 2022, pp. 1–6. doi: 10.1109/eeeic/icpseurope54979.2022.9854614.

[10] X. Hu, L. Xu, X. Lin, and M. Pecht, "Battery lifetime prognostics," *Joule*, vol. 4, no. 2, pp. 310–346, 2020, doi: 10.1016/j.joule.2019.11.018.

[11] R. Xiong, J. Cao, Q. Yu, H. He, and F. Sun, "Critical Review on the Battery State of Charge Estimation Methods for Electric Vehicles," *IEEE Access*, vol. 6, pp. 1832–1843, 2017, doi: 10.1109/ACCESS.2017.2780258.

[12] S. Peng, C. Chen, H. Shi, and Z. Yao, "State of Charge Estimation of Battery Energy Storage Systems Based on Adaptive Unscented Kalman Filter With a Noise Statistics Estimator," *IEEE Access*, vol. 5, pp. 13202–13212, 2017.

[13] M. S. Sidhu, D. Ronanki, and S. Williamson, "State of Charge Estimation of Lithium-ion Batteries using Hybrid Machine Learning Technique," in *IECON 2019 - 45th Annual Conference of the IEEE Industrial Electronics Society*, 2019, vol. 1, pp. 2732–2737.

[14] H. Chen, T. N. Cong, W. Yang, C. Tan, Y. Li, and Y. Ding, "Progress in electrical energy storage system: A critical review," *Prog. Nat. Sci.*, vol. 19, no. 3, pp. 291–312, 2009, doi: 10.1016/j.pnsc.2008.07.014.

[15] M. M. Kabir and D. E. Demirocak, "Degradation mechanisms in Li-ion batteries a state-of-the- art review," *Int. J. Energy Res.*, no. 41, pp. 1963–1986, 2017, doi: 10.1002/er.3762.

[16] M. R. Palacín, "Understanding ageing in Li-ion batteries: A chemical issue," *Chem. Soc. Rev.*, vol. 47, no. 13, pp. 4924–4933, 2018, doi: 10.1039/c7cs00889a.

[17] K. Xu, "Electrolytes and interphases in Li-ion batteries and beyond," *Chem. Rev.*, vol. 114, no. 23, pp. 11503–11618, 2014, doi: 10.1021/cr500003w.

[18] A. M. Abakumov, S. S. Fedotov, E. V. Antipov, and J. M. Tarascon, "Solid state chemistry

for developing better metal-ion batteries," *Nat. Commun.*, vol. 11, no. 1, pp. 1–14, 2020, doi: 10.1038/s41467-020-18736-7.

[19] Y. K. Sun, "Promising All-Solid-State Batteries for Future Electric Vehicles," *ACS Energy Lett.*, vol. 5, no. 10, pp. 3221–3223, 2020, doi: 10.1021/acsenergylett.0c01977.

[20] A. A. Heidari and H. Mahdavi, "Recent Development of Polyolefin-Based Microporous Separators for Li−Ion Batteries: A Review," *Chem. Rec.*, vol. 20, no. 6, pp. 570–595, 2020, doi: 10.1002/tcr.201900054.

[21] D. E. Demirocak and B. Bhushan, "Probing the aging effects on nanomechanical properties of a LiFePO4 cathode in a large format prismatic cell," *J. Power Sources*, vol. 280, pp. 256–262, 2015, doi: 10.1016/j.jpowsour.2015.01.114.

[22] M. Broussely *et al.*, "Main aging mechanisms in Li ion batteries," *J. Power Sources*, vol. 146, no. 1–2, pp. 90–96, 2005, doi: 10.1016/j.jpowsour.2005.03.172.

[23] S. Ramdon and B. Bhushan, "Nanomechanical characterization and mechanical integrity of unaged and aged Li-ion battery cathodes," *J. Power Sources*, vol. 246, pp. 219–224, 2014, doi: 10.1016/j.jpowsour.2013.07.078.

[24] D. Aurbach, E. Zinigrad, Y. Cohen, and H. Teller, "A short review of failure mechanisms of lithium metal and lithiated graphite anodes in liquid electrolyte solutions," *Solid State Ionics*, vol. 148, pp. 405–416, 2002.

[25] S. C. Nagpure, B. Bhushan, and S. S. Babu, "Multi-Scale Characterization Studies of Aged Li-Ion Large Format Cells for Improved Performance: An Overview," *J. Electrochem. Soc.*, vol. 160, no. 11, pp. A2111–A2154, 2013, doi: 10.1149/2.001311jes.

[26] J. W. Braithwaite *et al.*, "Corrosion of Lithium-Ion Battery Current Collectors," *J. Electrochem. Soc.*, vol. 146, no. 2, pp. 448–456, 1999, doi: 10.1149/1.1391627.

[27] P. Arora and Z. Zhang, "Battery separators," *Chem. Rev.*, vol. 104, no. 10, pp. 4419–4462, 2004, doi: 10.1021/cr020738u.

[28] L. Norin, R. Kostecki, and F. McLarnon, "Study of membrane degradation in high-power lithium-ion cells," *Electrochem. Solid-State Lett.*, vol. 5, no. 4, pp. 67–70, 2002, doi:

10.1149/1.1457206.

[29] M. Gaberšček, “Understanding Li-based battery materials via electrochemical impedance spectroscopy,” *Nat. Commun.*, vol. 12, no. 1, pp. 19–22, 2021, doi: 10.1038/s41467-021-26894-5.

[30] E. Din, C. Schaef, K. Moffat, and J. T. Stauth, “A Scalable Active Battery Management System With Embedded Real-Time Electrochemical Impedance Spectroscopy,” *IEEE Trans. Power Electron.*, vol. 32, no. 7, pp. 5688–5698, 2017, doi: 10.1109/TPEL.2016.2607519.

[31] F. Huet, “A review of impedance measurements for determination of the state-of-charge or state-of-health of secondary batteries,” *J. Power Sources*, vol. 70, no. 1, pp. 59–69, 1998, doi: 10.1016/S0378-7753(97)02665-7.

[32] Y. Xing, E. W. M. Ma, K. L. Tsui, and M. Pecht, “Battery management systems in electric and hybrid vehicles,” *Energies*, vol. 4, no. 11, pp. 1840–1857, 2011, doi: 10.3390/en4111840.

[33] W. Sung and C. B. Shin, “Electrochemical model of a lithium-ion battery implemented into an automotive battery management system,” *Comput. Chem. Eng.*, vol. 76, pp. 87–97, 2015, doi: 10.1016/j.compchemeng.2015.02.007.

[34] H. Gabbar, A. Othman, and M. Abdussami, “Review of Battery Management Systems (BMS) Development and Industrial Standards,” *Technologies*, vol. 9, no. 2, p. 28, 2021, doi: 10.3390/technologies9020028.

[35] Kang Taewoo, Park Seongyun, Lee Pyeong-yeon, Cho In-ho, Yoo Kisoo, and Kim Jonghoon, “Thermal Analysis of a Parallel-Configured Battery Pack (1S18P) Using 21700 Cells for a Battery-Powered Train,” *Electronics*, vol. 9, no. 3, p. 447, 2020.

[36] M. Abbas, I. Cho, and J. Kim, “Analysis of high-power charging limitations of a battery in a hybrid railway system,” *Electron.*, vol. 9, no. 2, 2020, doi: 10.3390/electronics9020212.

[37] E. Arnieri, L. Boccia, F. Amoroso, G. Amendola, and G. Cappuccino, “Improved efficiency management strategy for battery-based energy storage systems,” *Electron.*, vol. 8, no. 12, pp. 1–9, 2019, doi: 10.3390/electronics8121459.

[38] S. Lee and J. Kim, “Power capability analysis of lithium battery and supercapacitor by pulse duration,” *Electron.*, vol. 8, no. 12, 2019, doi: 10.3390/electronics8121395.

[39] M. Uno, T. Ueno, and K. Yoshino, “Cell voltage equalizer using a selective voltage multiplier with a reduced selection switch count for series-connected energy storage cells,” *Electron.*, vol. 8, no. 11, 2019, doi: 10.3390/electronics8111303.

[40] P. I. Kokkotis, C. S. Psomopoulos, G. C. Ioannidis, and S. D. Kaminaris, “Small Scale Energy Storage Systems. a Short Review in Their Potential Environmental Impact,” *Fresenius Environ. Bull.*, vol. 26, no. 9, pp. 5658–5665, 2017.

[41] C. Zhang, Y. Jiang, J. Jiang, G. Cheng, W. Diao, and W. Zhang, “Study on battery pack consistency evolutions and equilibrium diagnosis for serial- connected lithium-ion batteries,” *Appl. Energy*, vol. 207, pp. 510–519, 2017, doi: 10.1016/j.apenergy.2017.05.176.

[42] K. Rumpf, M. Naumann, and A. Jossen, “Experimental investigation of parametric cell-to-cell variation and correlation based on 1100 commercial lithium-ion cells,” *J. Energy Storage*, vol. 14, pp. 224–243, 2017, doi: 10.1016/j.est.2017.09.010.

[43] R. Gogoana, M. B. Pinson, M. Z. Bazant, and S. E. Sarma, “Internal resistance matching for parallel-connected lithium-ion cells and impacts on battery pack cycle life,” *J. Power Sources*, vol. 252, pp. 8–13, 2014, doi: 10.1016/j.jpowsour.2013.11.101.

[44] Z. Zhang, H. Gui, D. J. Gu, Y. Yang, and X. Ren, “A hierarchical active balancing architecture for lithium-ion batteries,” *IEEE Trans. Power Electron.*, vol. 32, no. 4, pp. 2757–2768, 2017, doi: 10.1109/TPEL.2016.2575844.

[45] W. Luo, J. Lv, W. Song, and Z. Feng, “Study on passive balancing characteristics of serially connected lithium-ion battery string,” in *ICEMI 2017 - Proceedings of IEEE 13th International Conference on Electronic Measurement and Instruments*, 2017, pp. 489–495. doi: 10.1109/ICEMI.2017.8265862.

[46] A. C. Baughman and M. Ferdowsi, “Double-tiered switched-capacitor battery charge equalization technique,” *IEEE Trans. Ind. Electron.*, vol. 55, no. 6, pp. 2277–2285, 2008, doi: 10.1109/TIE.2008.918401.

[47] M. Daowd, M. Antoine, N. Omar, P. van den Bossche, and J. van Mierlo, “Single switched capacitor battery balancing system enhancements,” *Energies*, vol. 6, no. 4, pp. 2149–2179, 2013, doi: 10.3390/en6042149.

[48] R. K. Vardhan, T. Selvathai, R. Reginald, P. Sivakumar, and S. Sundaresh, “Modeling of single inductor based Battery Balancing Circuit for Hybrid Electric Vehicles,” in *43rd Annual Conference of the IEEE Industrial Electronis Society*, 2017, pp. 2293–2298.

[49] X. Cui, W. Shen, Y. Zhang, and C. Hu, “A fast multi-switched inductor balancing system based on a fuzzy logic controller for lithium-ion battery packs in electric vehicles,” *Energies*, vol. 10, no. 7, 2017, doi: 10.3390/en10071034.

[50] M. Einhorn, W. Roessler, and J. Fleig, “Improved performance of serially connected Li-ion batteries with active cell balancing in electric vehicles,” *IEEE Trans. Veh. Technol.*, vol. 60, no. 6, pp. 2448–2457, 2011, doi: 10.1109/TVT.2011.2153886.

[51] A. M. Imtiaz, F. H. Khan, and H. Kamath, “A low-cost time shared cell balancing technique for future lithium-ion battery storage system featuring regenerative energy distribution,” in *Conference Proceedings - IEEE Applied Power Electronics Conference and Exposition - APEC*, 2011, pp. 792–799. doi: 10.1109/APEC.2011.5744686.

[52] X. Cui, W. Shen, Y. Zhang, and C. Hu, “A novel active online state of charge based balancing approach for Lithium-ion battery packs during fast charging process in electric vehicles,” *Energies*, vol. 10, no. 11, pp. 1–17, 2017, doi: 10.3390/en10111766.

[53] Y. S. Lee and G. T. Cheng, “Quasi-resonant zero-current-switching bidirectional converter for battery equalization applications,” *IEEE Trans. Power Electron.*, vol. 21, no. 5, pp. 1213–1224, 2006, doi: 10.1109/TPEL.2006.880349.

[54] M. Naguib, P. Kollmeyer, and A. Emadi, “Lithium-ion battery pack robust state of charge estimation, cell inconsistency, and balancing: Review,” *IEEE Access*, vol. 9, pp. 50570–50582, 2021, doi: 10.1109/ACCESS.2021.3068776.

[55] Q. Xu, J. Xiao, X. Hu, P. Wang, and M. Y. Lee, “A Decentralized Power Management Strategy for Hybrid Energy Storage System with Autonomous Bus Voltage Restoration and State-of-Charge Recovery,” *IEEE Trans. Ind. Electron.*, vol. 64, no. 9, pp. 7098–7108,

2017, doi: 10.1109/TIE.2017.2686303.

[56] H. Rahimi-Eichi, U. Ojha, F. Baronti, and M. Y. Chow, “Battery management system: An overview of its application in the smart grid and electric vehicles,” *IEEE Ind. Electron. Mag.*, vol. 7, no. 2, pp. 4–16, 2013, doi: 10.1109/MIE.2013.2250351.

[57] Y. Hu, C. Chen, T. He, J. He, X. Guan, and B. Yang, “Proactive Power Management Scheme for Hybrid Electric Storage System in EVs: An MPC Method,” *IEEE Trans. Intell. Transp. Syst.*, vol. 21, no. 12, pp. 5246–5257, 2020, doi: 10.1109/TITS.2019.2952678.

[58] P. Keil and A. Jossen, “Charging protocols for lithium-ion batteries and their impact on cycle life-An experimental study with different 18650 high-power cells,” *J. Energy Storage*, vol. 6, pp. 125–141, 2016, doi: 10.1016/j.est.2016.02.005.

[59] I. S. Kim, “Nonlinear state of charge estimator for hybrid electric vehicle battery,” *IEEE Trans. Power Electron.*, vol. 23, no. 4, pp. 2027–2034, 2008, doi: 10.1109/TPEL.2008.924629.

[60] L. Wang, D. Lu, Q. Liu, L. Liu, and X. Zhao, “State of charge estimation for LiFePO4 battery via dual extended kalman filter and charging voltage curve,” *Electrochim. Acta*, vol. 296, pp. 1009–1017, 2019, doi: 10.1016/j.electacta.2018.11.156.

[61] T. Haisch, H. Ji, and C. Weidlich, “Monitoring the state of charge of all-vanadium redox flow batteries to identify crossover of electrolyte,” *Electrochim. Acta*, vol. 336, 2020, doi: 10.1016/j.electacta.2019.135573.

[62] H. F. Khan, A. Hanif, M. U. Ali, and A. Zafar, “A Lagrange multiplier and sigma point Kalman filter based fused methodology for online state of charge estimation of lithium-ion batteries,” *J. Energy Storage*, vol. 41, no. August 2020, p. 102843, 2021, doi: 10.1016/j.est.2021.102843.

[63] W. Choi, “A study on state of charge and state of health estimation in consideration of lithium-ion battery aging,” *Sustain.*, vol. 12, no. 24, pp. 1–11, 2020, doi: 10.3390/su122410451.

[64] R. Xiong, J. Tian, H. Mu, and C. Wang, “A systematic model-based degradation behavior recognition and health monitoring method for lithium-ion batteries,” *Appl. Energy*, vol. 207,

pp. 372–383, 2017, doi: 10.1016/j.apenergy.2017.05.124.

[65] Y. Wang *et al.*, "A comprehensive review of battery modeling and state estimation approaches for advanced battery management systems," *Renew. Sustain. Energy Rev.*, vol. 131, 2020, doi: 10.1016/j.rser.2020.110015.

[66] L. Zheng, L. Zhang, J. Zhu, G. Wang, and J. Jiang, "Co-estimation of state-of-charge, capacity and resistance for lithium-ion batteries based on a high-fidelity electrochemical model," *Appl. Energy*, vol. 180, pp. 424–434, 2016, doi: 10.1016/j.apenergy.2016.08.016.

[67] Y. Bao, W. Dong, and D. Wang, "Online internal resistance measurement application in lithium ion battery capacity and state of charge estimation," *Energies*, vol. 11, no. 5, 2018, doi: 10.3390/en11051073.

[68] S. M. Mousavi G. and M. Nikdel, "Various battery models for various simulation studies and applications," *Renew. Sustain. Energy Rev.*, vol. 32, pp. 477–485, 2014, doi: 10.1016/j.rser.2014.01.048.

[69] H. Mu, R. Xiong, H. Zheng, Y. Chang, and Z. Chen, "A novel fractional order model based state-of-charge estimation method for lithium-ion battery," *Appl. Energy*, vol. 207, pp. 384–393, 2017, doi: 10.1016/j.apenergy.2017.07.003.

[70] Y. Li, C. Wang, and J. Gong, "A combination Kalman filter approach for State of Charge estimation of lithium-ion battery considering model uncertainty," *Energy*, vol. 109, pp. 933–946, 2016, doi: 10.1016/j.energy.2016.05.047.

[71] S. Sepasi, R. Ghorbani, and B. Yann, "A novel on-board state-of-charge estimation method for aged Li-ion batteries based on model adaptive extended Kalman filter," *J. Power Sources*, vol. 245, pp. 337–344, 2014, doi: 10.1016/j.jpowsour.2013.06.108.

[72] I. Baccouche, S. Jemmali, B. Manai, N. Omar, N. Essoukri, and B. Amara, "Improved OCV Model of a Li-Ion NMC Battery for Online SOC Estimation Using the Extended Kalman Filter," *Energies*, vol. 10, no. 6, p. 764, 2017, doi: 10.3390/en10060764.

[73] J. Lee, O. Nam, and B. H. Cho, "Li-ion battery SOC estimation method based on the reduced order extended Kalman filtering," *J. Power Sources*, vol. 174, no. 1, pp. 9–15, 2007, doi: 10.1016/j.jpowsour.2007.03.072.

[74] W. Wang, X. Wang, C. Xiang, C. Wei, and Y. Zhao, “Unscented Kalman Filter-Based Battery SOC Estimation and Peak Power Prediction Method for Power Distribution of Hybrid Electric Vehicles,” *IEEE Access*, vol. 6, pp. 35957–35965, 2018, doi: 10.1109/ACCESS.2018.2850743.

[75] H. W. He, Y. Z. Zhang, R. Xiong, and C. Wang, “A novel Gaussian model based battery state estimation approach: State-of-Energy,” *Appl. Energy*, vol. 151, pp. 41–48, 2015, doi: 10.1016/j.apenergy.2015.04.062.

[76] D. J. Xuan, Z. Shi, J. Chen, C. Zhang, and Y. X. Wang, “Real-time estimation of state-of-charge in lithium-ion batteries using improved central difference transform method,” *J. Clean. Prod.*, vol. 252, p. 119787, 2020, doi: 10.1016/j.jclepro.2019.119787.

[77] X. Hao and J. Wu, “Online State Estimation Using Particles Filters of Lithium-Ion Polymer Battery Packs for Electric Vehicle,” in *Proceedings - 2015 IEEE International Conference on Systems, Man, and Cybernetics, SMC 2015*, 2016, no. 1, pp. 783–788. doi: 10.1109/SMC.2015.146.

[78] B. Xia *et al.*, “A Comparative Study of Three Improved Algorithms Based on Particle Filter Algorithms in SOC Estimation of Lithium Ion Batteries,” *Energies*, vol. 10, no. 8, p. 1149, 2017, doi: 10.3390/en10081149.

[79] X. Shu, G. Li, J. Shen, W. Yan, Z. Chen, and Y. Liu, “An adaptive fusion estimation algorithm for state of charge of lithium-ion batteries considering wide operating temperature and degradation,” *J. Power Sources*, vol. 462, no. November 2019, p. 228132, 2020, doi: 10.1016/j.jpowsour.2020.228132.

[80] F. Zahng, G. Liu, L. Fang, and H. Wang, “Estimation of Battery State of Charge With H∞ Observer: Applied to a Robot for Inspecting Power Transmission Lines,” *IEEE Trans. Ind. Electron.*, vol. 59, no. 2, pp. 1086–1095, 2012.

[81] A. P. Schmidt, M. Bitzer, Á. W. Imre, and L. Guzzella, “Experiment-driven electrochemical modeling and systematic parameterization for a lithium-ion battery cell,” *J. Power Sources*, vol. 195, no. 15, pp. 5071–5080, 2010, doi: 10.1016/j.jpowsour.2010.02.029.

[82] S. Rahimian, S. Rayman, and R. White, “State of Charge and Loss of Active Material

Estimation of a Lithium Ion Cell under Low Earth Orbit Condition Using Kalman Filtering Approaches," *J. Electrochem. Soc.*, vol. 159, 2012.

[83] X. Han, M. Ouyang, L. Lu, and J. Li, "Simplification of physics-based electrochemical model for lithium ion battery on electric vehicle. Part II: Pseudo-two-dimensional model simplification and state of charge estimation," *J. Power Sources*, vol. 278, pp. 814–825, 2015, doi: 10.1016/j.jpowsour.2014.08.089.

[84] B. Y. Liaw, G. Nagasubramanian, R. G. Jungst, and D. H. Doughty, "Modeling of lithium ion cells - A simple equivalent-circuit model approach," *Solid State Ionics*, vol. 175, no. 1–4, pp. 835–839, 2004, doi: 10.1016/j.ssi.2004.09.049.

[85] J. Shen *et al.*, "Alternative combined co-estimation of state of charge and capacity for lithium-ion batteries in wide temperature scope," *Energy*, vol. 244, 2022, doi: 10.1016/j.energy.2022.123236.

[86] M. Verbrugge and E. Tate, "Adaptive state of charge algorithm for nickel metal hydride batteries including hysteresis phenomena," *J. Power Sources*, vol. 126, no. 1–2, pp. 236–249, 2004, doi: 10.1016/j.jpowsour.2003.08.042.

[87] R. Xiong, X. Gong, C. C. Mi, and F. Sun, "A robust state-of-charge estimator for multiple types of lithium-ion batteries using adaptive extended Kalman filter," *J. Power Sources*, vol. 243, pp. 805–816, 2013, doi: 10.1016/j.jpowsour.2013.06.076.

[88] Q. Zhu, M. Xu, W. Liu, and M. Zheng, "A state of charge estimation method for lithium-ion batteries based on fractional order adaptive extended kalman filter," *Energy*, vol. 187, p. 115880, 2019, doi: 10.1016/j.energy.2019.115880.

[89] B. Jiang, H. Dai, X. Wei, and T. Xu, "Joint estimation of lithium-ion battery state of charge and capacity within an adaptive variable multi-timescale framework considering current measurement offset," *Appl. Energy*, vol. 253, no. April, p. 113619, 2019, doi: 10.1016/j.apenergy.2019.113619.

[90] N. Chen, P. Zhang, J. Dai, and W. Gui, "Estimating the State-of-Charge of Lithium-Ion Battery Using an H-Infinity Observer Based on Electrochemical Impedance Model," *IEEE Access*, vol. 8, pp. 26872–26884, 2020.

[91] J. Xu, C. C. Mi, B. Cao, and J. Cao, “A new method to estimate the state of charge of lithium-ion batteries based on the battery impedance model,” *J. Power Sources*, vol. 233, pp. 277–284, 2013, doi: 10.1016/j.jpowsour.2013.01.094.

[92] W. Waag, S. Käbitz, and U. Sauer Dirk, “Experimental investigation of the lithium-ion battery impedance characteristic at various conditions and aging states and its influence on the application,” *Appl. Energy*, vol. 102, pp. 885–897, 2013.

[93] Y. Wu *et al.*, “State of Health Estimation for Lithium-Ion Batteries Based on Healthy Features and Long Short-Term Memory,” *IEEE Access*, vol. 8, pp. 28533–28547, 2020.

[94] M. A. Hannan *et al.*, “Toward Enhanced State of Charge Estimation of Lithium-ion Batteries Using Optimized Machine Learning Techniques,” *Sci. Rep.*, vol. 10, no. 1, pp. 1–15, 2020, doi: 10.1038/s41598-020-61464-7.

[95] T. Zahid, K. Xu, W. Li, C. Li, and H. Li, “State of charge estimation for electric vehicle power battery using advanced machine learning algorithm under diversi fi ed drive cycles,” *Energy*, vol. 162, pp. 871–882, 2018, doi: 10.1016/j.energy.2018.08.071.

[96] T. H. . Donato and M. Quiles, “Machine Learning Systems Based on xgBoost and MLP Neural Network Applied in Satellite Lithium-ion Battery Sets Impedance Estimation,” *Adv. Comput. Intell. An Int. J.*, vol. 5, pp. 1–20, 2018.

[97] F. Yang, W. Li, C. Li, and Q. Miao, “State-of-charge estimation of lithium-ion batteries based on gated recurrent neural network,” *Energy*, vol. 175, pp. 66–75, 2019, doi: 10.1016/j.energy.2019.03.059.

[98] B. Xia *et al.*, “State of charge estimation of lithium-ion batteries using optimized Levenberg-Marquardt wavelet neural network,” *Energy*, vol. 153, pp. 694–705, 2018, doi: 10.1016/j.energy.2018.04.085.

[99] Z. Deng, L. Yang, Y. Cai, H. Deng, and L. Sun, “Online available capacity prediction and state of charge estimation based on advanced data-driven algorithms for lithium iron phosphate battery,” *Energy*, vol. 112, pp. 469–480, 2016, doi: 10.1016/j.energy.2016.06.130.

[100] E. Chemali, P. J.Kollmeyer, M. Preindl, and A. Emadi, “State-of-charge estimation of Li-

ion batteries using deep neural networks: A machine learning approach," *J. Power Sources*, vol. 400, pp. 242–255, 2018.

[101] M. Messing, T. Shoa, R. Ahmed, and S. Habibi, "Battery SoC estimation from EIS using neural nets," *2020 IEEE Transp. Electrif. Conf. Expo, ITEC 2020*, pp. 588–593, 2020, doi: 10.1109/ITEC48692.2020.9161523.

[102] P. Kollmeyer, "Panasonic 18650PF Li-ion Battery Data," 2018.

[103] B. S. Brandt, *Linear and Polynomial Regression. In: Data Analysis*. New York: SPRINGER, 1999.

[104] M. K. Tran *et al.*, "Python-based scikit-learn machine learning models for thermal and electrical performance prediction of high-capacity lithium-ion battery," *Int. J. Energy Res.*, vol. 46, no. 2, pp. 786–794, 2022, doi: 10.1002/er.7202.

[105] S. Panchal, I. Dincer, M. Agelin-Chaab, R. Fraser, and M. Fowler, "Experimental and theoretical investigation of temperature distributions in a prismatic lithium-ion battery," *Int. J. Therm. Sci.*, vol. 99, pp. 204–212, 2016, doi: 10.1016/j.ijthermalsci.2015.08.016.

[106] K. Purohit *et al.*, "Soft sensors for state of charge, state of energy and power loss in formula student electric vehicle," *Appl. Syst. Innov.*, vol. 4, no. 4, p. 78, 2021, doi: 10.3390/asi4040078.

[107] Z. Wang, G. Feng, D. Zhen, F. Gu, and A. Ball, "A review on online state of charge and state of health estimation for lithium-ion batteries in electric vehicles," *Energy Reports*, vol. 7, pp. 5141–5161, 2021, doi: 10.1016/j.egyr.2021.08.113.

[108] Y. Tan and G. Zhao, "Transfer Learning With Long Short-Term Memory Network for State-of-Health Prediction of Lithium-Ion Batteries," *IEEE Trans. Ind. Electron.*, vol. 67, no. 10, pp. 8723–8731, 2020, doi: 10.1109/TIE.2019.2946551.

[109] D. Xiao *et al.*, "Reduced-Coupling Coestimation of SOC and SOH for Lithium-Ion Batteries Based on Convex Optimization," *IEEE Trans. Power Electron.*, vol. 35, no. 11, pp. 12332–12346, 2020, doi: 10.1109/TPEL.2020.2984248.

[110] M. Doyle, T. F. Fuller, and J. Newman, "Modeling of Galvanostatic Charge and Discharge

of the Lithium/Polymer/Insertion Cell," *J. Electrochem. Soc.*, vol. 140, no. 6, pp. 1526–1533, 1993, doi: 10.1149/1.2221597.

[111] S. L. Wang *et al.*, "Open circuit voltage and state of charge relationship functional optimization for the working state monitoring of the aerial lithium-ion battery pack," *J. Clean. Prod.*, vol. 198, pp. 1090–1104, 2018, doi: 10.1016/j.jclepro.2018.07.030.

[112] G. L. Plett, "Extended Kalman filtering for battery management systems of LiPB-based HEV battery packs - Part 3. State and parameter estimation," *J. Power Sources*, vol. 134, no. 2, pp. 277–292, 2004, doi: 10.1016/j.jpowsour.2004.02.033.

[113] B. Duan, Q. Zhang, F. Geng, and C. Zhang, "Remaining useful life prediction of lithium-ion battery based on extended Kalman particle filter," *Int. J. Energy Res.*, vol. 44, no. 3, pp. 1724–1734, 2020, doi: 10.1002/er.5002.

[114] C. Hu, B. D. Youn, and J. Chung, "A multiscale framework with extended Kalman filter for lithium-ion battery SOC and capacity estimation," *Appl. Energy*, vol. 92, pp. 694–704, 2012, doi: 10.1016/j.apenergy.2011.08.002.

[115] X. Tang, Y. Wang, C. Zou, K. Yao, Y. Xia, and F. Gao, "A novel framework for Lithium-ion battery modeling considering uncertainties of temperature and aging," *Energy Convers.*, vol. 180, pp. 162–170, 2019, doi: 10.1016/j.enconman.2018.10.082.

[116] C. Chen, R. Xiong, and W. Shen, "A Lithium-Ion Battery-in-the-Loop Approach to Test and Validate Multiscale Dual H Infinity Filters for State-of-Charge and Capacity Estimation," *IEEE Trans. Power Electron.*, vol. 33, no. 1, pp. 332–342, 2017, doi: 10.1109/TPEL.2017.2670081.

[117] X. Zhang, Q. Miao, and Z. Liu, "Remaining useful life prediction of lithium-ion battery using an improved UPF method based on MCMC," *Microelectron. Reliab.*, vol. 75, pp. 288–295, 2017, doi: 10.1016/j.microrel.2017.02.012.

[118] X. Hu, H. Yuan, C. Zou, Z. Li, and L. Zhang, "Co-Estimation of State of Charge and State of Health for Lithium-Ion Batteries Based on Fractional-Order Calculus," *IEEE Trans. Veh. Technol.*, vol. 67, no. 11, pp. 10319–10329, 2018, doi: 10.1109/TVT.2018.2865664.

[119] Z. Chen, C. C. Mi, Y. Fu, J. Xu, and X. Gong, "Online battery state of health estimation

based on Genetic Algorithm for electric and hybrid vehicle applications," *J. Power Sources*, vol. 240, pp. 184–192, 2013, doi: 10.1016/j.jpowsour.2013.03.158.

[120] H. Pan, Z. Lü, H. Wang, H. Wei, and L. Chen, "Novel battery state-of-health online estimation method using multiple health indicators and an extreme learning machine," *Energy*, vol. 160, pp. 466–477, 2018, doi: 10.1016/j.energy.2018.06.220.

[121] S. Li, S. Pischinger, C. He, L. Liang, and M. Stapelbroek, "A comparative study of model-based capacity estimation algorithms in dual estimation frameworks for lithium-ion batteries under an accelerated aging test," *Appl. Energy*, vol. 212, pp. 1522–1536, 2018, doi: 10.1016/j.apenergy.2018.01.008.

[122] X. Li, C. Yuan, X. Li, and Z. Wang, "State of health estimation for Li-Ion battery using incremental capacity analysis and Gaussian process regression," *Energy*, vol. 190, no. 116467, 2020, doi: 10.1016/j.energy.2019.116467.

[123] C. She, L. Zhang, Z. Wang, F. Sun, P. Liu, and C. Song, "Battery State of Health Estimation Based on Incremental Capacity Analysis Method: Synthesizing from Cell-Level Test to Real-World Application," *IEEE J. Emerg. Sel. Top. Power Electron.*, pp. 1–10, 2021, doi: 10.1109/JESTPE.2021.3112754.

[124] X. Feng *et al.*, "Online State-of-Health Estimation for Li-Ion Battery Using Partial Charging Segment Based on Support Vector Machine," *IEEE Trans. Veh. Technol.*, vol. 68, no. 9, pp. 8583–8592, 2019, doi: 10.1109/TVT.2019.2927120.

[125] P. Guo, Z. Cheng, and L. Yang, "A data-driven remaining capacity estimation approach for lithium-ion batteries based on charging health feature extraction," *J. Power Sources*, vol. 412, pp. 442–450, 2019, doi: 10.1016/j.jpowsour.2018.11.072.

[126] C. Hu, G. Jain, C. Schmidt, C. Strief, and M. Sullivan, "Online estimation of lithium-ion battery capacity using sparse Bayesian learning," *J. Power Sources*, vol. 289, pp. 105–113, 2015, doi: 10.1016/j.jpowsour.2015.04.166.

[127] C. Hu, G. Jain, P. Zhang, C. Schmidt, P. Gomadam, and T. Gorka, "Data-driven method based on particle swarm optimization and k-nearest neighbor regression for estimating capacity of lithium-ion battery," *Appl. Energy*, vol. 129, pp. 49–55, 2014, doi:

10.1016/j.apenergy.2014.04.077.

[128] G. Bai, P. Wang, C. Hu, and M. Pecht, “A generic model-free approach for lithium-ion battery health management,” *Appl. Energy*, vol. 135, pp. 247–260, 2014, doi: 10.1016/j.apenergy.2014.08.059.

[129] D. I. Stroe and E. Schaltz, “Lithium-Ion Battery State-of-Health Estimation Using the Incremental Capacity Analysis Technique,” *IEEE Trans. Ind. Appl.*, vol. 56, no. 1, pp. 678–685, 2020, doi: 10.1109/TIA.2019.2955396.

[130] G. You, S. Park, and D. Oh, “Diagnosis of Electric Vehicle Batteries Using Recurrent Neural Networks,” *IEEE Trans. Ind. Electron.*, vol. 64, no. 6, pp. 4885–4893, 2017, doi: 10.1109/TIE.2017.2674593.

[131] S. Shen, M. Sadoughi, X. Chen, M. Hong, and C. Hu, “A deep learning method for online capacity estimation of lithium-ion batteries,” *J. Energy Storage*, vol. 25, no. 100817, 2019, doi: 10.1016/j.est.2019.100817.

[132] K. Kaur, A. Garg, X. Cui, S. Singh, and B. K. Panigrahi, “Deep learning networks for capacity estimation for monitoring SOH of Li-ion batteries for electric vehicles,” *Int. J. Energy Res.*, vol. 45, no. 2, pp. 3113–3128, 2020, doi: 10.1002/er.6005.

[133] Y. Li, H. Sheng, Y. Cheng, D. Stroe, and R. Teodorescu, “State-of-health estimation of lithium-ion batteries based on semi-supervised transfer component analysis,” *Appl. Energy*, vol. 277, no. 115504, 2020, doi: 10.1016/j.apenergy.2020.115504.

[134] S. Shen, M. Sadoughi, M. Li, Z. Wang, and C. Hu, “Deep convolutional neural networks with ensemble learning and transfer learning for capacity estimation of lithium-ion batteries,” *Appl. Energy*, vol. 260, no. 114296, 2020, doi: 10.1016/j.apenergy.2019.114296.

[135] Y. Li, K. Li, X. Liu, Y. Wang, and L. Zhang, “Lithium-ion battery capacity estimation — A pruned convolutional neural network approach assisted with transfer learning,” *Appl. Energy*, vol. 285, no. 116410, 2021, doi: 10.1016/j.apenergy.2020.116410.

[136] X. Shu, J. Shen, G. Li, Y. Zhang, Z. Chen, and Y. Liu, “A Flexible State-of-Health Prediction Scheme for Lithium-Ion Battery Packs with Long Short-Term Memory Network and Transfer Learning,” *IEEE Trans. Transp. Electrif.*, vol. 7, no. 4, pp. 2238–2248, 2021,

doi: 10.1109/TTE.2021.3074638.

[137] C. Pastor-Fernández, K. Uddin, G. H. Chouchelamane, W. D. Widanage, and J. Marco, "A Comparison between Electrochemical Impedance Spectroscopy and Incremental Capacity-Differential Voltage as Li-ion Diagnostic Techniques to Identify and Quantify the Effects of Degradation Modes within Battery Management Systems," *J. Power Sources*, vol. 360, pp. 301–318, 2017, doi: 10.1016/j.jpowsour.2017.03.042.

[138] W. Majchrzycki, E. Jankowska, M. Baraniak, P. Handzlik, and R. Samborski, "Electrochemical Impedance Spectroscopy and Determination of the Internal Resistance as a Way to Estimate Lead-Acid Batteries Condition," *Batteries*, vol. 4, no. 4, p. 70, 2018, doi: 10.3390/batteries4040070.

[139] A. Guha and A. Patra, "State of Health Estimation of Lithium-Ion Batteries Using Capacity Fade and and Internal Resistance Growth Models," *IEEE Trans. Transp. Electrif.*, vol. 4, no. 1, pp. 135–146, 2018, doi: 10.1109/TTE.2017.2776558.

[140] J. Qiao, X. Liu, and Z. Chen, "Prediction of the Remaining Useful Life of Lithium-Ion Batteries Based on Empirical Mode Decomposition and Deep Neural Networks," *IEEE Access*, vol. 8, pp. 42760–42767, 2020, doi: 10.1109/ACCESS.2020.2977429.

[141] P. M. Attia *et al.*, "Closed-loop optimization of fast-charging protocols for batteries with machine learning," *Nature*, vol. 578, no. 7795, pp. 397–402, 2020, doi: 10.1038/s41586-020-1994-5.

[142] Y. Zou, X. Hu, H. Ma, and S. E. Li, "Combined State of Charge and State of Health estimation over lithium-ion battery cell cycle lifespan for electric vehicles," *J. Power Sources*, vol. 273, pp. 793–803, 2015, doi: 10.1016/j.jpowsour.2014.09.146.

[143] R. Xiong, J. Wang, W. Shen, J. Tian, and H. Mu, "Co-Estimation of State of Charge and Capacity for Lithium-Ion Batteries with Multi-Stage Model Fusion Method," *Engineering*, vol. 7, no. 10, pp. 1469–1482, 2021, doi: 10.1016/j.eng.2020.10.022.

[144] Y. Gao, K. Liu, C. Zhu, X. Zhang, and D. Zhang, "Co-Estimation of State-of-Charge and State-of- Health for Lithium-Ion Batteries Using an Enhanced Electrochemical Model," *IEEE Trans. Ind. Electron.*, vol. 69, no. 3, pp. 2684–2696, 2022, doi:

10.1109/TIE.2021.3066946.

[145] T. Ouyang, P. Xu, J. Lu, X. Hu, B. Liu, and N. Chen, “Co-estimation of State-of-Charge and State-of-Health for Power Batteries Based on Multi-thread Dynamic Optimization Method,” *IEEE Trans. Ind. Electron.*, vol. 69, no. 2, pp. 1157–1166, 2021, doi: 10.1109/TIE.2021.3062266.

[146] K. Mc Carthy, H. Gullapalli, K. M. Ryan, and T. Kennedy, “Electrochemical impedance correlation analysis for the estimation of Li-ion battery state of charge, state of health and internal temperature,” *J. Energy Storage*, vol. 50, p. 104608, 2022, doi: 10.1016/j.est.2022.104608.

[147] A. Mondal, A. Routray, and S. Puravankara, “Parameter identification and co-estimation of state-of-charge of Li-ion battery in real-time on Internet-of-Things platform,” *J. Energy Storage*, vol. 51, p. 104370, 2022, doi: 10.1016/j.est.2022.104370.

[148] X. Lai *et al.*, “Co-estimation of state of charge and state of power for lithium-ion batteries based on fractional variable-order model,” *J. Clean. Prod.*, vol. 255, p. 120203, 2020, doi: 10.1016/j.jclepro.2020.120203.

[149] Z. Xu, J. Wang, P. D. Lund, and Y. Zhang, “Co-estimating the state of charge and health of lithium batteries through combining a minimalist electrochemical model and an equivalent circuit model,” *Energy*, vol. 240, p. 122815, 2022, doi: 10.1016/j.energy.2021.122815.

[150] X. Li, Z. Wang, and L. Zhang, “Co-estimation of capacity and state-of-charge for lithium-ion batteries in electric vehicles,” *Energy*, vol. 174, pp. 33–44, 2019, doi: 10.1016/j.energy.2019.02.147.

[151] Y. Song, D. Liu, H. Liao, and Y. Peng, “A hybrid statistical data-driven method for on-line joint state estimation of lithium-ion batteries,” *Appl. Energy*, vol. 261, p. 114408, 2020, doi: 10.1016/j.apenergy.2019.114408.

[152] K. Liu, Y. Shang, Q. Ouyang, and W. D. Widanage, “A Data-Driven Approach with Uncertainty Quantification for Predicting Future Capacities and Remaining Useful Life of Lithium-ion Battery,” *IEEE Trans. Ind. Electron.*, vol. 68, no. 4, pp. 3170–3180, 2021, doi: 10.1109/TIE.2020.2973876.

[153] V. Klass, M. Behm, and G. Lindbergh, “Capturing lithium-ion battery dynamics with support vector machine-based battery model,” *J. Power Sources*, vol. 298, pp. 92–101, 2015, doi: 10.1016/j.jpowsour.2015.08.036.

[154] J. H. Lee and I. S. Lee, “Lithium battery SOH monitoring and an SOC estimation algorithm based on the SOH result,” *Energies*, vol. 14, no. 15, 2021, doi: 10.3390/en14154506.

[155] Y. Che, Y. Liu, Z. Cheng, and J. Zhang, “SOC and SOH Identification Method of Li-Ion Battery Based on SWPSO-DRNN,” *IEEE J. Emerg. Sel. Top. Power Electron.*, vol. 9, no. 4, pp. 4050–4061, 2021, doi: 10.1109/JESTPE.2020.3004972.

[156] Q. Wang, M. Ye, M. Wei, G. Lian, and C. Wu, “Co-estimation of state of charge and capacity for lithium-ion battery based on recurrent neural network and support vector machine,” *Energy Reports*, vol. 7, pp. 7323–7332, 2021, doi: 10.1016/j.egyr.2021.10.095.

[157] Z. Du, L. Zuo, J. Li, Y. Liu, and H. T. Shen, “Data-Driven Estimation of Remaining Useful Lifetime and State of Charge for Lithium-Ion Battery,” *IEEE Trans. Transp. Electrif.*, vol. 8, no. 1, pp. 356–367, 2022, doi: 10.1109/TTE.2021.3109636.

[158] Q. Zhang, C. G. Huang, H. Li, G. Feng, and W. Peng, “Electrochemical Impedance Spectroscopy based State of Health Estimation for Lithium-ion Battery Considering Temperature and State of Charge Effect,” *IEEE Trans. Transp. Electrif.*, 2022, doi: 10.1109/TTE.2022.3160021.

[159] I. Babaeiyazdi, A. Rezaei-Zare, and S. Shokrzadeh, “Transfer Learning with Deep Neural Network for Capacity Prediction of Li-ion Batteries Using EIS Measurement,” *IEEE Trans. Transp. Electrif.*, pp. 1–10, 2022, doi: 10.1109/TTE.2022.3170230.

[160] G. Pozzato, A. Allam, and S. Onori, “Lithium-ion battery aging dataset based on electric vehicle real-driving profiles,” *Data Br.*, vol. 41, p. 107995, 2022, doi: 10.1016/j.dib.2022.107995.

[161] X. Feng, J. Chen, Z. Zhang, S. Miao, and Q. Zhu, “State-of-charge estimation of lithium-ion battery based on clockwork recurrent neural network,” *Energy*, vol. 236, p. 121360, 2021, doi: 10.1016/j.energy.2021.121360.

[162] S. Behera, R. Misra, and A. Sillitti, “Multiscale deep bidirectional gated recurrent neural

networks based prognostic method for complex non-linear degradation systems," *Inf. Sci. (Ny).*, vol. 554, pp. 120–144, 2021, doi: 10.1016/j.ins.2020.12.032.

[163] S. Li *et al.*, "State-of-charge estimation of lithium-ion batteries in the battery degradation process based on recurrent neural network," *Energies*, vol. 14, no. 2, pp. 1–21, 2021, doi: 10.3390/en14020306.

[164] A. Sherstinsky, "Fundamentals of Recurrent Neural Network (RNN) and Long Short-Term Memory (LSTM) network," *Phys. D Nonlinear Phenom.*, vol. 404, p. 132306, 2020, doi: 10.1016/j.physd.2019.132306.

[165] S. Jin, X. Sui, X. Huang, S. Wang, R. Teodorescu, and D. I. Stroe, "Overview of machine learning methods for lithium-ion battery remaining useful lifetime prediction," *Electron.*, vol. 10, no. 24, pp. 1–18, 2021, doi: 10.3390/electronics10243126.

[166] Y. Zhang, R. Xiong, H. He, and M. G. Pecht, "Long short-term memory recurrent neural network for remaining useful life prediction of lithium-ion batteries," *IEEE Trans. Veh. Technol.*, vol. 67, no. 7, pp. 5695–5705, 2018, doi: 10.1109/TVT.2018.2805189.

[167] K. Park, Y. Choi, W. J. Choi, H. Y. Ryu, and H. Kim, "LSTM-Based Battery Remaining Useful Life Prediction with Multi-Channel Charging Profiles," *IEEE Access*, vol. 8, pp. 20786–20798, 2020, doi: 10.1109/ACCESS.2020.2968939.

[168] J. Hong, Z. Wang, W. Chen, L. Y. Wang, and C. Qu, "Online joint-prediction of multi-forward-step battery SOC using LSTM neural networks and multiple linear regression for real-world electric vehicles," *J. Energy Storage*, vol. 30, no. January, p. 101459, 2020, doi: 10.1016/j.est.2020.101459.

[169] X. Ren, S. Liu, X. Yu, and X. Dong, "A method for state-of-charge estimation of lithium-ion batteries based on PSO-LSTM," *Energy*, vol. 234, p. 121236, 2021, doi: 10.1016/j.energy.2021.121236.

[170] F. Yang, S. Zhang, W. Li, and Q. Miao, "State-of-charge estimation of lithium-ion batteries using LSTM and UKF," *Energy*, vol. 201, p. 117664, 2020, doi: 10.1016/j.energy.2020.117664.